AEC-DEPARTMENT OF COMMERCE-DEPARTMENT OF DEFENSE-NASA-NSF
DEPARTMENT OF INTERIOR-DEPARTMENT OF TRANSPORTATION

BOMEX BULLETIN NO. 10

June 1971

CONTENTS

From the Editorial Desk

Mr. DeVer Colson, Editor of the BOMEX Bulletin, retired from government service on May 31, 1971. All inquiries, and material for publication in future issues, should be directed to Mrs. May Laughrun, Editor, BOMAP Office, Rx9, NOAA, Rockville, Md. 20852.

I.   BOMEX PARTICIPANTS INFORMATION EXCHANGE

In response to inquiries by the BOMAP Office, the information contained in this section has been furnished by BOMEX participants. We believe that such information - including notes on results, novel techniques, problems, plans, critiques - will be of interest not only to those directly concerned with BOMEX data but also to the scientific community at large, and we will welcome additional material for publication in future issues. Past summaries of information received from BOMEX participants have been published in BOMEX Bulletin Nos. 6, 8, and 9.

EXPERIMENT 4:   Water Vapor Flux Transport

PRINCIPAL INVESTIGATOR: Dr. Bradford R. Bean

AFFILIATION: Environmental Research Laboratories, NOAA

Preliminary results of initial analysis of the RFF Gust Probe Experiment are currently being submitted for publication. However, the following more or less summarizes our findings to date:

(1)   The average evaporation for the several days which we flew was ~ 0.5 cm/day.

(2)   The evaporative flux measurements indicate large variability in time (diurnal and interdiurnal) and space.

(3)   The ρ_w' spectra of longer runs indicate a compromise of these data by the phugoidal motion of the aircraft. Luckily, the spectra of $\rho_w'w'$ indicate this compromise only slightly affects the values of flux. We are presently instituting schemes to eliminate phugoidal motion from the ρ_w' data. This effect will be present in all parameters measured by other aircraft unless specifically removed or accounted for in data reduction.

(4)   The spectra of flux averaged for several 5-min runs as well as several 10-min runs indicate significant differences in scale size when flying along the wind as opposed to flying across the wind.

(5)   The flux spectra also show a good relationship between the scale size and altitude of measurement.

(6)   Time series signatures allow us to speculate on a model of the **convective** element which is known as a puff under shear.

We are concentrating our efforts on a detailed description of the convective element as well as its interaction with larger scale size phenomena (such as roll vortexes, waves, etc.) which our data indicate may be present.

EXPERIMENT 10: Radon-222 and African Dust in the North Atlantic Trade Winds

PRINCIPAL INVESTIGATORS: Dr. Joseph M. Prospero[1] and Dr. Toby N. Carlson[2]

AFFILIATION: [1]School of Atmospheric Science, University of Miami, and [2]National Hurricane Research Laboratory, NOAA, Miami, Fla.

The following is a preliminary and condensed version of a paper by Drs. Prospero and Carlson entitled "The Structure and Dynamics of the African Dust Layer Over the Equatorial Atlantic Ocean During BOMEX." The article will be submitted for publication at a later date.

Introduction

Aerosol studies performed at Barbados, West Indies, almost continuously from 1965 to 1969 have shown that large amounts of dust are being transported by air currents from the arid and semiarid stretches of North Africa to the Caribbean during the summer and early fall (Prospero, 1968). Similar studies made at Miami (Prospero and Carlson, 1971) and Bermuda (Bricker and Prospero, 1969) indicate that large quantities of this dust are regularly carried into the higher latitudes. Recent work by Prospero and Carlson (1970) and by Prospero et al. (1970) documents the movement of a number of specific dust outbreaks from Africa; these studies show that, although the measured quantities of airborne dust arriving at Barbados are highly variable from day to day, the dust stream has a coherent structure that is determined by the mixing processes and the peculiarities of air flow over Africa.

During BOMEX, we performed a number of experiments in addition to the regular aerosol program which we have carried out on the island for the past several years. Our principal effort was the measurement of the atmospheric concentration of radon-222, a radioactive inert gas (half-life of 3.82 days) produced in the uranium-238 decay series. Atmospheric radon has its source at the ground as is the case with sensible heat and water vapor. In contrast, the emanation rate of radon from the ocean is about a factor of 100 less; consequently, radon is a good tracer for air parcels that have recently been in convective contact with a continental land mass. The radon-222 activity in the atmosphere was measured from two DC-6 aircraft of the National Oceanic and Atmospheric Administration's Research Flight Facility (RFF) (Friedman et al., 1970); approximately 30 flights were made during the three months of BOMEX. A description of the method used in determining the concentration of radon-222 - more specifically, the concentration of radon daughter products - on board these aircraft has been set forth by Prospero and Carlson (1970).

The particular usefulness of radon-222 and dust as tracers of air motions in the tropics can be understood by considering the early history of air streams passing over Africa. As dry, cool air progresses over the arid regions of North Africa, it is subjected to intense heating from below, as a consequence of the large amount of incoming radiation and of the disproportionately large fraction of this energy that is redistributed to the atmosphere in the form of sensible, rather than latent, heat (Carlson and Ludlam, 1968). Within a few days, the air stream becomes completely modified by the dry convection in the mixing layer, and it acquires a unique set of characteristics identifying it as "Saharan" air. Saharan air is recognizable on meteorological soundings made over the interior of the Sahara as a deep, well-mixed layer of nearly uniform potential temperature and mixing ratio. In July this layer attains its greatest warmth (a potential temperature, θ, of about 43°C) and depth (about 15,000 ft) (Carlson and Ludlam, 1968). The top of this mixing layer is capped by an inversion created by the overshooting of dry thermals through the top of the mixing layer. Because of the prolonged mixing, the relative humidity increases with height, attaining a maximum a little below the top of the mixing layer and decreasing sharply above. Despite the incorporation of air with higher potential temperature - and much lower water vapor content - from above, the overshooting of dry thermals causes the air at the top to be slightly colder than the surrounding unmodified air; in contrast, the base of the heated layer possesses the greatest anomalous warmth. Depending on the extent of mixing and the moisture available, the mixing layer may become nearly saturated over a thin layer near the top.

The amount of dust raised is dependent on soil type and the strength of the wind and low levels (Warn, 1952; Burns, 1961), conditions that vary considerably across the Sahara. One would expect, therefore, that the quantity of dust raised within an air stream about to depart the Sahara would vary markedly from day to day according to the path of the air stream and the meteorological conditions to which it has been subjected.

There is much evidence that the unusually large dust loadings measured at Barbados during the summer and early fall are occasionally attributable to dramatic upserges in dust storm activity over the Sahara (e.g., Prospero et al., 1970). Statistics compiled by us show that dust storm activity over the western Sahara appears to increase in response to passing disturbances to the south. This result has been recently verified by close examination of ATS-3 satellite pictures, which show a discontinuous pattern of stratocumulus and dust moving westward off the African coast between 15° and 25°N behind the axis of each successive disturbance. The reason for this is not entirely clear, but we suggest that alternate weakening and strengthening of the pressure gradient occurs with the passage of disturbances.

Our observations show that the radon and dust are sharply confined below the inversion at the top of the African mixing layer (Prospero and Carlson, 1970). In figure 1, Saharan air is recognizable on the Cape Verde sounding as a deep layer of air with an almost constant lapse rate (potential temperature about 42°C) between 820 and 600 mb. In the bottom 100 mb, the flow is approximately parallel to the coastline of Africa except for a marked inland component south of about 20°N. The steadiness of this flow precludes the possibility that Saharan air reaches Cape Verde except above 100 mb. Indeed, it would appear that the Saharan air begins to slide over the northeasterly
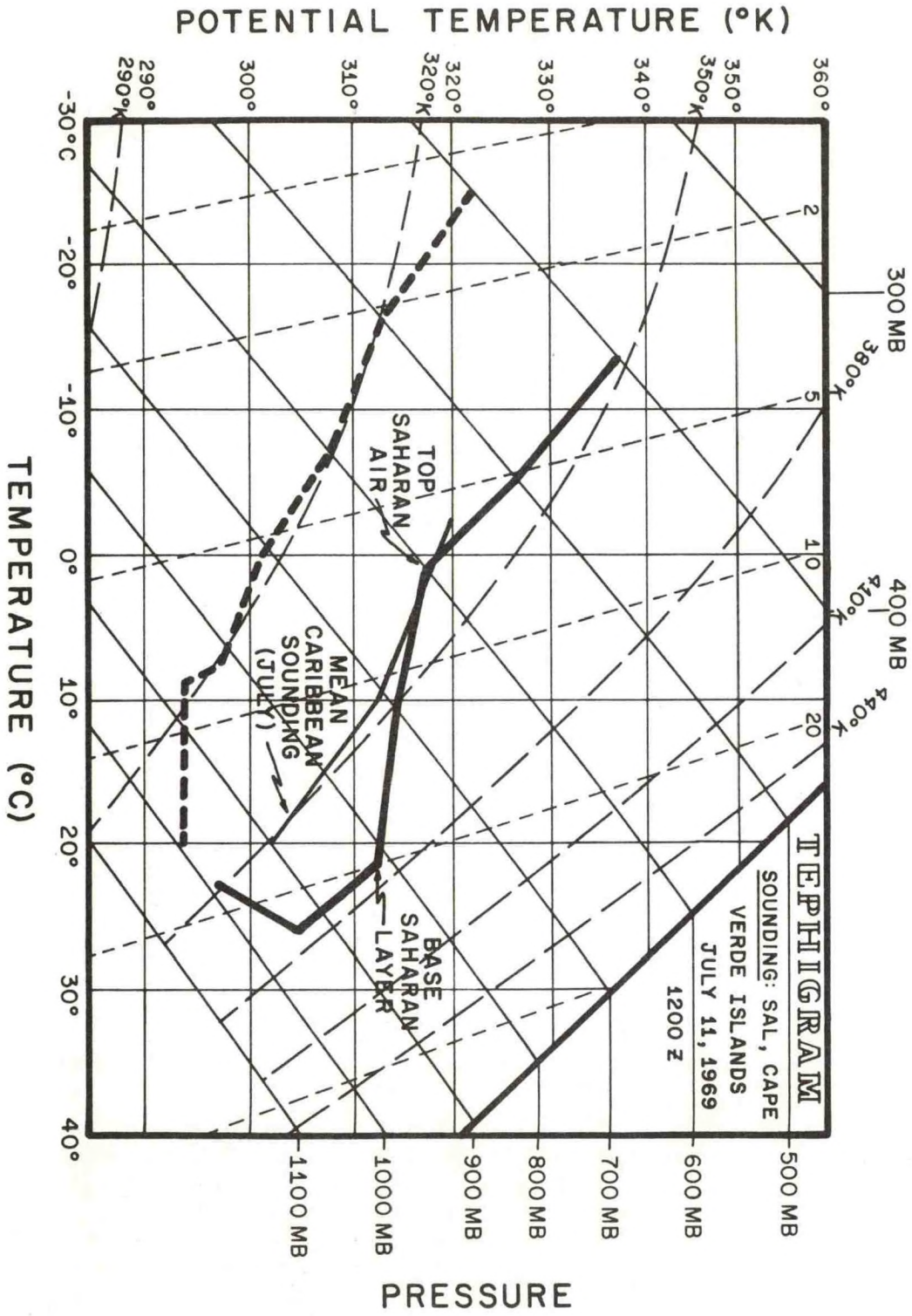
Figure 1. Tephigram representation of a sounding at Sal, Cape Verde Islands, July 11, 1969, as compared with a typical Caribbean sounding. Solid lines indicate temperature soundings; heavy dashed lines show mean point (mixing ratio).

4

pre-trade-wind flow even before reaching the coastline. At Cape Verde, the
air lying between the base of the inversion and the surface represents a
transition between maritime air that has not passed over the Sahara and air
that has resided for some time over arid terrain. The normal radiation and
convective processes associated with the trade wind moist layer bring about a
gradual deepening and moistening of the lower layer as the air flows westward
in the tropics. Until the cumulus convection can penetrate the Saharan air,
the top of the trade wind moist layer, i.e., the trade wind inversion, remains
situated at the base of the Saharan air, and deeper convection associated with
cumulus congestus is stronly suppressed by the stable lid above it. The
trade wind moist layer (initially low in radon because of its relatively long
residence time over the North Atlantic) is continually enriched in radon and
dust by a small amount of penetrative pixing at the base of the Saharan air;
it is further enriched in dust fallout from the upper layer.

BOMEX Results

A good case study of a dust outbreak is provided by the disturbance that
passed the Cape Verde Islands just before July 11, 1969; the disturbance is
clearly visible at 35°W on the satellite photograph in figure 2 as an inverted
'V' in the ITC cloud pattern. (See Frank, 1969, for a description of the in-
verted 'V'.) To the rear (east) of the wave axis one can see curved bands of
stratocumulus set against a background of gossamer whiteness, which our obser-
vations repeatedly have shown to be representative of dust or haze. Examina-
tion of a sequential series of satellite photographs reveals the continued
westward motion of both the wave axis and the curved bands of stratocumulus.
Close inspection of several similar situations during the summer of 1969 sug-
gests that the disturbance acts as a barrier to the flow at middle levels,
causing the dust stream to curl anticyclonically behind the disturbance.
Along the African coast, the blocking of the flow by a disturbance tends to
induce northward flow of dust into midlatitudes (Carlson, 1969 a and b).

On July 14, 1969, two RFF DC-6 aircraft penetrated this same disturbance,
then located near 56°W. Although the wave had weakened considerably and the
dust was not clearly visible on the satellite photograph, the aircraft obser-
vations showed a moderate increase in haziness and radon activity as the
aircraft flew westward across the wave axis at low levels. As the aircraft
ascended to 10,000 ft behind the disturbance, the radon activity increased
tenfold, reaching a maximum in the region of densest haze; in this region,
the air filters used for the radon measurements attained a deep red-brown
color similar to that of dust collected at Barbados. In contrast, no haze
was observed west of the disturbance.

A comparison of a sounding from the *Discoverer* made in the dusty air
behind the wave with the profile made behind the same disturbance at Cape
Verde shows the similarity in the structure of the African layer (fig. 3).
In the absence of convective mixing over the ocean, the cooling that occurred
in the 4- to 5-days' travel from 22°W to 54°W represents a net radiational
deficit (long wave loss less short wave gain) of about 0.5°C per day. One
can further conclude from such reasoning that the rate of vertical motion in
the upper part of the Saharan duct was negligible since the upper inversion,
a substantial surface, changed altitude by only 20 mb during that period.

5
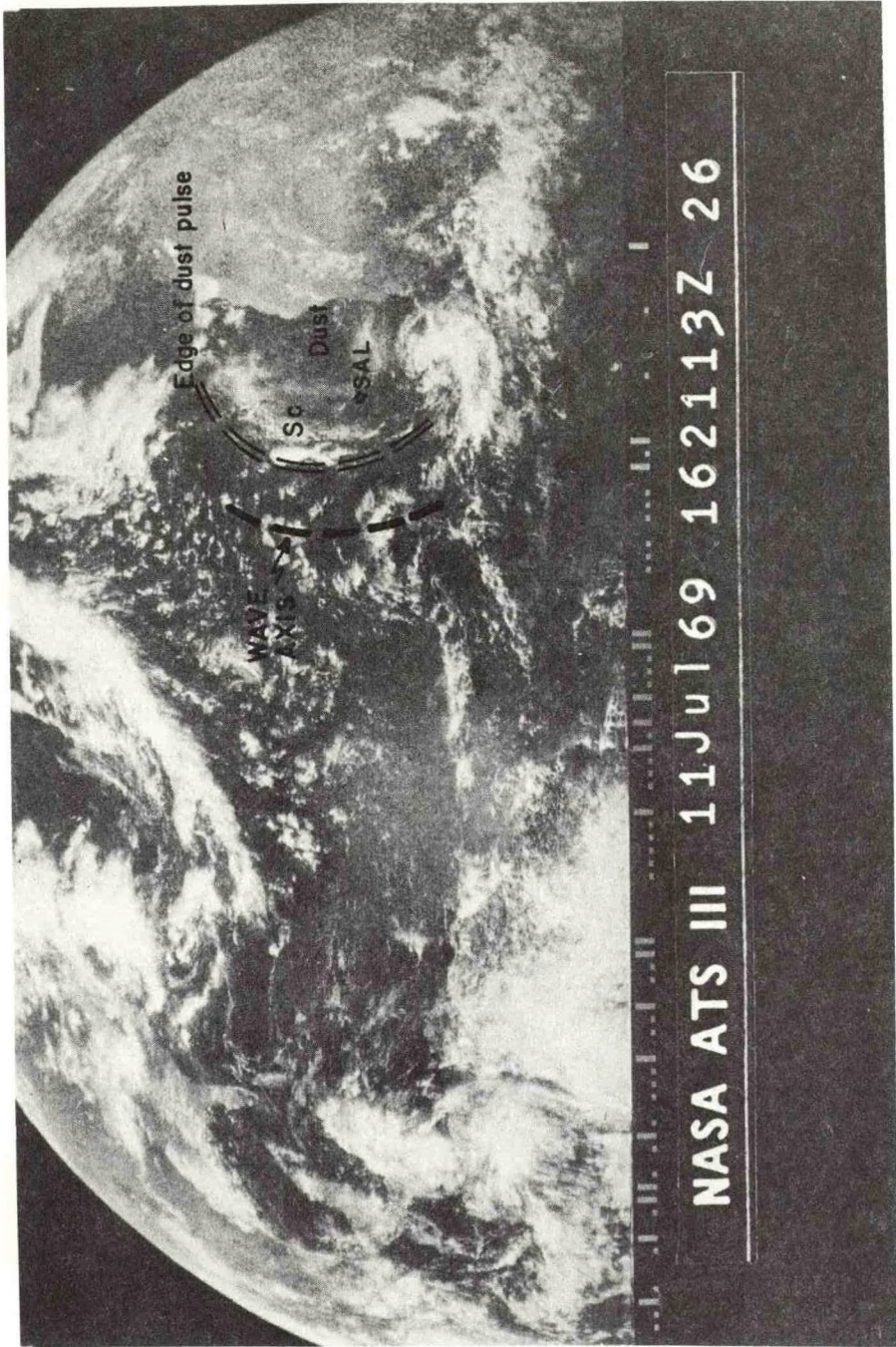
Figure 2. ATS-3 satellite photograph showing the axis of the tropical disturbance that emerged off the African coast on July 9, 1969, and the leading edge of the dust and stratocumulus pulse that followed it.

6

Figure 3. Sounding made at the Discoverer, July 15, 1969, at 1200 GMT. The heavy solid and dashed lines show temperature and dew point (mixing ratio), respectively, and the thin solid line is part of the Sal temperature sounding shown in fig. 1. The wind vectors are shown at the right.

Deep isentropic layers formed by intense heating over land are characterized by relatively high temperatures in their lower portion. In figure 1, the base of the S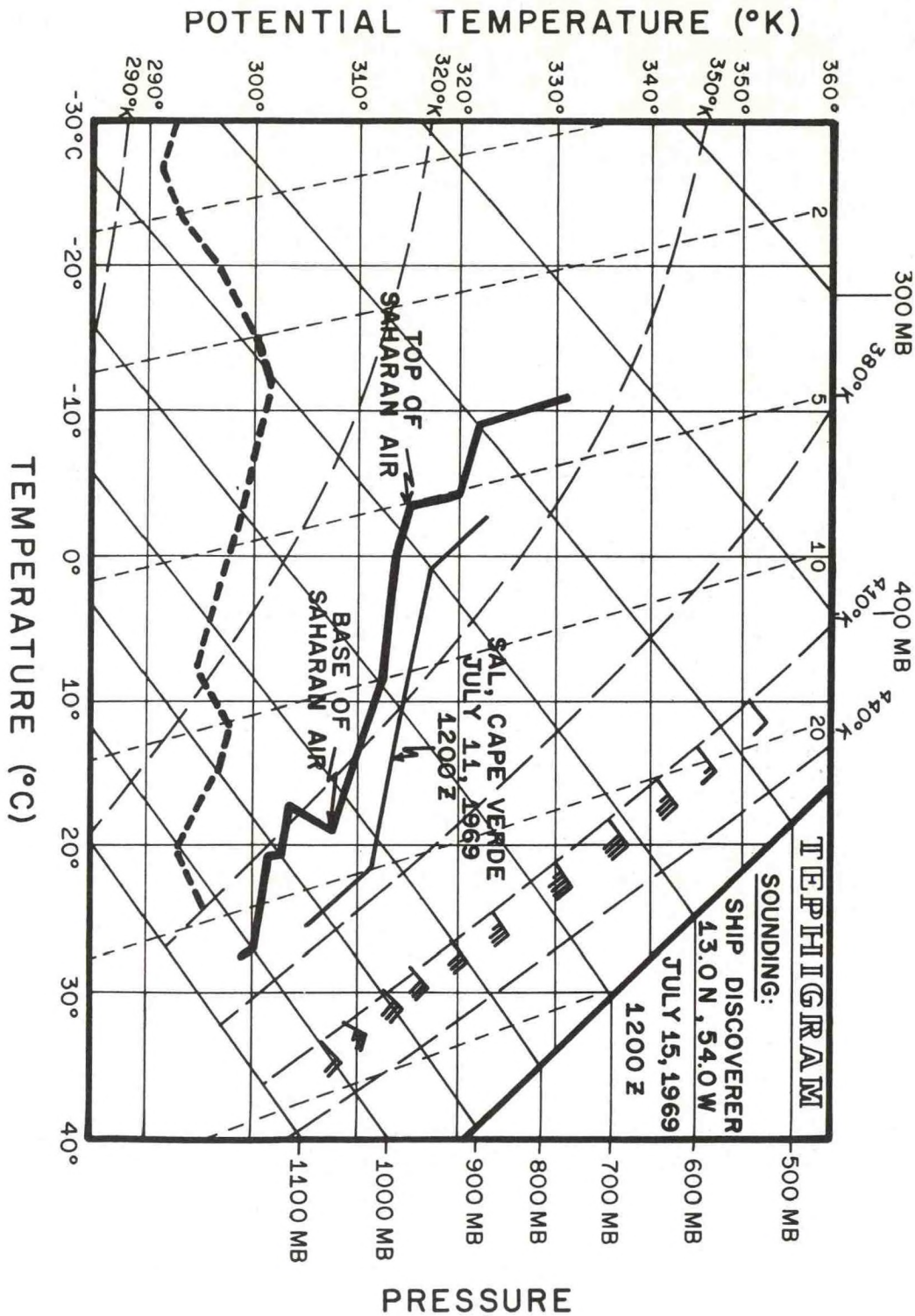aharan air at 820 mb was about 7°C warmer than the mean Caribbean sounding at that level. Despite radiational cooling of the Saharan layer, the dusty air continues to be appreciably warmer than its surroundings near 800 mb according to the *Discoverer* sounding (fig. 3); it should be noted, however, that the upper portion of the Saharan air is slightly cooler than the ambient air.

The pair of soundings in figure 4 illustrate the sharp temperature differences that can occur across the front of a dust pulse. On July 18, 1969, the RFF DC-6 39C aircraft ascended to 520 mb in the vicinity of Barbados and proceeded eastward at that level; during this time the radon concentration remained low and the filters clean. Concurrently, the RFF DC-6 40C ascended to 760 mb east of Barbados at point A-A' (temperature and humidity coordinates, respectively) as shown in figure 4 and continued to fly eastward without encountering much change in temperature or humidity; atmospheric conditions were suppressed but no haze was visible. At about longitude 56°W, the DC-6 40C aircraft encountered a very rapid warming and drying of the air as it penetrated the dusty airstream; within a very few minutes the temperature and humidity had changed to values B and B', respectively, on the sounding, and the air became very hazy with an accompanying large increase in radon concentration. At the same time the 39C, flying above the 40C at 520 mb, reported seeing a dense haze layer below although the radon activity at the upper level remained low. A short time later, the 40C aircraft ascended to 670 mb at point C-C' on the sounding; after continuing at this level for some time, it descended to D-D' and then to E-E'.

Although the haze top undoubtedly was above 670 mb, the highest level reached by the 40C, the Saharan air is still easily recognizable on the 40C aircraft sounding in figure 4 as an exceedingly well-mixed layer whose potential temperature and mixing ratios were uniformly about 40°C and 3.6 g/kg, respectively. Radon activity was also uniformly high between C-C' and D-D' although the highest counts were actually experienced near 700 mb. At point D-D' on the sounding, the temperature of the dust plume was about 5° warmer than the air at that same level a little farther to the west at the point of ascent of the 39C. In crossing the "dust front," the winds recorded on the RFF 40C aircraft changed direction slightly and increased markedly. We have noted wind speed increases on other occasions when making the transition from clear to hazy air; we attribute these increases to the presence of a jet in the upper part of the Saharan layer. An example of this is found in the sounding in figure 3 which shows a 45-kt wind speed maximum at 670 mb. The occurrence of sudden wind increases with the passage of disturbances in the tropics have long been observed and have been referred to as "surges in the trades;" thus, the jet is probably a regular feature of these disturbances.

Conclusion

These few examples illustrate the value of tracers such as radon-222 and dust when used in conjunction with the more conventional conservative properties of potential temperature and water vapor. By this multiple tracer technique, we expect to obtain a much better understanding of the factors effecting the transport of African air parcels and dust across the Atlantic.

POTENTIAL TEMPERATURE (°K)

TEMPERATURE (°C)

PRESSURE

TEPHIGRAM

AIRCRAFT SOUNDING:
JULY 18, 1969

BASE SAHARAN LAYER
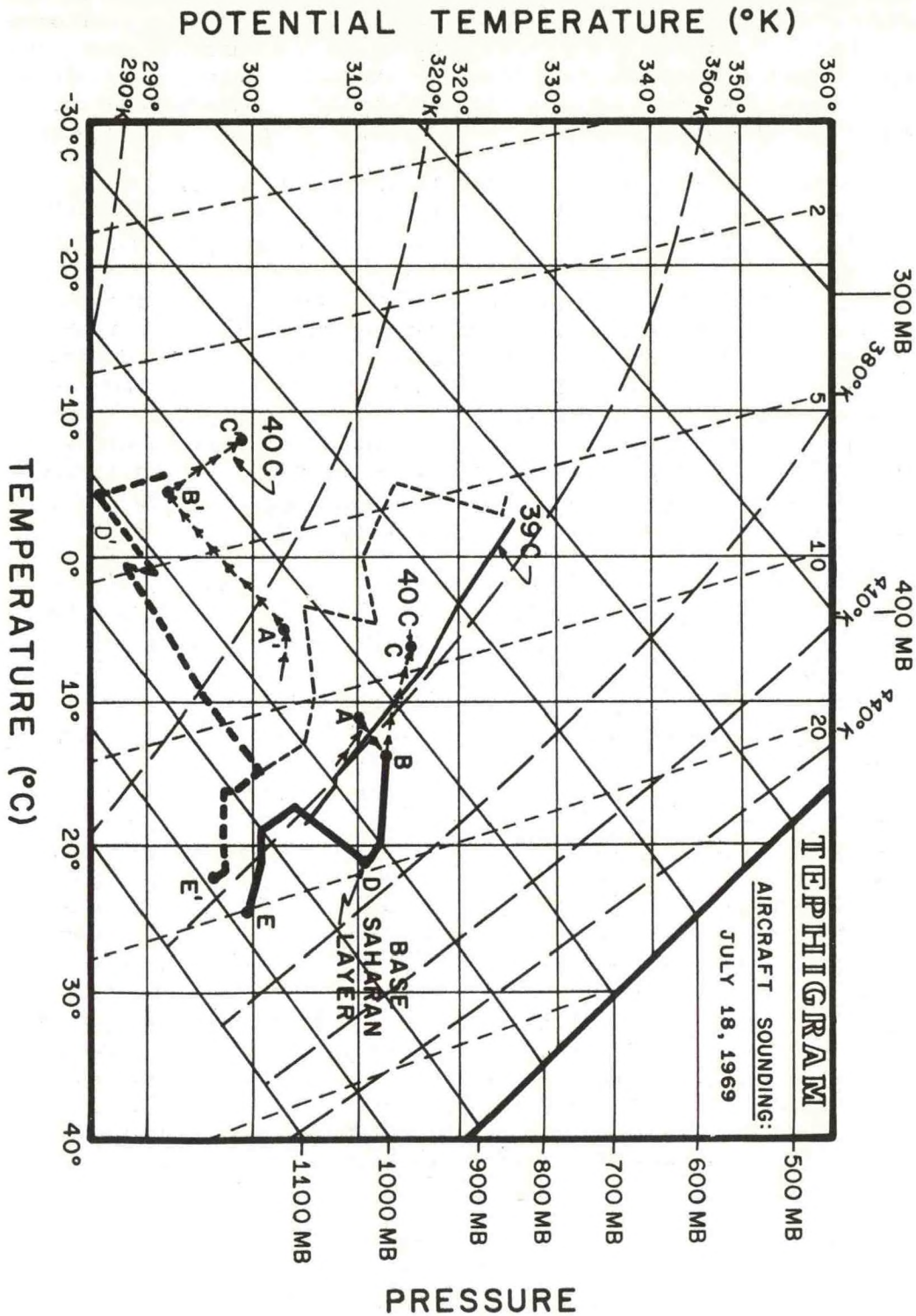
Figure 4. Aircraft soundings by DC-6 39C and 40C aircraft east of Barbados, July 18, 1969, point at approximately 1200 GMT. Arrows indicate continuous aircraft temperature and dashed lines dew point. Solid lines are temperature and dashed lines dew point. Arrows indicate continuous aircraft soundings from C-C' to E-E'. Sounding C-C', to point during descent, the 40C aircraft descended during A-A', but the 40C of E-E' was traced during descent from C-C' to E-E'; the part between C-C' and B-B' was identical on descent and ascent.

Acknowledgments

References

Bricker, O.P., and Prospero, J.M., "Airborne Dust on the Bermuda Island and Barbados," Abstract, EOS Transactions, Vol. 50, 1969, p. 176.

Burns, F.A., "Dust Haze in Relation to Pressure Gradients," Meteorological Magazine, Vol. 90, 1961, pp. 223-226.

Carlson, T.N., and Ludlam, F.H., "Conditions for the Formation of Severe Local Storms," Tellus, Vol. 20, 1968, pp. 203-226.

Carlson, T.N., "Synoptic Histories of Three African Disturbances That Developed Into Atlantic Hurricanes," Monthly Weather Review, Vol. 97, 1969 a, pp. 256-276.

Carlson, T.N., "Some Remarks on African Disturbances and Their Progress Over the Tropical Atlantic," Monthly Weather Review, Vol. 97, 1969 b, pp. 716-726.

Frank, N.L., "The Inverted V Cloud Pattern, An Easterly Wave," Monthly Weather Review, Vol. 97, 1969, pp. 130-140.

Friedman, H.A., Conrad, G., and McFadden, J.D., "ESSA Research Flight Facility Aircraft Participation in the Barbados Oceanographic and Meteorological Experiment," Bulletin of the American Meteorological Society, Vol. 51, 1970, pp. 822-835.

Prospero, J.M., "Atmospheric Dust Studies on Barbados," Bulletin of the American Meteorological Society, Vol. 49, 1968, pp. 645-652.

Prospero, J.M., and Carlson, T.N., "Radon-222 in the North Atlantic Trade Winds: Its Relationship to Dust Transport From Africa," Science, Vol. 167, 1970, pp. 974-977.

Prospero, J.M., and Carlson, T.N., "Mineralogy of Aerosols Collected at Miami, Florida: Evidence for the Frequent Presence of African Dust," Abstract, EOS Transactions, Vol. 52, 1971, p. 370.

Prospero, J.M., Bonatti, E., Schubert, C., and Carlson, T.N., "Dust in the Caribbean Atmosphere Traced to an African Dust Storm," Earth and Planetary Science Letters, Vol. 9, 1970, pp. 287-293.

Warn, G.E., "Some Dust Conditions of the Southern High Plains," Bulletin of the American Meteorological Society, Vol. 33, 1952, pp. 240-243.

EXPERIMENT 19: Study of Tropical Weather Systems During Project BOMEX

PRINCIPAL INVESTIGATOR: Dr. Mariano A. Estoque

AFFILIATION: University of Miami

L.M. Herrera Cantilo and J.J. Fernandez-Partagas of the University of Miami are the authors of the following paper, "Analysis of a Tropical Depression Based on Radar Data," which will be submitted for publication soon.

The tropical depression of July 26, 1969, was chosen for a detailed study of the horizontal motion field defined by the radar echoes observed by the AN/MPS-34 located on Barbados.

Radar data were collected at 2-hour intervals and the resulting motion field was read into a grid whose spacing was 6 mi in the N-S and E-W directions. Vorticity and divergence were computed at each grid point. This process was carried out every 2 hours from 0600 to 1800 GMT.

A study of the vorticity field did not reveal a continuous displacement of one single center of maximum vorticity during that period. Rather, a succession of maxima intensified and weakened, the predominant one arising progressively further north, and all maxima traveling in the same general direction. This evolution appeared closely related to the divergence field, in that developing centers of maximum vorticity fell consistently in areas of strong convergence, while decaying centers were found in areas of divergence.

The field of echo motion was tested with the vorticity equation by computing the following terms: the local rate of change of the absolute vorticity, its horizontal advection, and the divergence term. The vertical advection, the solenoid, and the twisting and friction terms were lumped into a residual. This residual, far from being always negligible, was found to predominate over the other terms at many grid locations. At most of these, however, strong echoes occurred during at least part of the period considered, suggesting large values of the residual terms in areas of heavy convection.

The echo-motion field was compared with the wind field reported by instrumented aircraft. Three aircraft flew through the same area close to 1600 GMT: the NCAR Queen Air, at about 150-m altitude, one RFF DC-6 at 1,500 m, and the RFF DC-4 at 3,000 m. A modest statistical comparison showed that the DC-4 wind speed was consistently smaller than the speed of the echoes, and that wind direction measured by the DC-6 was consistently to the right of echo motion.

EXPERIMENT 35: <u>Wisconsin Atmospheric Radiation Divergence Study</u> (WARDS)

PRINCIPAL INVESTIGATORS: <u>Dr. Kirby J. Hanson[1], Dr. Stephen K. Cox[2],
Dr. Verner E. Suomi[3], and Dr. Thomas H. Vonder Haar[2]</u>

AFFILIATION: [1]Atlantic Oceanographic and Meteorological Laboratories, NOAA,
[2]Colorado State University, and [3]University of Wisconsin.

Reproduced below is a paper on "Measurements of Absorbed Shortwave Energy
in a Tropical Atmosphere," authored by Drs. Cox, Vonder Haar, Hanson, and
Suomi. The paper was presented at the "Meteorological and Atmospheric
Effects" session of the 1971 Conference of the International Solar Energy
Society, Goddard Space Flight Center, Greenbelt, Md., May 11, 1971.

Introduction

The absorption of shortwave radiation (.3 μm to 3 μm) by the earth's
atmosphere is a very basic question in the study of the atmosphere's energy
budget. Whether the sun's energy enters the atmospheric energy cycle directly
or through a transformation to latent or sensible heat determines the response
time of the atmosphere to the solar forcing function. Indeed, solar energy
absorbed in the ocean may be stored in this massive heat reservoir for decades
or centuries. On the other hand, if a significant portion of this energy is
absorbed directly in the atmosphere, it is available to drive the atmosphere's
circulation immediately.

Another important reason for establishing the magnitude of the atmospheric
absorption of shortwave radiation lies in the design of future meteorological
observation programs. These programs have scientific goals that must be
translated into accuracy requirements for observations of various parameters.
The conclusion, from theory, that we know the magnitude of shortwave absorp-
tion in the atmosphere, is premature and we cannot rightfully overlook or
neglect this heat budget component on all scales during all situations with-
out further study.

The work by Roach (1961 a and b), Manabe and Möller (1961), Yamamoto
(1962), and Manabe and Strickler (1964) is that upon which we have based our
comparisons in this paper. Other investigators who have made significant
contributions to the study of shortwave absorption by the atmosphere are
included in the references.

Data

During the months of May, June, and July 1969, observations of heating
rates due to shortwave (.3 μm to 3 μm) (SW) radiation absorption in the
tropical atmosphere were collected as part of the Barbados Oceanographic
and Meteorological Experiment (BOMEX) in the vicinity of Barbados, West
Indies (59.5°W, 12.4°N).

The results presented in this paper were derived from pyranometric meas-
urements of the total hemispheric irradiance measured by upward and downward
facing instruments. The sensors were mounted on a National Center for
Atmospheric Research (NCAR) Queen Air aircraft. The NCAR aircraft flew
successive horizontal passes at a number of preselected altitudes allowing
the aircraft to be advected along with the mean wind; this type of flight
plan provided assurance that the same air column was being sampled on con-
secutive passes.[1] The upward and downward irradiance data were then normal-
ized with respect to the solar-terrestrial geometry.

Data were collected in 3-min horizontal aircraft passes at various alti-
tudes. The pyranometers were sampled every second, and sample averages were
formed from the data to obtain the upward and downward irradiance at that
level.

Results

Figure 1 shows the mean downward irradiance as a function of height ob-
tained from five different cloud-free ascents on three different days.

The bar through each observed data point depicts the standard deviation
of the observations. The series of points to the right of the observed curve
was computed by a scheme taken from the work by Manabe and Strickler (1964)
for a cloud-free gaseous atmosphere. Slight modifications to their technique
involved use of 1.95 cal cm^{-2} min^{-1} as the solar constant and a mass dependent
correction for Rayleigh scattering. The observed mean moisture profile for
the five aircraft observation dates were used in the calculation. A third
series of points were taken from Kondratyev and Nikolsky (1968). This last
set represents the downward irradiance observed by a balloon-borne actinometer
in an atmosphere with a water vapor optical mass of 4.7 gm cm^{-2} - the same
mean total optical mass for the observations at Barbados. Comparison of these
three versions of the downward SW irradiance showed observed irradiance at all
levels to be consistently lower than the calculated.

Let us now define the fractional absorption as proposed by Yamamoto (1962).
If Hnet at a given level is the net shortwave irradiance level, the fractional
absorption, f_a, for that layer is given by

$$f_a = \frac{Hnet_{top} - Hnet}{SC} , \tag{1}$$

---

[1]Aircraft performance allowed a typical flight sounding (five levels between
surface and 20,000 ft) to be completed in 45 min; only data from flights
within 2 hours of local noon were considered.

where SC is the solar constant, and Hnet$_{top}$ is the SW irradiance at the top of the atmosphere. A heating rate can be computed from

$$\frac{\Delta T}{\Delta t} = \frac{g}{Cp} \frac{\Delta Hnet}{\Delta p} , \qquad\qquad (2)$$

where g is acceleration of gravity, Cp is the specific heat of dry air, and Δp is the pressure increment of the layer.
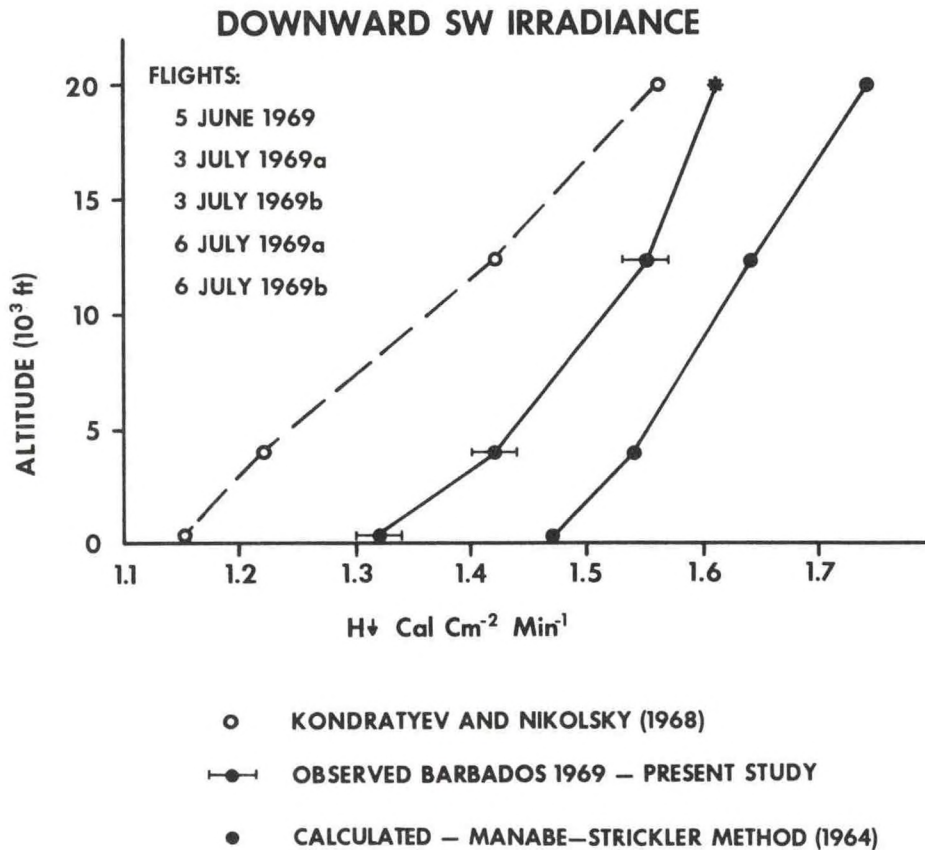
DOWNWARD SW IRRADIANCE

Figure 1. *Mean observed and calculated downward solar irradiance at the surface in an atmosphere with 4.7 cm precipitable water.*

Figure 2 shows a comparison of the fractional absorption computed from (1) based on observed Hnet values (points with absolute dispersion bars) and calculated absorption values. Hnet$_{top}$ was deduced from measurements of reflected and scattered solar radiation from Nimbus III MRIR data, with an assumed solar constant of 1.95 (Vonder Haar et al., 1971). A minimum planetary albedo of 10 was chosen as representative of the cloudless case near the Barbados region during July.

The observed fractional values shown in figure 2 are consistently higher than the calculated. The departure increases toward the surface where the observed fractional absorption for the five cloud-free ascents is more than 20 percent greater than the calculated. One is tempted to compute observed heating rates from the mean data shown in figure 2, but this may be misleading since the absolute dispersion shown could account for either greater or less heating than the calculated.
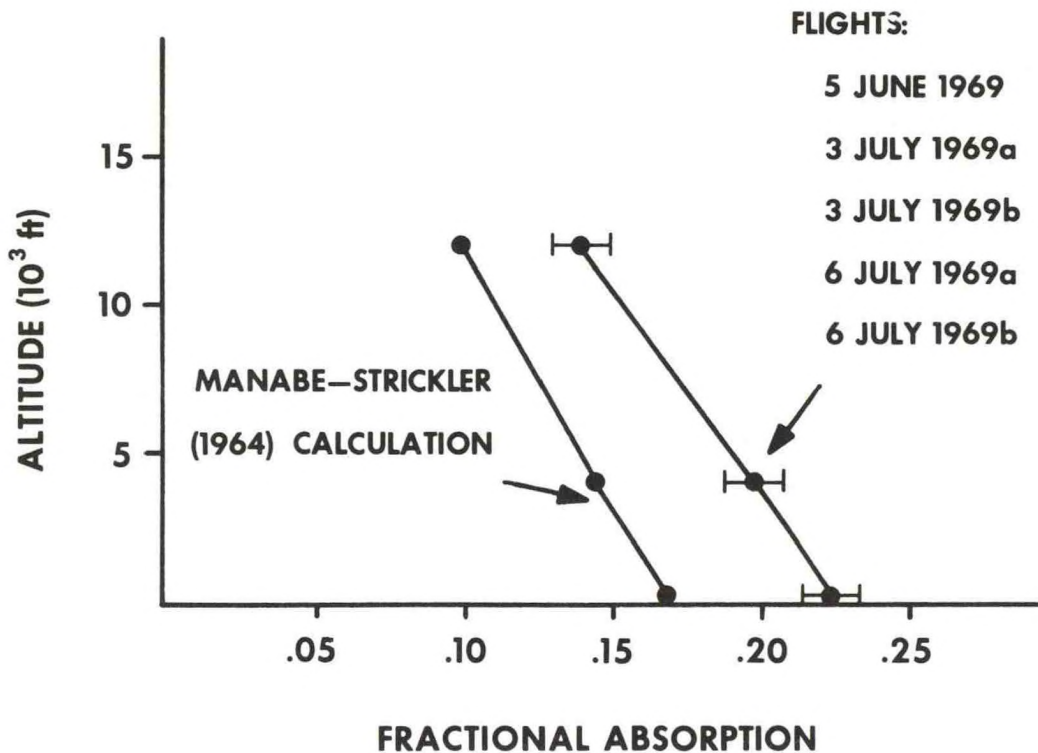

Figure 2. Observed and calculated mean fractional absorption in a tropical atmosphere.

For a comparison of heating rates we selected one flight, June 5, 1969, and calculated heating rates by the Roach (1961*a*) and Manabe-Strickler (1964) method. These results are shown in figure 3, where we see that the calculated heating rates are 30 percent lower than the observed in the lowest 4,000 ft and in reasonable agreement between 4,000 and 8,000 ft.
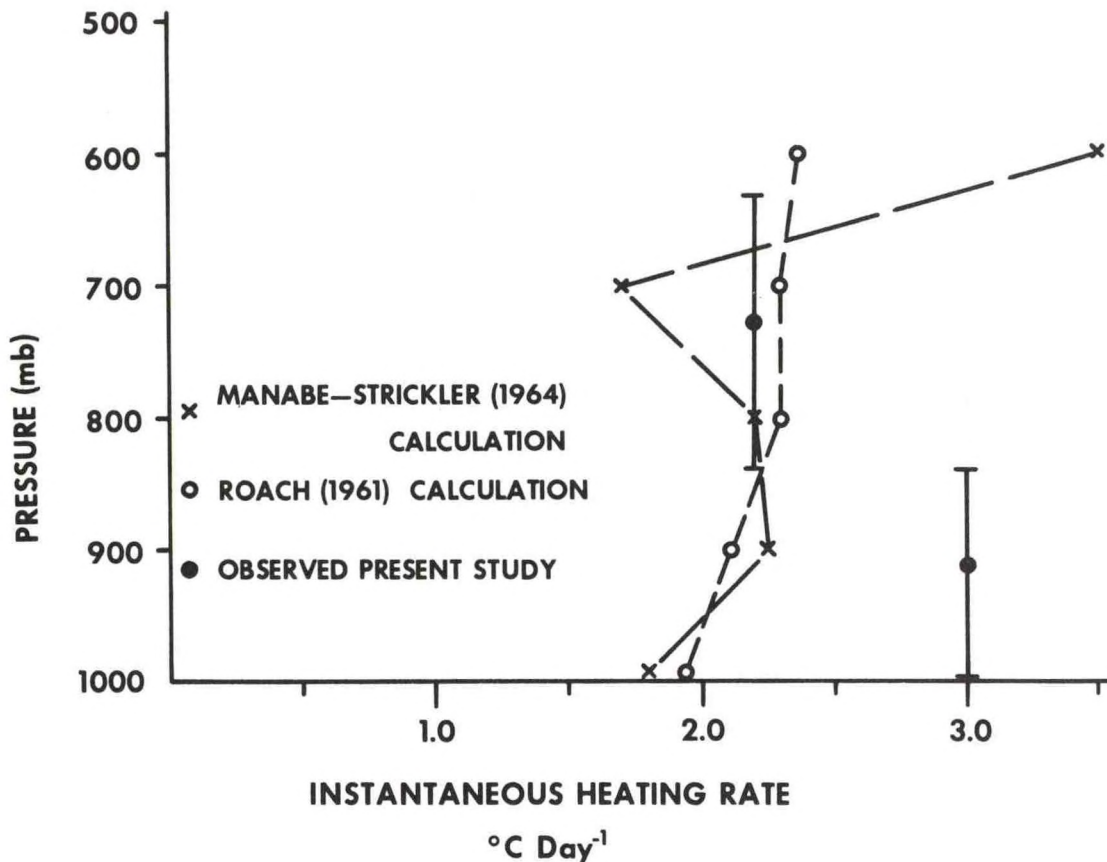
*Figure 3.   Instantaneous heating rates observed and
calculated for a tropical atmosphere (4.7
cm precipitable water; 13° N; 1100 local time).*

Each of the comparisons shown in figures 1 to 3 indicates that there is something in the real atmosphere that is absorbing shortwave energy in excess of the calculated values. As stated earlier, all observed cases were cloud-free. Physically, this directs attention to (a) the presence of "haze"; (b) additional amounts of waver vapor; or, perhaps, (c) uncertainties in the basic absorption data as applied in the computation to nonhomogeneous paths as possible explanations for the observed/computed discrepancies.

16

Of the three explanations offered above, the presence of haze seems most plausible. Haze in the tropics results from a concentration of aerosols, which may be either pure water, dilute solutions of NaCl or water-coated dust particles. We feel that it is highly unlikely that dry dust particles would be present in a near-saturated environment. Prospero and Carlson (1970) report atmospheric dust concentrations in excess of 10 $\mu gm \; m^{-3}$ to be not uncommon during June and July. In any event, by putting forth the haze hypothesis we do not at this time question any of our basic gaseous absorption data or empirical computation technique to qualitatively explain the greater observed absorption values. Haze may absorb the SW energy directly or it can cause a longer path through the absorbing gaseous constituents by scattering; either explanation (or a combination) would result in increased absorption.

If subsequent study supports the "haze effect" hypothesis, the relative magnitude of the difference between the calculated and observed SW heagint may provide a meaningful "haze index."

Let us consider again figure 3. The greater-than-calculated observed value of SW heating in the layer from 820 to 1,000 mb includes the vertical layer normally occupied by trade cumulus clouds (base 1,700 ft; top 2,000 to 4,000 ft), and this layer normally contains sufficient aerosol to distinctly affect visibility. Even in the cloud-free data flights shown in figures 1 to 3 the horizontal visibility in this lower layer was significantly less than would be expected from a strictly gaseous atmosphere. Therefore we conclude that the aerosol affecting visibility is also responsible for the enhanced absorption of shortwave energy either by the scattering effect or direct absorption mentioned above. Kuhn (1970, personal communication) and Cox (1969) report larger than expected infrared cooling of the lower layers of the tropical atmosphere; this measured anomaly also points to the presence of aerosol in these layers.

Conclusions

Initial analysis of aircraft measurements of shortwave irradiance in a cloudless atmosphere shows larger absorption by the atmosphere than can be explained by the gaseous constituents alone. In the case presented, the observed heating rate is 50 percent greater than the calculated for the lowest 4,000 ft of the atmosphere. We feel that in the presence of a low cloud deck the absorption will be even greater in this layer. On the basis of these preliminary results we suggest that the role of solar radiation absorbed directly by the atmosphere in the tropics has been seriously underestimated. A check on this statement must await analysis, now underway, of additional data.

Acknowledgements

References

Angstrom, A., "Atmospheric Turbidity, Global Illumination and Planetary Albedo of the Earth," Tellus, Vol. 14, 1962, pp. 435-450.

Cox, S., "Observational Evidence of Anomalous Infrared Cooling in a Clear Tropical Atmosphere," Journal of the Atmospheric Sciences, Vol. 26, 1969, pp. 1347-1349.

Cox, S., and Hastenrath, S., "Radiation Measurements Over the Equatorial Central Pacific," Monthly Weather Review, Vol. 98, 1970, pp. 823-832.

Davis, P., "An Analysis of the Atmospheric Heat Budget," Journal of the Atmospheric Sciences, Vol. 20, 1963, pp. 5-22.

Fritz, S., Rao, P.K., and Weinstein, M., "Satellite Measurements of Reflected Solar Energy and the Energy Received at the Ground," Journal of the Atmospheric Sciences, Vol. 21, 1964, pp. 141-151.

Hanson, K., Vonder Haar, T., and Suomi, V., "The Reflection of Sunlight to Space and Absorption by the Earth and Atmosphere Over the United States During Spring, 1962," Monthly Weather Review, Vol. 95, 1967, pp. 354-361.

Hougton, H., "On the Annual Heat Budget of the Northern Hemisphere," Journal of Meteorology, Vol. 11, 1954, pp. 1-9.

Kondratyev, K., Nikolsky, G., Badinov, I., and Andreev, S., "Direct Solar Radiation up to 30 km and Stratification of Attenuation Components in the Stratosphere," Applied Optics, Vol. 6, 1967, pp. 197-207.

Kondratyev, K., and Nikolsky, G., "Direct Solar Radiation and Aerosol Structure of the Atmosphere From Balloon Measurements in the Period of IQSY," Sveriges Meteorologiska och Hydrologiska Institut, Meddelanden, Ser. B, No. 28, 1968.

Korb, G., and Möller, F., "Theoretical Investigation of Energy Gain by Absorption of Solar Radiation in Clouds," Final Technical Report - Contract DA-91-591 EUC-1612, Ludwig-Maximilians-Universität, Meteorologisches Institut, Munich, Germany, 1962, 185 pp.

London, J., "A Study of the Atmospheric Heat Balance," Final Report, Contract AF 19(122)-165, Department of Meteorology and Oceanography, New York University, 1957, 99 pp.

Manabe, S., and Möller, F., "On the Radiative Equilibrium and Heat Balance of the Atmosphere," Monthly Weather Review, Vol. 89, 1961, pp. 503-532.

Manabe, S., and Strickler, R., "Thermal Equilibrium of the Atmosphere With a Convective Adjustment," Journal of the Atmospheric Sciences, Vol. 21, 1964, pp. 361-385.

Prospero, J., and Carlson, T., "Radon-222 in the North Atlantic Trade Winds: Its Relationship to Dust Transport From Africa," Science, Vol. 167, 1970, pp. 974-977.

Raschke, E., "On the Parameterization of Solar Radiative Energy Absorbed in the Earth-Atmosphere System," Paper presented to the NOAA Workshop on Remote Sensing, Atlantic Oceanographic and Meteorological Laboratories, Miami, March 1971.

Roach, W., "Some Aircraft Observations of Fluxes of Solar Radiation in the Atmosphere," Quarterly Journal of the Royal Meteorological Society, Vol. 87. 1961 a, pp. 346-363.

Roach, W., "The Absorption of Solar Radiation by Water Vapor and Carbon Dioxide in a Cloudless Atmosphere," Quarterly Journal of the Royal Meteorological Society, Vol. 87, 1961 b, pp. 364-373.

Vonder Haar, T., and Hanson, K., "Absorption of Solar Radiation in Tropical Regions," Journal of the Atmospheric Sciences, Vol. 26, 1969, pp. 652-655.

Vonder Haar, T., Raschke, E., Bandeen, W., and Pasternak, M., "Measurements of Solar Energy Reflected by the Earth and Atmosphere from Meteorological Satellites," Paper presented at Solar Energy Society Conference, Goddard Space Flight Center, Greenbelt, Md., 1971.

Vonder Haar, T., Cox, S., and Hanson, K., "Measurements of Solar Radiation Absorption in the Tropical Atmosphere: Preliminary Results," Annual Report Grant E-230-68, Space Science and Engineering Center, University of Wisconsin, 1969, pp. 143-152.

Yamamoto, G., "Direct Absorption of Solar Radiation by Atmospheric Water Vapor, Carbon Dioxide and Molecular Oxygen," Journal of the Atmospheric Sciences, Vol. 19, 1962, pp. 182-188.

EXPERIMENT 36: In Situ Water Vapor Measurements by Means of an Aluminum
  Oxide Hygrometer

PRINCIPAL INVESTIGATOR: Mr. Ernest K. Hilsenrath

AFFILIATION: Goddard Space Flight Center, NASA

"Performance of an Aluminum Oxide Hygrometer on the NASA Convair CV 990
Aircraft Meteorological Observatory," by E. Hilsenrath and E.L. Coley, is
available from the authors in the form of a preprint, X-651-71-37, January
1971. Only the abstract is included here.

An aluminum oxide hygrometer has been flown on the NASA Convair 990 air-
craft on several meteorological expeditions, including BOMEX and the June 1970
flights over the Arctic Ocean, the continental United States, and the Gulf of
Mexico. Water vapor data are available for most of these flights. A standard
aluminum oxide probe was mounted in a specially designed air sampler. A con-
trol unit was designed such that the hygrometer system would be compatible
with the flight environmental computer flown on board the 1970 expedition.
Comparisons were made with other aircraft measurements yielding water vapor
data and with humidity data from radiosondes, when available. These compari-
sons substantiate the validity of the suggested corrections to radiosonde data
obtained during BOMEX. These flights have also demonstrated the negligible
temperature dependence of the hygrometer data and the rapid time response of
the configuration flown in a jet aircraft, which yield useful water vapor data
in the range from +15°C to -60°C.

EXPERIMENT 37, 38: Basic Synoptic Scale Water Vapor, Energy and Momentum
  Budgets

PRINCIPAL INVESTIGATORS: Dr. Joshua Z. Holland and Dr. Eugene M. Rasmusson

AFFILIATION: BOMAP Office, Environmental Research Laboratories, NOAA

Based on data now available in preliminary processed form ("A_0" data), a
series of trial integral calculations have been designed, consisting of in-
creasingly complex computations covering progressively longer time periods.
These calculations are being undertaken with the following objectives:

(1) Uncovering data problems and testing methods for correcting known
     deficiencies.

(2) Developing analytical and computational techniques for evaluating
     the budget equations developed in "Mass, Momentum, and Energy Budget
     Equations for BOMAP Computations," by E.M. Rasmusson, NOAA Technical
     Memorandum ERL BOMAP-3, January 1971.

(3) Ensuring optimum use of all data obtained from the various sensors and systems used during BOMEX.

(4) Providing error estimates of the various terms in the equations.

(5) Documenting problems and results as the anlyses progress.

Resulsts of these and related efforts in support of Experiment 37, 38 - the BOMEX Core Experiment - are reflected in papers given by several members of the BOMAP staff at the 52nd Annual Meeting of the American Geophysical Union, April 12-16, 1971, Washington, D.C. The papers presented are contained in section II of this Bulletin.

EXPERIMENT 41: Ocean Environmental Effects on Surface Schooling Tuna

PRINCIPAL INVESTIGATOR: Dr. James F. Hebard

AFFILIATION: Tropical Atlantic Biological Laboratories, National Marine Fisheries Service, NOAA

Salinity-temperature-depth (STD) data from 38 stations from the June and July 1969 surveys by the research vessel *Undaunted* have been deposited with the National Oceanographic Data Center (NODC) for processing into the standard NODC-BOMEX format on magnetic tape. These will be available for distribution in the summer of 1971. See BOMEX Bulletin No. 8 for further details on this experiment.

EXPERIMENT 42: Oceanic Thermal Structure Prediction

PRINCIPAL INVESTIGATORS: Dr. R.W. James and Mr. George L. Hansen

AFFILIATION: U.S. Naval Oceanographic Office

A 10-min 16-mm time-lapse film of salinity-temperature-depth (STD) profiles has been made and is available. Dr. James will obtain STD data for BOMEX Period III from the BOMEX Temporary Archive and will analyze them for gross temperature and salinity structure.

EXPERIMENT 44: Lidar Measurements During BOMEX

PRINCIPAL INVESTIGATORS: Dr. Warren B. Johnson and Dr. Edward E. Uthe

AFFILIATION: Stanford Research Institute

The principal investigators' final report has been completed, entitled "Lidar Observations of the Lower Tropospheric Aerosol Structure During BOMEX," Final report submitted to the Atomic Energy Commission, Contract AT9043-155, Stanford Research Institute, Menlo Park, Calif., January 1971. The abstract of this report follows.

A lidar (laser radar) was flown on a U.S. Air Force WC-130B aircraft over the BOMEX area during the third experimental period (20 June to 3 July 1969). The instrument used a neodymium laser (1.06-μm wavelength) and had a firing rate of approximately one pulse per 3.5 sec. A total of 5,192 lidar signatures were collected during the eight flight missions. Most of the observations were obtained over the eastern portion of the BOMEX area at an altitude of 10,000 ft and an aircraft speed of 100 m/sec, with a lidar pointing angle of 60° below the horizon. Under these conditions, the backscattered signal was generally above the receiver noise level over the complete path to the surface. The data are of sufficient spatial extent to allow presentation in terms of vertical cross sections of optical density.

A computer technique is described that adjusts and corrects the data for the range effect, instrumentation nonlinearities, and pulse-to-pulse variations in transmitted energy, and then objectively performs a contour analysis of the resulting data matrix. Vertical cross sections of normalized lidar signal return obtained in this way are presented along with the associated average vertical profiles. These lidar results are interpreted qualitatively in terms of changes in aerosol density and/or particle size in the lowest 3,000 m of the atmosphere. They are compared with vertical profiles of temperature, dew point, and the radionuclides [7]Be and [95]Zr, which were obtained from supplementary data sources.

The data analyzed clearly reveal the existence of well-defined scattering layers associated with the sub-cloud layer, the trade-wind inversion, and the Sahara dust stream. The sub-cloud layer was nearly always present and its top extended to an average height of 610 m (standard deviation of 110 m) with nearly a constant scattering amplitude (standard deviation of 0.7 dB). The height of this layer was well correlated with a change in stability typically shown by the temperature and dew-point profiles. Near cloud tops the air typically gave less signal return, indicating cleaner or drier conditions.

The height, thickness, density and structure of the Sahara dust layer showed large vertical and horizontal variability. The average aerosol scale height determined from this study was 1.48 km (standard deviation of 0.7 km). The large scale heights result from the presence of the elevated dust layer. The decrease in scattering normally observed above the base of an elevated inversion in continental regions was not usually found at the trade-wind inversion in this experiment, because of the typical presence of a dust layer above the inversion. The base of this layer frequently appeared to be trapped by the inversion, preventing downward movement.

22

Lidar returns favorably compare with signatures synthesized by using measured particle size distributions and Mie theory. This indicates that useful quantitative information on aerosol density can be inferred from lidar measurements over an extended period of time. However, such inferences are subject to errors introduced by nonlinear variations between aerosol density and the volume backscatter coefficient.

EXPERIMENT 46: Radiation Experiment

PRINCIPAL INVESTIGATORS: Dr. Peter M. Kuhn and Mrs. Lois P. Sterns

AFFILIATION: Environmental Research Laboratories, NOAA

Abstracts of two papers related to this experiment appeared in BOMEX Bulletin No. 7 and will not be repeated here. Titles of these papers are: "Altering the Tropical Radiation Norm," by P.M. Kuhn, Bulletin of the American Meteorological Society, Vol. 51, No. 3, March 1970; and "Interaction of Radiation and Climate - BOMEX Experiment," by P.M. Kuhn and L.P. Stearns, EOS Transactions, AGU, Vol. 51, No. 4, April 1970.

Further results have now been published or have been submitted for publication. Abstracts of these papers are given below.

"Airborne Observations of Contrail Effects on the Thermal Radiation Budget," by P.M. Kuhn, Journal of Atmospheric Sciences, Vol. 27, No. 6, September 1970.

Direct infrared and solar radiometric observations were made to analyze the effects on the environment of any alterations in the radiation budget in regions of heavy jet traffic. The observations, made from the NASA Convair 990 jet laboratory, were coupled with Mie scattering and absorption theory calculations to analyze any inadvertent alterations in the natural atmospheric thermal radiation budget. It was found a 500-m-thick contrail sheet increases the infrared emission below the sheet by 21 percent but decreases the solar power below the sheet by 15 percent. The infrared increase cannot make up for the solar depletion, resulting in a net available thermal power at the earth's surface, which in turn results in a 5.3°C decrease in the surface temperature, if we assume contrail persistence. The actual temperature decrease is ~0.15°C with 5 percent contrail persistence.

"Radiative Transfer Observations and Calculations During BOMEX," by P.M. Kuhn and L.P. Stearns, NOAA Technical Report ERL 203-APCL 19, April 1971.

During the Barbados Oceanographic and Meteorological Experiment in 1969, over 220 balloon-borne radiometersonde ascents were made from the NOAA research vessels *Discoverer* and *Rainier,* the U.S. Coast Guard vessel *Rockaway* and the Seawell Airport on Barbados. The radiative power derived from these ascents provided a massive comparison between observed values and calculations using the temperature and moisture profiles of the radiosonde. A summary and brief analysis of the observations and calculations by the radiative transfer equation is examined, along with comments on the radiative cooling.

"Radiosonde Humidity Retrieval by Simultaneous Radiation Measurements," by P.M. Kuhn and L.P. Stearns, Submitted to Journal of Meteorology.

A radiometric method for the retrieval of moisture data at altitudes above the radiosonde hygristor cutoff region or in situations where a malfunction of the hygristor occurs is described. The method was applied to BOMEX radiation soundings. Regardless of the exact moisture profile, the method is designed to radiometrically infer the average decrease of moisture through the entire atmospheric column through a solution of the radiative transfer equation. This enables recovery of the total mass of atmospheric water vapor.

In at least 25 percent of all BOMEX radiometersonde ascents, humidity retrieval did produce a more realistic moisture profile and total mass of precipitable water vapor. In these cases, the radiosonde hygristor humidity deficiencies averaged from -45 percent at 800 mb to -30 percent at 600 mb. For such pressure levels, the optical mass of water vapor retrieved for the soundings discussed averaged 1.68 gm cm^{-2}. This represents 56 percent of the hygristor-measured optical mass. Above 400 mb the optical mass recovered averaged 0.7 gm cm^{-2} for all BOMEX radiometer soundings. It is suggested that a simple radiometer could be used to improve moisture measurements for soundings requiring the best possible water vapor data.

"Parameterizing Continuum Radiation to Remove the Computed-Observed Radiation Discrepancy," Paper presented at Atlantic Oceanographic and Meteorological Laboratories Workshop on Remote Sensing, March 29, 1971, Miami.

BOMEX and the 1970 International Radiometersonde Intercomparison radiometersonde and radiosonde ascent data were the basis for a parameterization of continuum radiation in a computer model of the radiative transfer equation (RTE). In situ (aircraft) measurements of particle size during radiometersonde ascent and some aerosol sizing allowed inclusion of a fourth integral for atmospheric particulates (in addition to those for water vapor, carbon dioxide and ozone) in the RTE. Transmission functions were obtained for

10 cm^{-1} intervals from 730 to 1300 cm^{-1}. Addition of the continuum emission and transmission integrals to the RTE reduced discrepancies between computed and measured downward radiant emittance from a total column average of 50.0 watts m^{-2} to 10.0 watts m^{-2}. It is shown that clouds can account for the remaining 10 watts cm^{-2} difference. These changes did not appreciably affect the upward calculated and measured radiant emittance differences which are relatively small.

EXPERIMENT 56: Nimbus 3 Study of Various Environmental Parameters[1]

EXPERIMENT 57: Nimbus 3 Study of Aerosol Distribution[1]

EXPERIMENT 58: Measurements and Interpretation of the Sea-Surface and Air Temperature Gradients in the Sub-Cloud Layer During BOMEX[2]

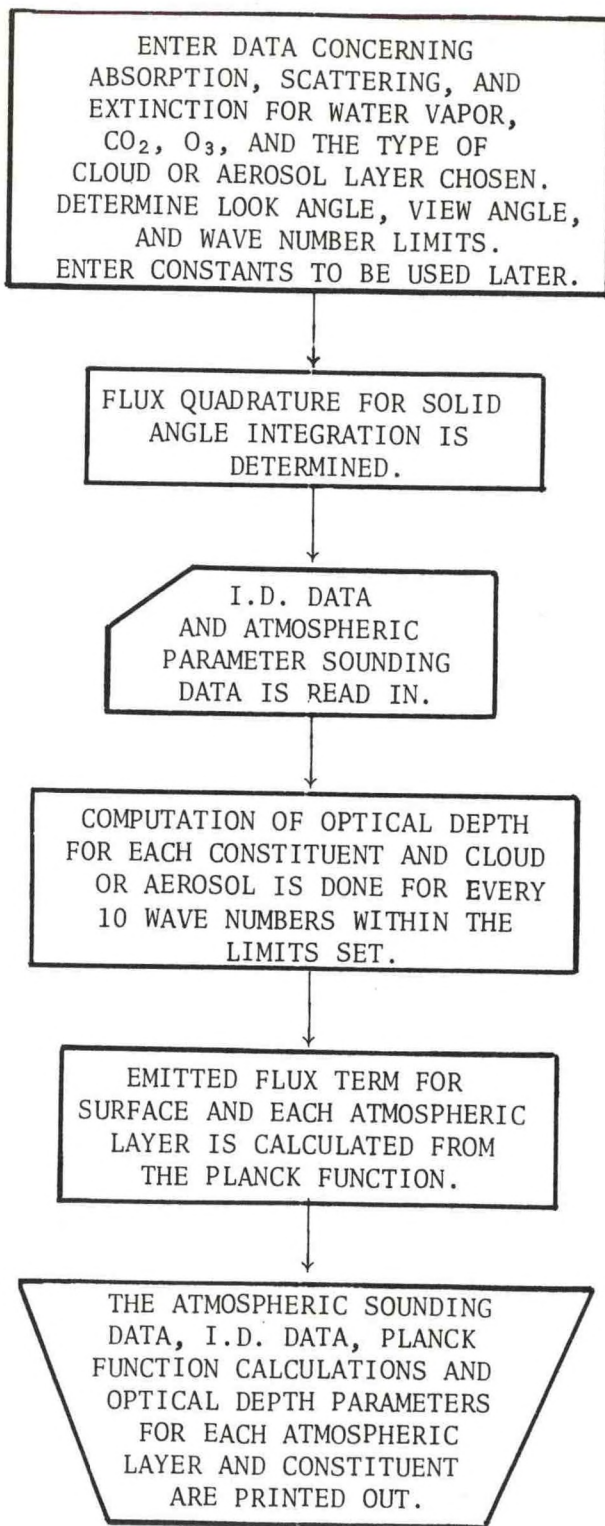PRINCIPAL INVESTIGATORS: [1]Dr. W. Marlatt, [2]Dr. W. Marlatt and Dr. W. Gray

AFFILIATION: Colorado State University

On Experiments 56 and 57, the data are available from Mr. William Bandeen, Goddard Space Flight Center, NASA, Greenbelt, Md. Concerning these two experiments, the following final report has been published: "Infrared Radiation Transfer Through Atmospheric Haze Layers," Final Report: NAS 5-11631, "Atmospheric Limitations to Remote Sensing," by W.E. Marlatt, H.L. Cole, J.C. Harlan, and J.I. Hjermstad, Department of Watershed Sciences, Colorado State University. This report includes analysis of atmospheric particulates encountered by the NASA Convair 990 during BOMEX as well as some cases where observed radiometric sea surface temperatures were compared with sea surface temperature values calculated by a mathematical atmospheric model. The comparisons showed that atmospheric aerosols contributed as much as 20 percent of the attenuation of infrared radiation between the sea surface and the airborne radiometer.

The technique used to determine the aerosol effect was as follows:

(1) Calculations were undertaken by a mathematical model of atmospheric infrared radiation transfer, RADIANV, a block diagram of which is included. The atmospheric parameter data were supplied from aircraft and/or ship radiosonde data. The program then calculated the radiation values which should have been observed by the airborne radiometer if no particulate matter was between the sea surface and the aircraft.

(2) Comparisons were made between the observed values and the calculated values of sea surface temperature with the difference being attributed to the atmospheric particulate attenuation of infrared radiation.

ENTER DATA CONCERNING
ABSORPTION, SCATTERING, AND
EXTINCTION FOR WATER VAPOR,
CO_2, O_3, AND THE TYPE OF
CLOUD OR AEROSOL LAYER CHOSEN.
DETERMINE LOOK ANGLE, VIEW ANGLE,
AND WAVE NUMBER LIMITS.
ENTER CONSTANTS TO BE USED LATER.

FLUX QUADRATURE FOR SOLID
ANGLE INTEGRATION IS
DETERMINED.

I.D. DATA
AND ATMOSPHERIC
PARAMETER SOUNDING
DATA IS READ IN.

COMPUTATION OF OPTICAL DEPTH
FOR EACH CONSTITUENT AND CLOUD
OR AEROSOL IS DONE FOR EVERY
10 WAVE NUMBERS WITHIN THE
LIMITS SET.

EMITTED FLUX TERM FOR
SURFACE AND EACH ATMOSPHERIC
LAYER IS CALCULATED FROM
THE PLANCK FUNCTION.

THE ATMOSPHERIC SOUNDING
DATA, I.D. DATA, PLANCK
FUNCTION CALCULATIONS AND
OPTICAL DEPTH PARAMETERS
FOR EACH ATMOSPHERIC
LAYER AND CONSTITUENT
ARE PRINTED OUT.

The next steps to be taken in our analysis are as follows:

(1) To model the size distribution of typical atmospheric particulate conditions encountered during BOMEX according to the data collected in Experiments 57 and 58.

(2) To use the particulate models as input to RADIANV along with the other atmospheric parameter data in order to determine the effect on radiation transfer of varying concentrations and particle size distributions.

The accompanying simplified flow chart illustrates the radiation transfer program RADIANV now being used. Originally developed by S. Cox and P. Kuhn, it has been modified to handle atmospheric particulate data as well as constituent data. For atmospheric particulates, the extinction, scattering, and absorption volume cross sections must be calculated by another computer program and then entered in the first block of RADIANV.

Preliminary results of analysis of data of infrared radiation transfer through atmospheric particulates during BOMEX were presented by Dr. W. Marlatt and Mr. C. Harlan at the BOMEX Radiation and Particulate Conference held at the National Center for Atmospheric Research, Boulder, Colorado, October 1970.

All data for Experiment 58 are available at the BOMAP Office. Dr. W. Gray is now analyzing portions of the data. It might also be noted that some data from this experiment are included in the report on "Infrared Radiation Transfer Through Atmospheric Haze Layers," referred to above.

A National Science Foundation research grant entitled "An Investigation of the Effects of Atmospheric Particulates on the Radiometric Measurement of Sea Surface Temperature and on Infrared Cooling Rates in the Troposphere During BOMEX" has been awarded Dr. Marlatt as principal investigator. Under this grant, an analysis of the aerosol and radiometer data collected for BOMEX Experiments 57 and 58 will be undertaken to define quantitatively the role of atmospheric particulates in attenuating infrared radiation. A paper was given at the Seventh International Symposium on Remote Sensing of the Environment at Ann Arbor, Michigan, May 1971, in which preliminary results of this work were discussed.

EXPERIMENT 65: Photographic Study of the Generation and Concentration of Oceanic White Caps

PRINCIPAL INVESTIGATOR: Dr. Edward C. Monahan

AFFILIATION: University of Michigan

Results of this BOMEX experiment are included in a paper by Dr. Monahan, "Oceanic Whitecaps," which appeared in the April 1971 issue of Journal of Physical Oceanography. With the permission of the American Meteorological Society the abstract of the article is quoted below.

The variation of oceanic whitecap coverage with wind speed was determined from the analysis of groups of five or more photographs taken, along with measurements of wind speed and air and water temperatures, during each of 71 observation periods at locations on the Atlantic Ocean and adjacent salt water bodies. The fraction of the sea surface covered by whitecaps is always <0.1% for wind speeds $V<4$ m sec^{-1}. For winds from 4 to 10 sec^{-1} the maximum percentage of the sea surface covered by whitecaps is given by $W=0.00135\ V^{3.4}$

EXPERIMENT 70: Measurement of Humidity and Temperature Fluctuations and Turbulent Transport of Latent and Sensible Heat

PRINCIPAL INVESTIGATOR: Dr. G. Stephen Pond

AFFILIATION: Oregon State University

The following is an abstract of a paper, to be published, on "Measurements of the Turbulent Fluxes of Momentum, Moisture and Sensible Heat Over the Ocean," by S. Pond, G.T. Phelps, and J.E. Paquin, Oregon State University, and G. McBean and R.W. Stewart, University of British Columbia.

This paper describes results of measurements of the fluxes of momentum, moisture and sensible heat by both the eddy correlation and "dissipation" techniques. The data were collected on FLIP during BOMEX and during a pre-BOMEX trial cruise near San Diego in February 1969. The results are mainly based on data collected by personnel from Oregon State University and the University of British Columbia. We are grateful to the University of Washington personnel who have made their data and results available to us to check some of our results and allowed us to use their temperature fluctuation data from the San Diego cruise when our equipment failed to provide such data.

The methods of determining the fluxes are discussed. The instrumentation and methods of data analysis are described. The effects of FLIP's interference on the flow are described and the method of removing the interference from the results is given. The spectra of the three components of velocity fluctuations and the cospectra between the vertical velocity fluctuations, w, and the downstream velocity, u, temperature, T, and humidity, q, fluctuations are presented. The fluxes determined by the eddy correlation method are compared

with fluxes estimated from the rates of dissipation of kinetic energy and scalar fluctuations. These fluxes are then used to evaluate the constants in the bulk aerodynamic formulae for estimating the fluxes.

The normalized velocity component spectra and the normalized uw cospectra appear to have universal forms and are similar to earlier results. The normalized wT cospectra do not appear to have a universal form. The normalized wq cospectra do appear to have a universal form and are very similar to the normalized uw cospectra. As has been found before, the dissipation and eddy correlation methods agree quite well on average for the momentum flux. The two methods do not give the same results for the sensible heat flux for BOMEX although there is fair agreement for the small number of San Diego results. The two methods do give good agreement for the moisture flux. Comparison of the eddy correlation flux for momentum with the mean wind speed squared leads to a drag coefficient of 1.5×10^{-3}. The sensible heat flux, however, does not show a good relationship with the mean wind speed times the mean sea-air temperature difference during BOMEX. For the San Diego results the relationship is fair and similar to other measurements. The moisture flux shows a strong correlation with the wind speed times the mean sea-air humidity difference. The non-dimensional aerodynamic evaporation coefficient (corresponding to the drag coefficient for momentum) was found to be 1.2×10^{-3} with an uncertainty of about 20 percent. This result based on direct measurements of the flux agrees rather well with some earlier indirect estimates based on evaporation pan data.

EXPERIMENT 84: Atmospheric Nuclei Concentrations

PRINCIPAL INVESTIGATORS: Dr. Helmut K. Weickmann and Dr. Paul A. Allee

AFFILIATION: Environmental Research Laboratories, NOAA

During the BOMEX project, the Atmospheric Physics and Chemistry Laboratory made airborne measurements of the Aitken nuclei, cloud droplet condensation nuclei, and ice nuclei concentrations from one of the DC-6's of the NOAA Research Flight Facility. Results of averaging airborne measurements of the Aitken nuclei and cloud droplet condensation nuclei (at 1 percent supersaturation) have been obtained with respect to altitude for all flight data acquired.

The average Aitken nuclei concentration is less than 350 nuclei ml^{-1} at all flight levels, including 12,000 ft.

The surface concentration of Aitken nuclei was measured at sea level aboard the *Discoverer* and the average concentration was found to be 190 nuclei ml^{-1}. During 1928 the research ship *Carnegie* in the same area during late summer measured the Aitken nuclei concentration at an average of 185 nuclei ml^{-1}. From a comparison of the two results it appears that there has been little or no increase in the concentration of atmospheric particulates in the BOMEX area during the last 41 years.

The cloud droplet condensation nuclei (at 1 percent supersaturation) was measured at a concentration of less than 200 nuclei ml^{-1} at all levels, up to and including the 12,000-ft level.

Results of the ice nuclei concentration measurements are being studied for their relationship to other parameters recorded during the flights.

EXPERIMENT 95: Day-to-Day Variation of Divergence in Trade Wind Region

PRINCIPAL INVESTIGATOR: Mr. Robert W. Reeves

AFFILIATION: BOMAP Office, Environmental Research Laboratories, NOAA

Tentative analytical results related to this experiment are presented in "Preliminary Velocity Divergence Computations for BOMEX Volume Based on Aircraft Winds," by R.W. Reeves, NOAA Technical Memorandum ERL BOMAP-5, April 1971. These preliminary calculations of the horizontal velocity divergence are based on a limited sample of wind measurements from line integral aircraft night flights around the perimeter of the BOMEX volume at a level of 1,000 ft and stepped soundings at seven different heights at the midpoint of each side of the volume. The results indicate that,with careful systematic calibration, such aircraft-measured wind data may be useful in determining divergence.

EXPERIMENT 98: Sea Surface and Cloud Photography From the CV-990

PRINCIPAL INVESTIGATORS: Mr. John Semyan and Mr. William Vetter

AFFILIATION: Goddard Space Flight Center, NASA

The Convair 990 cloud photographs referred to in BOMEX Bulletin No. 8 were all taken during BOMEX Observation Period IV. Flight data, including times that cameras were on and off, are given in the first volume of "Support Data for NASA Convair 990 Meteorological Flight V July 2-July 29, 1969," published by the Department of Atmospheric Science, Colorado State University, December 1969. This volume includes a summary of photographic coverage (p. 8). The second volume contains the flight tracks. Four cameras were operated, 35 mm port, 35 mm starboard, 35 mm downward, and 70 mm downward. Pictures were taken every 10 sec by all cameras.

Limited quantities of duplicates of selected photographs can be made available to responsible investigators. Requests should be directed to Mr. Joseph Steranka, Code 650, Goddard Space Flight Center, Greenbelt, Md. 20771.

II. BOMAP PAPERS PRESENTED AT AGU MEETING

At the 52nd Annual Meeting of the American Geophysical Union, April 12-16, 1971, five papers related to the BOMEX Core Experiment were presented. Pending formal publication at a later date, these papers are reproduced here to convey, in preliminary form, the results to date of analyses in progress.

Interim Report on Results From the BOMEX Core Experiment

Joshua Z. Holland
BOMAP Office

Introduction

The Barbados Oceanographic and Meteorological Experiment (BOMEX) Sea-Air Interaction Program, known as the Core Experiment, was conducted during May and June 1969 with the collaboration of seven Federal Agencies and the Government of Barbados. Ships, aircraft, satellites, and other platforms were used for the observations, with the objective of obtaining accurate measurements of the sea-air transfer of mass, energy, and momentum over an area representative of a single synoptic grid interval (Holland, 1970).

The BOMEX "cube" - 500 km x 500 km in horizontal dimensions, 500 mb deep in the atmosphere, and 500 m deep in the ocean - was located east of Barbados. Salinity-temperature-depth soundings (STD's) were taken four times a day at the two western fixed ships of the array, and eight times a day at the other three ships, to a depth of 1,000 m. Rawinsondes, consisting of separate sondes for temperature and humidity, were released 15 times daily at the four corner ships and the data recorded to at least 400 mb. Aircraft "line integral" missions were flown by one to six aircraft on a variable schedule.

In the design of the experiment, emphasis was given to the accurate measurement of the air-sea energy flux, the principal component being the latent heat of vaporization. Three independent estimates are to be compared:

(1) The heat loss from the ocean based on analysis of the oceanographic data.

(2) The terms of the water vapor continuity equation integrated over the atmospheric volume computed by means of the Gauss divergence theorem.

(3) The vertical flux of the water vapor as determined by correlation of high-frequency turbulent fluctuations of vertical velocity and humidity measured in the atmospheric surface layer, as well as budgets of heat, mechanical energy, and momentum (Rasmusson, 1971).

Within the 2 months devoted to the Core Experiment, observations were scheduled in three periods with 10-day breaks in between. The third period, June 20 - July 2, produced the most complete ship data and has been given first priority for analysis.

Almost all the data have been put through a first-pass reduction process with a highly satisfactory yield, both qualitatively and quantitatively. The products are now being analyzed, primarily to develop a final reduction process that will eliminate a larger fraction of the noise, retrieve an even larger portion of the recorded information content, and introduce more accurate calibrations and corrections. Some preliminary scientific results are also being derived.

Ocean Heat Budget

In the ocean heat budget studies, we have so far relied primarily on the fixed-ship STD data. These data were recorded by NASA's signal conditioning and recording device (SCARD), digitized at NASA's Mississippi Test Facility, reduced by Lt. Victor Delnore of the BOMAP Office using a procedure developed by John McHugh of the National Oceanographic Data Center, and analyzed by Lt. Delnore. Figure 1 shows the mean temperature profiles in the top 80 m for each of the fixed ships based on 10-day observations during the third BOMEX Observation Period. The *Rainier* and *Mt. Mitchell,* the westernmost ships, have the warmest surface water; the *Oceanographer* and *Discoverer,* the eastern ships, have the coolest. The overall spread is 0.7°C.

Direct measurements of the currents in the upper few meters are not available. Positions of the ships while drifting confirm the expectation that, on the average, the flow is toward the west, with a smaller northward component, at a velocity on the order of 1 kt. Advective temperature changes in the upper 20 m, averaged over the third period, would thus be expected to be of the order of -.03°C/day. Below this depth the east-west temperature gradient disappears rapidly. By 50 m the gradient is meridional, the coldest water lying beneath the two northernmost ships, the *Rainier* and *Oceanographer*. The average advective change would most likely become very small below 30 m, possibly changing sign.

In the upper 10 m of the mixed layer, during Period III, the average diurnal variation contains the major part of the time variation, with an amplitude of about ¼°C. During the 6 hours of warming, the rate of change is about 1°C/day. A fluctuation of longer period with an amplitude of about .2°C was associated with rates of the order of .03°C/day, comparable to the horizontal advection.

The overall linear trend was about +.01°C/day, which would reflect both incomplete sampling of the long-period fluctuation and any seasonal warming. The residual higher-frequency deviations are generally less than .1°C and include random errors of measurement from one STD cast to the next. The sampling error of the 10-day average for each observation time can thus be considered to be about .03°C.

The temperature profiles for the *Discoverer* STD casts showing the coldest and warmest mixed layer are presented in figure 2, together with the average profile for BOMEX Period III. The highly unstable thermal stratification between 15 and 31 m is compensated for by a very large increase of salinity with depth (not shown), giving a very stable density stratification below the mixed layer. The low-salinity surface layer was traced to the mouth of the Amazon River by scientists of the Research Triangle Institute aboard the Cape Fear Technical Institute's research vessel *Advance II*. At the *Discoverer*, the large salinity gradient puts a stable floor under the layer subject to diurnal thermal convection.

The average Period III temperature profile for each observation time for the *Discoverer* is shown in figure 3. The vertical resolution is 1 m. The existence of a layer from 25 to 28 m with an overall diurnal amplitude not exceeding .03°C again suggests that this is an upper limit of the random errors of measurement. The upper 17 m show a rapid heating of the upper few meters with slow vertical penetration of the heating, and a slower cooling rate with rapid vertical propagation. The stable stratification at the time of maximum surface temperature and the vertically uniform temperature at minimum are reminiscent of the seasonal variation of the temperature profile in a lake. The exquisite quality of the data is emphasized by the fact that the overall range in the upper 3 m is only .275°C.

When the average difference in heat content of the top 27 m from the previous observation time to the following one is divided by the 6-hour time interval, the curve of heat storage rate results, labelled Q_θ in figure 4. The abscissa is local time and the ordinate is in langleys per minute. Also shown is the net radiative heating, $Q_S - Q_A$, from the pyranometer mounted on the boom extending from the ship's bow, with a small infrared back-radiation correction. The difference, $Q_V + Q_K$, represents the net loss due to evaporation and sensible heat transfer to the atmosphere, when the net daily storage, advective change, and any heat flux through the 27 m level are neglected. The average loss, .37 ly/min, is then equal to the radiative input by definition. Measurements of the sensible heat flux in the atmospheric surface layer in this geographical area under similar meteorological conditions by various investigators (e.g., Garstang, 1967; Phelps, 1971; and Donelan, 1970) suggest that it is on the order of .02 ly/min. This would leave .35 ly/min for evaporation, which would then be about 8.4 mm/day.

In these units the very rough estimates of advection and long-term storage, given earlier, amount to about -.06 and +.02 ly/min, respectively. Both would reduce the estimated net loss to the atmosphere, leaving a total energy transfer from sea to air of about .29 ly/min, of which .27 ly/min would be available for evaporation. The corresponding evaporation rate would be about 6.5 mm/day.

Both the phase and the amplitude of the diurnal variation of sea-air energy transfer rate deduced from this simple one-dimensional heat budget model are suprising. For example, evaporation rates computed from the ship's boom meteorological data by the bulk aerodynamic method imply a smaller amplitude with an afternoon minimum. Further studies of the ocean heat and salt budgets are underway.
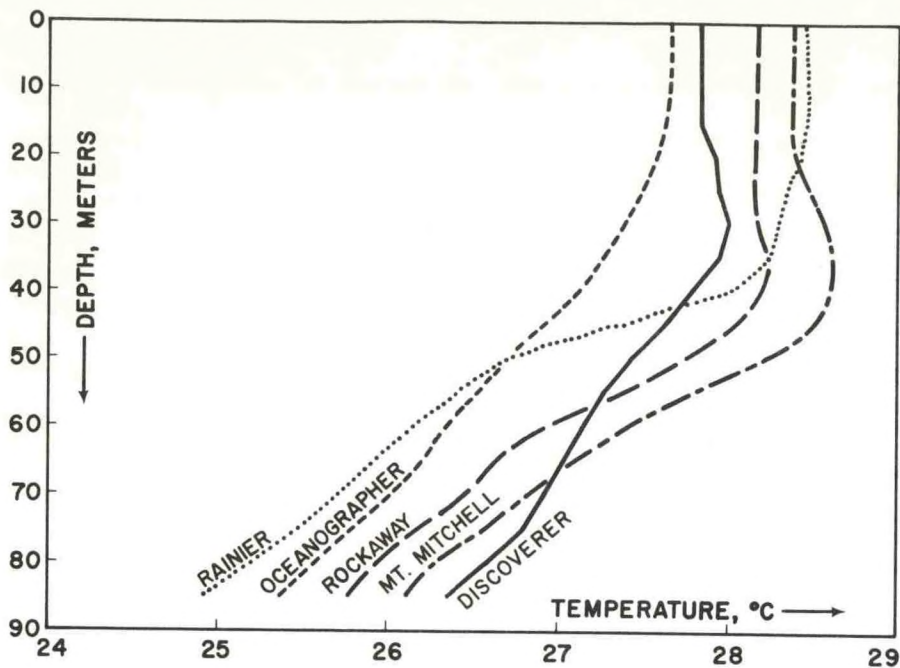
Figure 1. Ten-day mean temperature profiles (STD
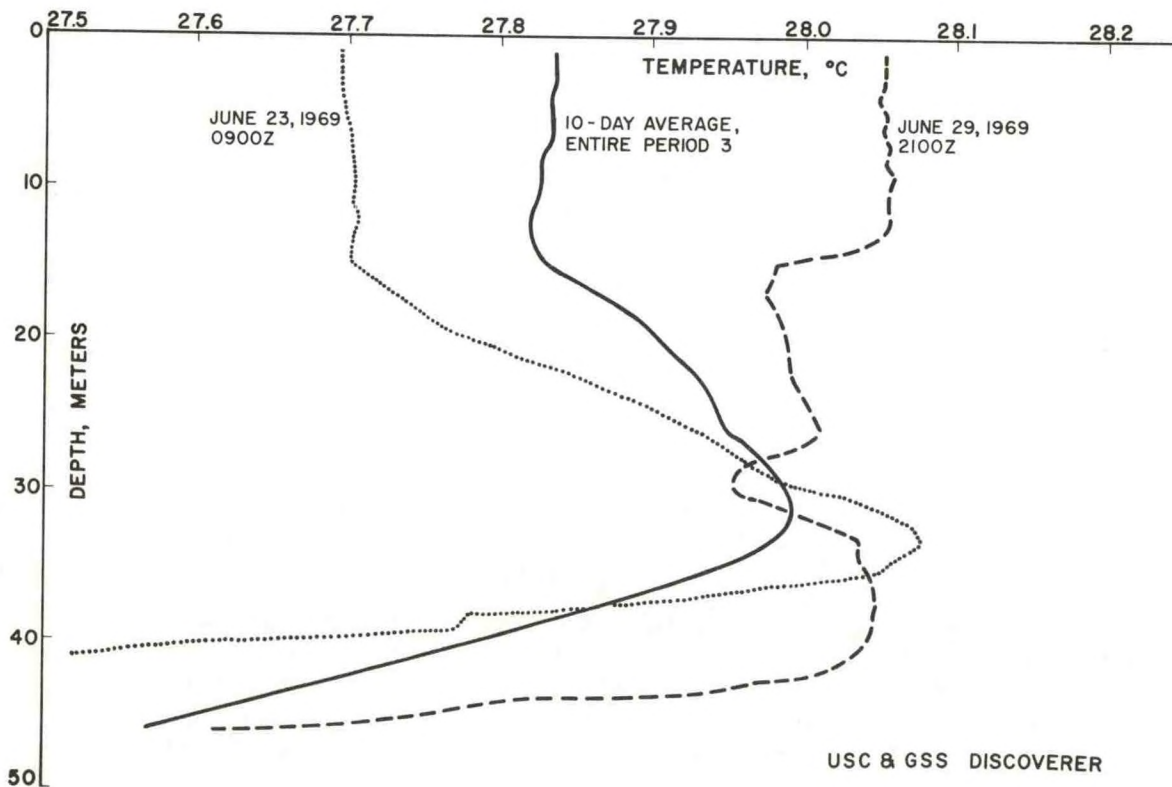data) in the top 80 m for each ship.

Figure 2. Temperature profiles for Discoverer STD casts showing coldest and
warmest mixed layer and the 10-day average profile during Period III.
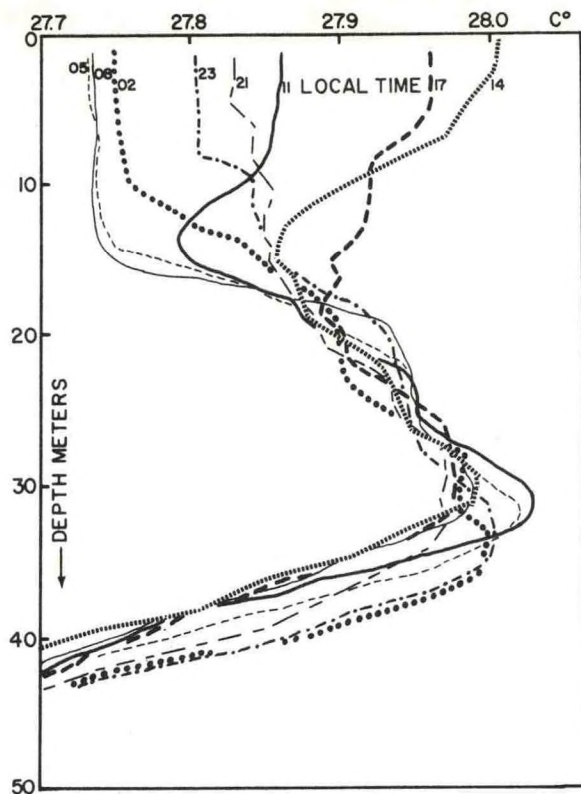
Figure 3. *Average Period III temperature profiles for each observation time at the Discoverer from STD casts.*
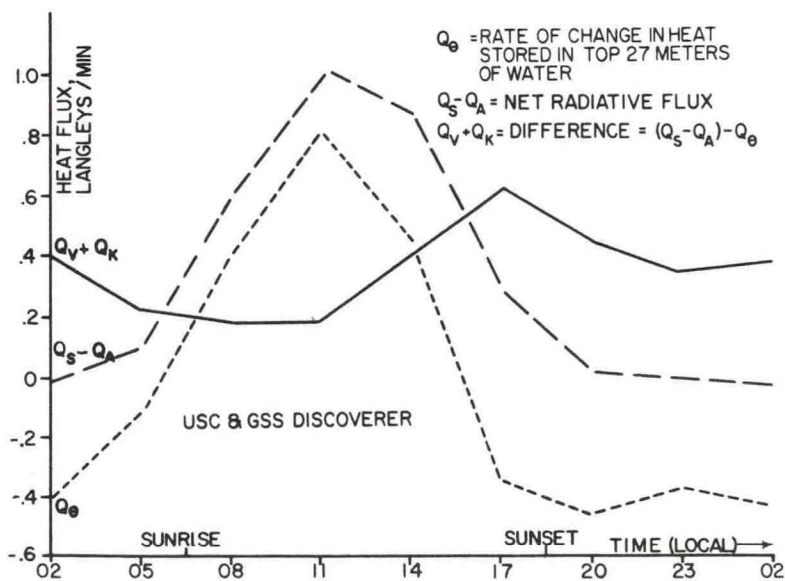

Figure 4. *Diurnal rate of heat flux (ly/min) at the Discoverer.*

As to the evidence from the numerous direct measurements made in BOMEX of vertical eddy flux of water vapor in the lowest tens of meters of the atmosphere, it should be noted that the bulk of these measurements were made during May, when the Navy's Floating Laboratory Instrument Platform (FLIP) was on station in the BOMEX array.

Three primary data sets will be summarized here. First, NOAA Research Flight Facility DC-6 aircraft collected 8 to 10 data samples of 5 min each, in each of six categories determined by two aircraft headings, along wind and crosswind, and three altitudes, 18, 45, and 150 m (Friedman et al., 1970). Vertical velocity was measured by an angle-of-attack vane installed and calibrated under the technical guidance of U.O. Lappe. Humidity was measured by a microwave refractometer installed and operated under the direction of Brad Bean of NOAA's Wave Propagation Laboratory. The data were reduced and spectrum computations performed by Leonard Rinaldi. Statistical summaries of the cospectral densities of vertical velocity and absolute humidity were prepared by Dr. Bean's group.

Second, a similar data set was collected by the Queen Air aircraft of the National Center for Atmospheric Research with a sonic anemometer and Lyman-alpha humidiometer installed and operated under the direction of Mikio Miyake of the University of British Columbia (UBC) (Miyake et al., 1970). A selection of 17 Queen Air data runs has been analyzed by Mark Donelan of UBC (Donelan, 1970).

Third, on FLIP, a set of fast-response vertical velocity measurements was made under the direction of R.W. Stewart of UBC, by means of a sonic anemometer, and a coordinated set of humidity measurements by Stephen Pond of Oregon State University (OSU) using a Lyman-alpha humidiometer. One subset consisting of 5 runs ranging in length from 35 to 52 min each has been analyzed by Gordan A. McBean of UBC (McBean, 1970). A different subset of 11 runs ranging in length from 25 to 87 min has been analyzed by George T. Phelps of OSU (Phelps, 1971).

Figure 5 shows the RFF cospectral densities of vertical velocity, w, and specific humidity, q, at 45 m, normalized by dividing the covariance of w and q, and nondimensionalized by multiplication by wave number k. The averages of 10 downwind runs (solid) and 10 crosswind runs (dashed) at 45 m, with the band representing cospectral densities within one standard deviation of the mean, are shown by hand-smoothed curves based on averages and standard deviations at 11 abscissa values supplied by Dr. Bean. At a nominal airspeed of 100 m/sec, the frequency band from .05 to 4 kHz is converted to wave number band from .0005 to .04 m^{-1}. The upper cutoff is determined by combined analog filtering and digital filtering of the data to avoid noise due to instrument boom vibration. The lower cutoff is determined by the limits of adequate statistical sampling and low-frequency instrumental resolution. The cospectrum represents the distribution of vertical eddy flux of water vapor with respect to the logarithm of wave number.
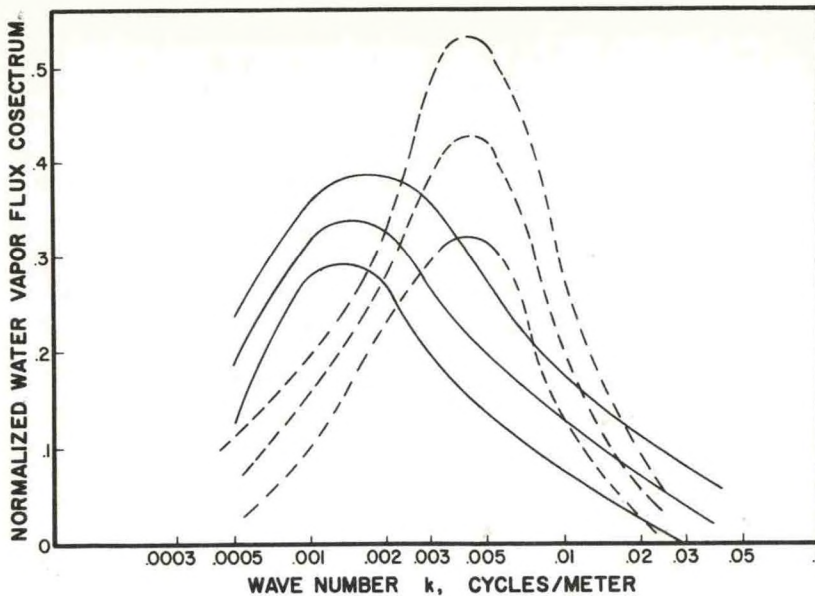
WAVE NUMBER k, CYCLES/METER

Figure 5. *Normalized water vapor flux cospectrum; $k\phi_{wq}(k)/\overline{w'q'}$ as a function of wave number k from RFF along-wind (solid) and crosswind (dashed) samples at 45-m altitude. Each family of three curves represents the mean and ± 1 standard deviation of 10 samples (hand-smoothed).*

The crosswind cospectrum has a sharp peak at a wave number of about .004 m^{-1}, or a wavelength of about 250 m. In the along-wind direction the cospectrum has a flatter peak at a wavelength of about 700 m. The eddies dominating the vertical transport of water vapor are thus seen to be highly elongated in the direction of the mean wind. It seems likely that a broader bandwidth would be required to obtain accurate values of the integrated covariance, and that the vertical flux may be underestimated because of the high-frequency cutoff in the crosswind case, and the low-frequency cutoff in the along-wind case.

Similar plots of the cospectra at 18 m and 150 m show an increase in the wavelength of the cospectral peak from about 200 m at a height of 18 m to about 600 m at 150 m. While the eddy wavelength of maximum flux appears to be within the instrumental bandwidth at all three levels, the possibility of significant loss in the integrated flux, at high frequencies at the lowest altitude, and at low frequencies at the highest altitude, must be given serious consideration.

The Queen Air data (Donelan, 1970) show a peak in the cospectrum at a somewhat shorter wavelength than that indicated by the RFF data, and a slower decrease of the cospectrum, cutting off at a wave number about an order of magnitude higher than the RFF cutoff. The FLIP data (McBean, 1970; Phelps, 1971) agree with the Queen Air data at the high-frequency end. At the lower wave numbers, on the other hand, including that of the cospectral peak, the RFF data appear to define the cospectrum better. The FLIP cospectral densities have a very wide scatter at wavelengths of the order of 100 m or more (wave numbers $\leq$ .01 m^{-1}), falling predominantly below those derived from the RFF data.

Thus all the wq covariance values may be suspected of being underestimates of the flux that would be observed with a system having sufficient bandwidth (wavelengths from 1 to at least 10,000 m). The amount of the underestimate cannot be accurately determined from the available data and may be variable. Nevertheless, it appears that, for the first time, a rather good picture of the cospectrum, as well as the individual spectra of w and q, and their variations with direction relative to the wind and with altitude in the lowest few hundred meters, can be synthesized from the data obtained with the various measurement systems.

The measured fluxes from all three observation platforms are plotted as evaporation rates against local time in figure 6. The Queen Air data excluded, the bulk of the data lie between 3 and 7 mm/day. The Queen Air data (NCAR/UBC) fall below most of the other data.
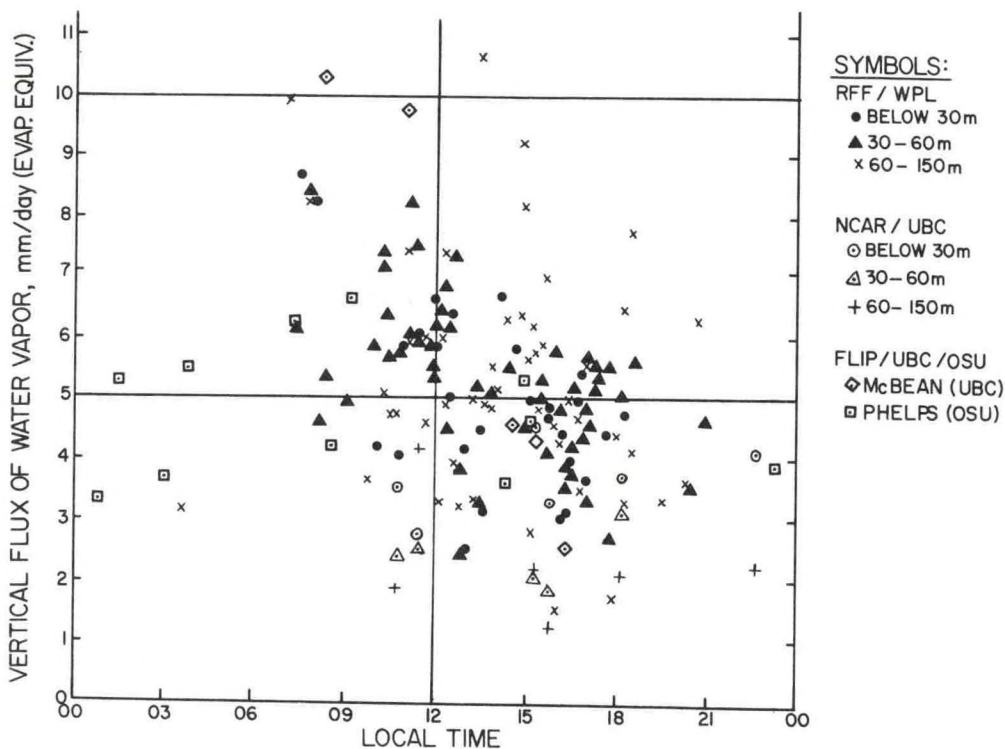
Figure 6. Measurements of vertical flux of water vapor, mm/day (evporation equivalent), based on RFF and NCAR aircraft and FLIP data vs. time of day.

The results of the ocean heat budget analysis based on the *Discoverer* data for June 21 - July 2, discussed previously, do not necessarily apply to the May data obtained in the vicinity of FLIP. It is interesting, however, that the median value of the May FLIP and RFF fluxes (about 5 mm/day) would be consistent with the mean value estimated from the late June ocean budget from the *Discoverer* data (6.5 mm/day), if the former were assumed to be 23 percent lower due to bandwidth truncation.

Divergence Error Studies

To obtain estimates of the evaporation by measuring all the other terms of the atmospheric volume budget of water vapor, it is essential to determine accurately the horizontal velocity divergence (Holland, 1970).

For measuring the area-integrated divergence by integration of the outward normal velocity component around the boundary by means of the divergence theorem, the line integral flight patterns were designed to provide dense sampling of the normal wind component around the perimeter of the BOMEX square. Efforts were made to minimize errors due to time delays between measurements on opposite sides by using at least two aircraft. This required that extensive comparison data be obtained between the aircraft whose measurements were to be combined.

Figure 7 shows part of the flight pattern used by four aircraft to obtain data simultaneously on all four sides of the BOMEX square at each of three altitudes. Two aircraft were flown together in loose formation from Barbados to point KILO, the midpoint of the south side of the square. They then separated, and each flew a series of data legs at altitudes of 300, 1,300, 2,300, and again 300 m, one on the DELTA-ALFA leg and the other on the ECHO-BRAVO leg. They then rejoined at KILO and flew back to Barbados together for intercomparison. The whole mission took approximately 12 hours. The starting times of the outbound and inbound intercomparison legs were separated by about 10 hours. The first (outbound) and second (inbound) 300-m data legs were separated by about 6 hours.
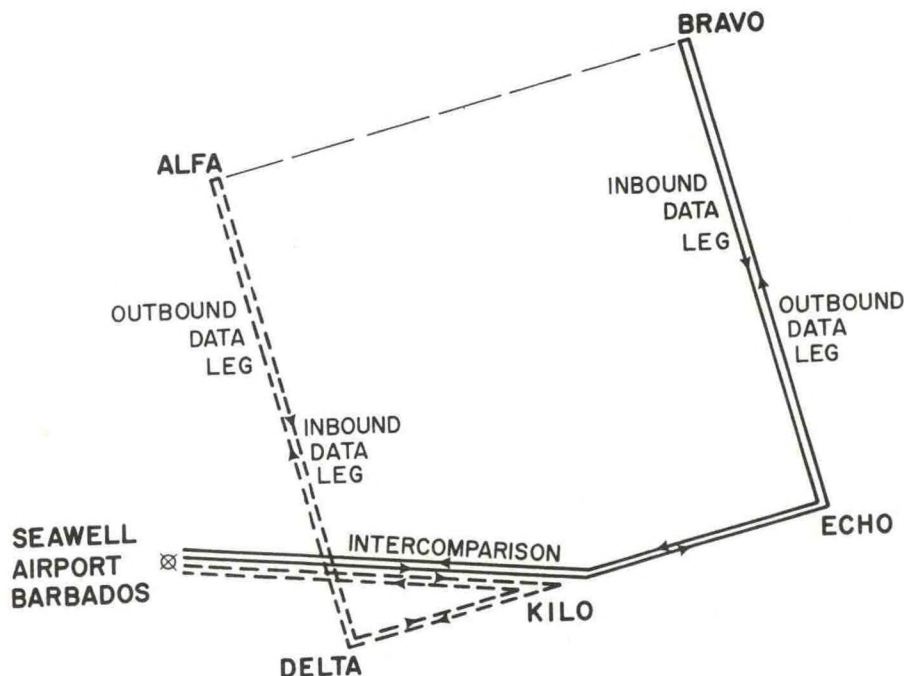

Figure 7. Part of four-aircraft flight pattern used in divergence test.

39

Both the RFF and the Navy VW-4 squadron took part in these line integral missions, but the data discussed are only RFF wind data based on digital recordings of Doppler drift angle and ground speed, magnetic heading, pitot tube pressure differential, temperature, and humidity. These data were reduced by the National Hurricane Research Laboratory, NOAA. The computations summarized here were carried out by P. Pytlowany of BOMAP.

The difference between the normal wind components measured by two aircraft on the intercomparison legs provides an estimate of the errors in divergence that would occur when the (oppositely directed) normal components measured by the same two aircraft of opposite data legs are added. In 12 such intercomparisons between pairs of RFF aircraft, a mean difference of 0.13 m/sec was obtained, corresponding to a systematic error of 0.26×10^{-6} sec^{-1} in the divergence averaged over the 500-km box. It is assumed that this small systematic error can be corrected. The random error, computed from the standard deviation of the difference in normal velocity, turned out to be 2.1×10^{-6} sec^{-1}.

The comparison of normal wind components measured by the same aircraft on the outbound and inbound passes on the same leg permit an estimate of the divergence errors that would result from measurements of normal wind component made by the same aircraft on both sides of the square by flying around the square over a period of several hours. In 21 outbound-inbound pairs of intercomparison legs (10 hours time delay), the random error in the divergence, based on the standard deviation of the difference in normal velocity components, was 3.5×10^{-6} sec^{-1}. In 9 outbound-inbound pairs of 300-m data legs (6 hours time delay), the random error was 2.2×10^{-6} sec^{-1}. Thus the error increases with time delay and is larger than that attributable to the difference between two aircraft flying simultaneously. It follows that this type of error is mainly due to time changes in the wind.

The general divergence theorem method will be called the "boundary method." Another method has suggested itself, since the same flights provided the necessary data for it. Called the "trend method," it consists of measuring the one-dimensional divergence in each of two orthogonal directions by a least-squares estimate of the rate of change of the parallel wind component along a straight, level track.

In the boundary method, the difference between two averages of the same wind component is used. The trend method involves, in effect, reversing the order of averaging and differencing. The potential advantages of the latter are that average time delays are kept to half the duration of one data leg. Absolute accuracy of Doppler drift angle and ground speed are not needed since the heading is not changed during the differencing process. Only the stability of calibration of one aircraft over the short differencing interval is involved.

The intercomparison flight **leg** data are the only ones from which a direct estimate of the error of the trend method can be made. The random error in divergence for 12 intercomparisons is 2.5×10^{-6} sec^{-1} for a single one-dimensional measurement. The accuracy is thus comparable to the accuracy of the two-dimensional divergence determined by the boundary method, based on data from four aircraft flying simultaneously or from one aircraft on the perimeter circuit.

Figure 8 shows a comparison of the two-dimensional divergence measured by aircraft and by ship rawinsondes. This example is for a daytime aircraft mission on June 22, 1969. The continuous curves are based on divergence computations from the rawinsondes in fifty 10-mb layers. The vertical coordinate is p*, which is equal to the difference between sea level pressure and actual pressure at each altitude. The rawinsonde data were recorded by NASA on SCARD, were digitized and reduced by NASA at the Mississippi Test Facility, and have been time smoothed and interpolated to uniform intervals by Thomas Carpenter of the Air Resources Laboratory, NOAA. Each curve consists of the averages of the divergences at two successive observation times (e.g., the 1200-1400 GMT curve is based on the time-smoothed 1200 GMT and 1330 GMT rawinsonde data). No corrections have been made for ship motion, although the time-averaging probably reduces the maximum errors due to this motion to something of the order of 1×10^{-6} sec^{-1}.

The rawinsondes show the lowest 50 mb (about 400 m), representing the subcloud layer, undergoing a change from convergence to divergence during the course of the day. This portion, based on the first 2 min of data, is subject to considerable uncertainty. The cumulus layer extending up to just over 100 mb is rather steadily divergent throughout this period. From the trade inversion, in the neighborhood of 150 mb and on up, the pattern is quite variable with respect to both height and time.

The aircraft divergences at 300, 1,300, and 2,300 m were computed from the data obtained by only two aircraft, flying the eastern and western sides of the square. The boundary method was used for the east-west component of the divergence and the trend method for the north-south component ("mixed" method). Computations were made for both the outbound and inbound passes at 300 m. Data at 3,300 and 4,900 m were obtained by one aircraft making the complete circuit, first at the lower level clockwise, then at the upper counterclockwise. With measurements on all four sides it was possible to derive the total divergence independently by both the boundary and trend methods at these two higher levels.

Agreement between the divergence computed from aircraft and rawinsonde data is as good as can be expected in view of the rapid time changes and great difference in the time-space sampling characteristics of the two systems. The discrepancy at 300 m could be partly caused by errors in the rawinsonde data in the first 2 min after launch. At 3,300 m the two methods give considerably different results, but both are within the range of divergences computed from the rawinsonde data collected during the time of the aircraft circuit. The trend method comes closest to representing a time-mean of the rawinsonde data. At 4,900 m the two aircraft methods are in better agreement with each other, but differ from the rawinsonde divergences measured at the same level. At a few hundred meters lower altitude, however, some rawinsonde data agree closely with the aircraft data in showing pronounced convergence during the observation period.
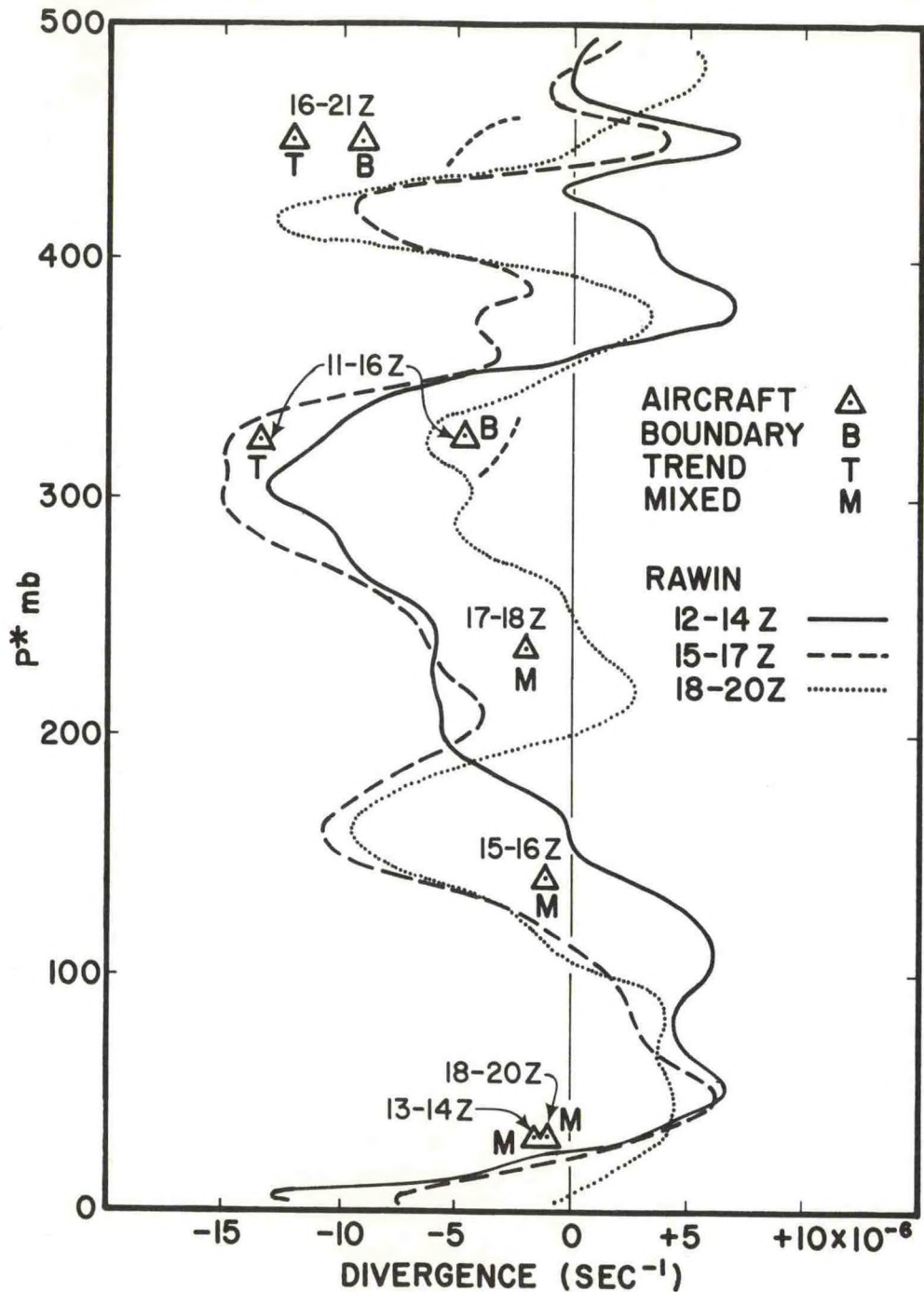
Figure 8. Comparison of aircraft and rawinsonde measurements of two-dimensional mass divergence. Aircraft measurements by boundary (B), trend (T), and mixed (M) methods.

The conclusion can be drawn that the trend method is a promising substitute for the boundary method in computing divergence and will permit roughly a doubling of the BOMEX aircraft data base for divergence estimates, and may permit aircraft divergence measurements in future experiments with fewer flight hours. The accuracy considerations are approximately the same for vorticity measurements, where the trend of the normal component along one leg would replace the difference between the mean parallel components along opposite legs.

Applications of the divergence measurements to the water vapor budget analysis, leading to further evidence regarding the evaporation rate, will be discussed in Dr. Rasmusson's paper, which follows.

References

Donelan, M., "An Airborne Investigation of the Structure of the Atmospheric Boundary Layer over the Tropical Ocean," Ph.D. Thesis, University of British Columbia, 1970.

Friedman, H.A., Conrad, G., and McFadden, J.D., "ESSA Research Flight Facility Aircraft Participation in the Barbados Oceanographic and Meteorological Experiment," Bulletin of the American Meteorological Society, Vol. 51, 1970, pp. 822-834.

Garstang, M., "Sensible and Latent Heat Exchange in Low Latitude Synoptic-Scale Systems," Tellus, Vol. 19, 1967, pp. 492-508.

Holland, J.Z., "Preliminary Report on the BOMEX Sea-Air Interaction Program," Bulletin of the American Meteorological Society, Vol. 51, 1970, pp. 809-820.

McBean, G.A., "The Turbulent Transfer Mechanisms in the Atmospheric Surface Layer," Ph.D. Thesis, Institute of Oceanography, University of British Columbia, 1970.

Miyake, M., Donelan, M., and Mitsuta, Y., "Airborne Measurement of Turbulent Fluxes," Journal of Geophysical Research, Vol. 75, 1970, pp. 4506-4518.

Phelps, G.T., "The Fluxes of Latent and Sensible Heat in the Marine Boundary Layer," Ph.D. Thesis, Department of Oceanography, Oregon State University, 1971.

Rasmusson, Eugene M., "Mass, Momentum, and Energy Budget Equations for BOMAP Computations," NOAA Technical Memorandum ERL BOMAP-3, January 1971.

BOMEX Atmospheric Mass and Energy Budgets
Preliminary Results

Eugene M. Rasmusson
BOMAP Office

The Barbados Oceanographic and Meteorological Analysis Project (BOMAP) has as one of its major responsibilities the analyses of the mass, momentum, and energy budgets (including latent heat) of the atmospheric mass within the BOMEX box. Although most of the data currently available for such analyses represent output from intermediate processing steps, rather than final validated data, the decision has been made to run a series of trial integral computations based on the data in their present form.

The first major trial analyses were made for a 5-day undisturbed period in late June, 1969. A vertical resolution of 10 mb was used in computations from the surface to 500 mb above the surface in a p* coordinate system, where p* is the position on the vertical axis in terms of pressure differential relative to sea level (Rasmusson, 1971). Rawinsonde observations at intervals of $1\frac{1}{2}$ hours constituted the basic data.

Prior to these calculations, the basic data at each level were examined by my colleague, Mr. Carpenter, and any values more than three standard deviations from the mean at that level were discarded. Next, missing values were filled in by fitting a cubic spline to the data points at each level. Finally, the data at each level were filtered to remove all frequencies of less than 6-hour periods. Frequencies of 12-hour periods or greater were passed unattenuated.

The handling of the humidity data is still a serious special problem because of instrumental errors. These errors, which will be discussed in the paper by Crutcher, Sanders and Sullivan, induce a spurious diurnal variation in the humidity values. In an effort to minimize their effect, the diurnal variation of humidity in the basic data was removed. No direct account was taken of the effect of ship motion on the measured wind, although the filtering procedure used probably removed much of this error. Subsequent to the basic computations, however, the mean 5-day ship motions during the periods of rawinsonde ascent were computed. The errors arising from the neglect of this correction , which are small, but not negligible, will be pointed out in a later discussion.

Our evaluation of the results to date is limited to an examination of the mass and water vapor budgets. Before reviewing a few highlights from these results, I wish to point out a few features of the potential temperature time cross section shown in figure 1 for the *Oceanographer* (northeast corner of BOMEX array) for the 5-day period. The zone of stability associated with the trade inversion is found between the $\theta = 302°-308°$ isentropes, and centers approximately on the 305° isentrope (shown as a heavier line). In examining the budget results, we have been particularly interested in noting relationships between this stable layer and features of the computed divergence and vertical motion profiles. Significant changes began taking place in the thermal structure around the middle of the period in connection with an upper tropospheric trough passage, although little rainfall was observed.

The trade inversion weakened markedly, and a descending stable layer appeared aloft, which, by the end of the period, appeared to be merging into, or forming, a new trade inversion. These thermal changes were also accompanied by sharp changes in humidity in the vicinity of the stable layers.

Turning to the water vapor budget calculations, we show here the computed 5-day average water balance components for this period:

<div align="center">

COMPUTED WATER BUDGET

03 GMT 22 June - 21 GMT 26 June
1969

Units: millimeters/day

</div>

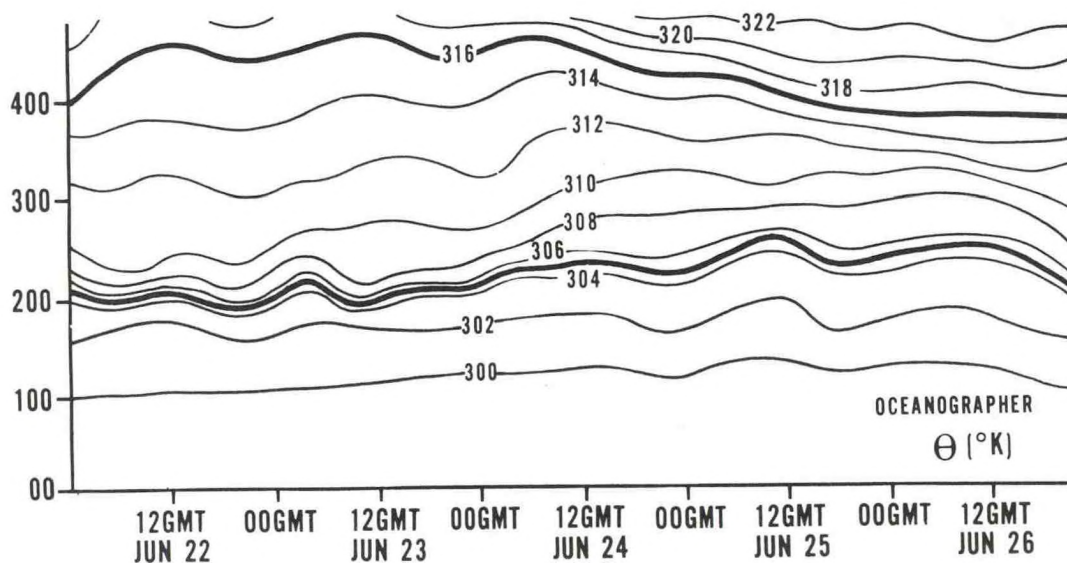| Precipitation | | | + 0.2 |
Change of Vapor Content	$\frac{\delta}{\delta t} \int \overline{q} dp^*$	=	+ 0.6
Mean Flux Divergence	$\int [q][V_n] dp^*$	=	+ 6.5
Advective Flux Divergence	$\int [q^* V_n^*] dp^*$	=	+ 1.1
Outflow Through the Top	$(\overline{q} \ \overline{\omega^*})_{top}$	=	$\underline{- 1.1}$
Residual (Evaporation)		=	+ 7.3

Figure 1. Potential temperature time cross sections for the Oceanographer.

As we see, the components consist of the following:

(1) Precipitation. Very little precipitation fell over the array during this period. From an analysis of radar and satellite data, Dr. Hudlow of our office has arrived at an average value of only .2 mm per day.

(2) $\delta q/\delta t$, the mean change in the water vapor content of the atmosphereic column, where q - specific humidity. The term is small during this period.

(3) Horizontal vapor flux divergence. In the formulation of the vapor balance equation used in the BOMAP computations (Rasmusson, 1971), the vapor flux divergence was partitioned into two terms:

    (a) A term that approximates the $q\nabla \cdot V$ term in the basic expression for divergence. This will be referred to as the mean divergence contribution. The dominance of this term is apparent, emphasizing the importance of an accurate evaluation of the velocity divergence.

    (b) A term that corresponds approximately to the $V \cdot \nabla q$ term in the basic expression for divergence. This will be referred to as the advective contribution to the divergence.

(4) Vertical vapor flux through the top of the box. During undisturbed periods, the vertical flux at $p^* = 500$ mb arising from variations in q and ω^* on scales smaller than the dimensions of the box is neglected. Thus the flux is evaluated as the product of the mean values of ω^* (in units of 10^{-4} mb/sec^{-1}) and q at the top of the box. It is interesting to note that through the continuity equation, this term plus the mean divergence contribution equals the vertical advection. Comparing this with the horizontal advective contribution shows that downward transport of dry air was five times more effective in drying out the column than was the horizontal advection of dry air.

(5) The sum of the above terms, which equals the computed evaporation. Application of a correction for mean ship motion reduces this value from 7.3 to 6.7 mm/day.

The dominance of the mean divergence term in the water budget computations and the importance of an accurate value of ω^* at the top of the box emphasize the importance of the kinematic mass budget computations. The kinematically computed mean divergence and vertical motion profiles are illustrated in figure 2. Note that in the p^* system, upward motion is positive. The level of maximum divergence is near $p^* = 80$ mb, the level at which the mean sounding begins to show an increase in stability. The level of zero divergence at $p^* = 160$ mb, which marks the level of computed maximum mean downward motion, is slightly below the level of greatest stability, marked by the 305° isentrope. The values of divergence, averaged for three aircraft line integral missions, are shown by crosses on the profile. A mean vertical velocity has also been computed for the top 50 mb
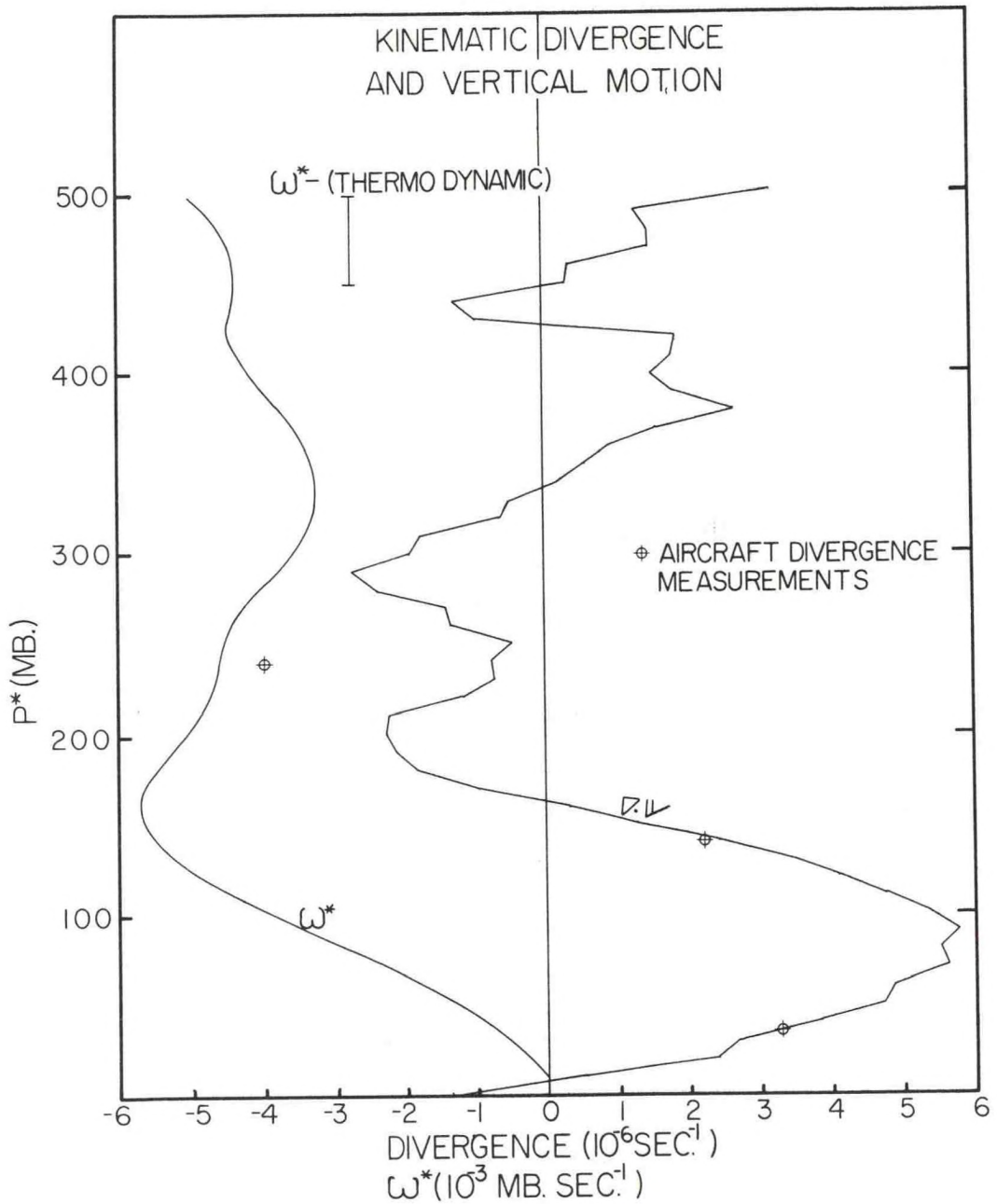
Figure 2. *Kinematically computed mean divergence*
and vertical motion profiles.

of the box from the thermodynamic equation. Values of radiational cooling were required for this computation, and these were kindly provided by Dr. Stephen Cox of Colorado State University.

In terms of mean divergence of the column, the thermodynamic divergence averages about 5×10^{-7} sec^{-1} less than the kinematic divergence, which represents good agreement between the two methods. This difference is reduced even further, to around 3×10^{-7} sec^{-1}, when a correction is applied for the mean ship motion.

Examination of the divergence time cross section showed that low-level divergence prevailed during almost the entire 5-day period, although the intensity varied considerably. This strong divergence was typically capped by a region of convergence, as shown on the mean profile, although here the time variability was much greater. The divergence computed for the upper half of the box was extremely variable, but a significant portion of this variability represented a computed diurnal variation in divergence and vertical motion.

The computed diurnal variation of vertical motion is shown in figure 3, where ω^* is in units of 10^{-4}mb sec^{-1}. A semidiurnal variation of ω^* was computed in the lowest 80 to 100 mb. Above p* = 100 mb, a diurnal variation dominates the pattern. In the upper 250 mb of the box, the data show relative sinking motion at night, relative rising motion during most of the daylight hours. The maximum diurnal changes at the top of the box represent a computed vertical displacement of $\pm$ 38 mb around the mean sinking rate. One might expect to find visible evidence of these variations in the cumulus layer (p* = 50-150 mb) in the form of a diurnal variation in cloudiness.
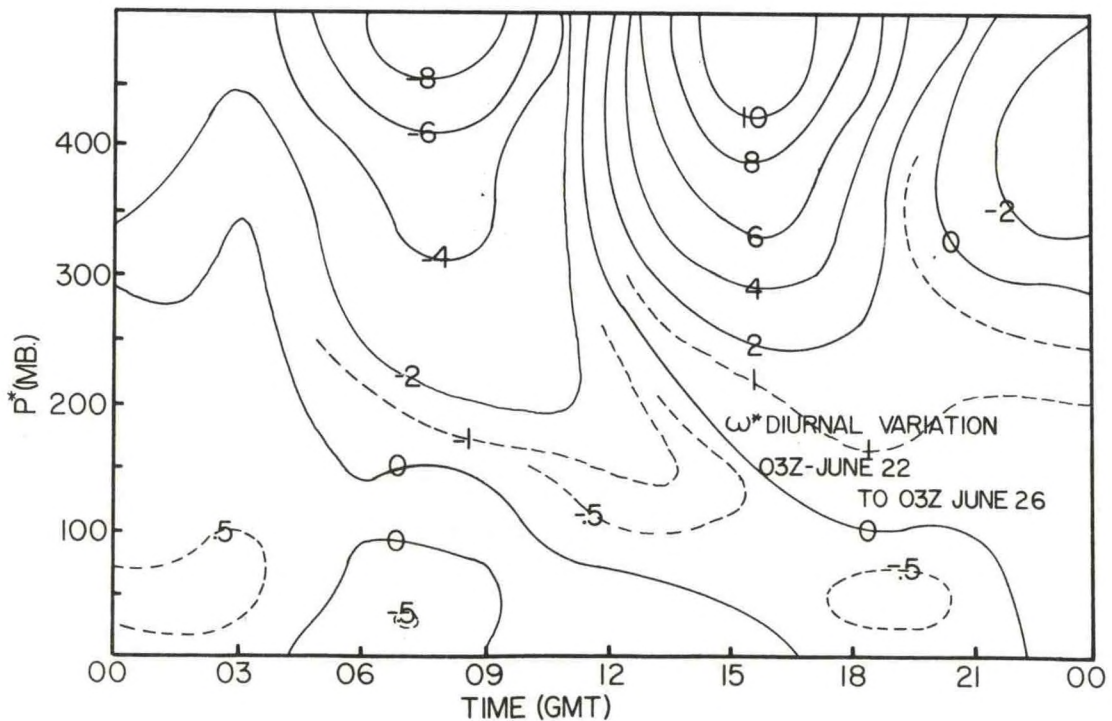
Figure 3. Computed diurnal variation of vertical motion, ω^*, in 10^{-4} mb sec^{-1}.

48

Here, the computations give on balance a weak tendency for downward motion during the day, upward motion at night, in apparent agreement with observed diurnal changes of radar echoes during this period.

For a more detailed look at the vapor flux divergence, we turn next to figure 4, which shows the relative contribution of the mean term (small squares) and the advective term (small triangles) as functions of p*. The

VAPOR FLUX DIVERGENCE

Figure 4. *Relative contribution of mean term (small squares) and advective term (small triangles) to the vertical flux divergence as a function of p*.*

Figure 5. *Computed vertical moisture transport. Mean vertical motion (···), subgrid-scale eddies (——), and computed net vertical flux (---).*

relative importance of the mean divergence contribution was noted earlier. This figure shows that almost all the mean divergence contribution came f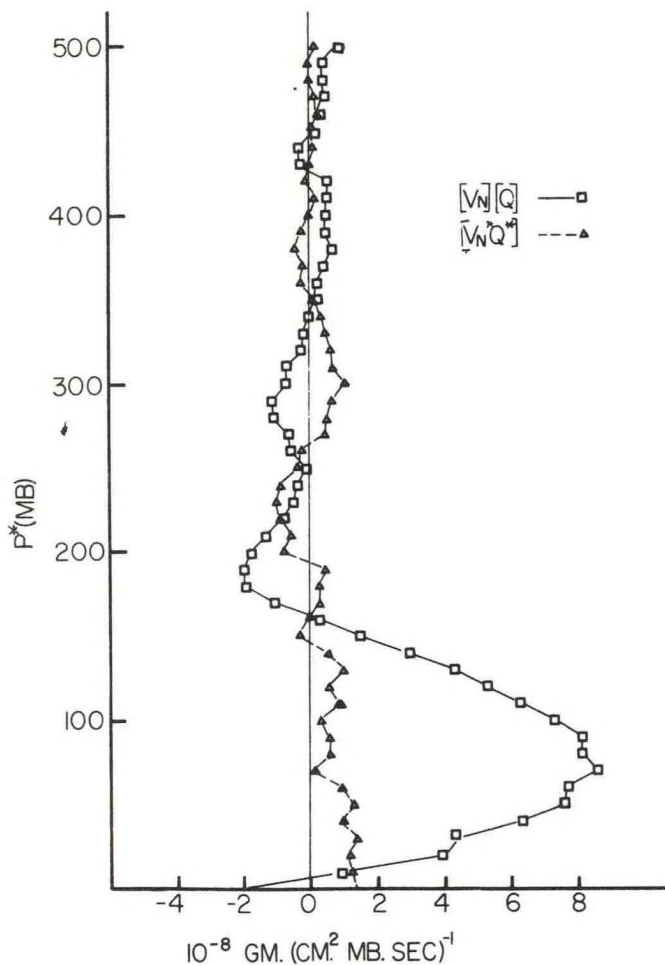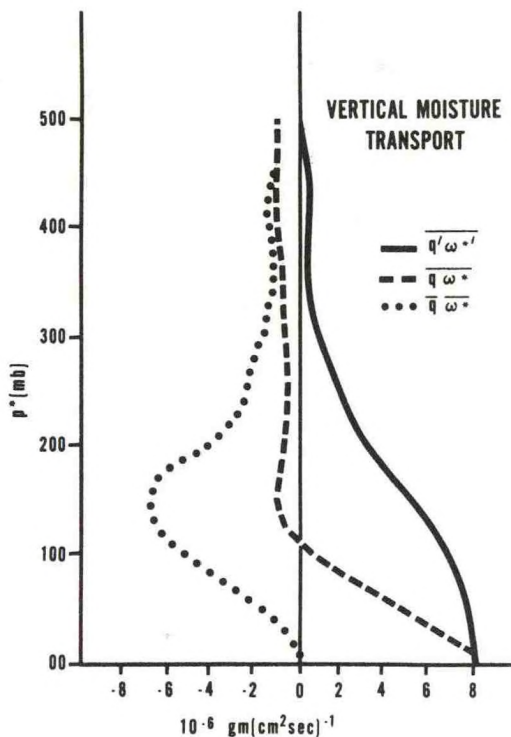rom the lowest 150 mb of the column, a consequence of the high values of velocity divergence weighted by the high values of humidity in the moist layer.

Since precipitation was practically negligible during the 5 days under study, this period offers an opportunity for an indirect computation of the vertical eddy flux of water vapor arising from correlations between q and ω^* for scales less than the size of the box, i.e., subgrid-scale vertical transfer, where the grid spacing is 500 km. In order to do this, we neglect condensation and assume that the vertical eddy flux = 0 at the top of the box.

The divergence of vertical eddy flux then equals the sum of the change in water vapor content, the horizontal flux convergence, and the convergence of water vapor due to the area-averaged vertical velocity. Beginning with zero at the top of the box, we can construct the eddy flux profile downward by adding the computed vertical eddy flux convergence of each layer to the value of the flux at the top of that layer. The computed vertical flux by the mean vertical motion, and the eddies, are shown in figure 5, together with the computed net vertical flux, which is the sum of the two terms.

The major features of the computed vertical eddy flux profile appear quite plausible. The eddy flux decreases slowly with height through the first 80 mb, then more rapidly as we proceed upward into the stable layer. The most rapid decrease in eddy flux, and consequently the largest values of vertical eddy flux convergence, is found in the layer $p^* = 170\text{-}220$ mb, which corresponds to the layer of greatest stability on the mean sounding. At the top of the mean stable layer ($p^* = 240$ mb), the computed eddy flux is less than 25 percent of its surface value. The consistently low values in the upper 150 mb of the box support the assumption of negligible eddy flux at the top.

The net vertical flux is upward in the lowest 110 mb, where the upward eddy flux is dominant. Above this level, the flux accomplished by the mean downward motion dominates, and the computed vertical flux settles down to a relatively steady value of around 10^{-6} gm^{-2} sec^{-1}.

The results presented here represent conditions during a single 5-day undisturbed period. Analysis of data taken during other intensive observational periods of BOMEX should clarify to what extent these results can be considered typical of undisturbed conditions in this geographical area.

Reference

Rasmusson, Eugene M., "Mass, Momentum, and Energy Budget Equations for BOMAP Computations," NOAA Technical Memorandum ERL BOMAP-3, January 1971.

Three-Dimensional Model of Precipitation Echoes for
X-Band Radar Data Collected During BOMEX

Michael D. Hudlow
BOMAP Office

Introduction

To perform meaningful budget studies, a knowledge of the statistical character and quantity of clouds and precipitation within the BOMEX box is required. During the experiment, surface-based and airborne radars were deployed to document precipitation echoes (fig. 1). A U.S. Army radar (AN/MPS-34) was stationed on the island of Barbados. A NOAA radar (METEOR-200) was aboard the NOAA ship *Discoverer*. Also, U.S. Air Force aircraft and aircraft from NOAA's Research Flight Facility were used to collect radar photographs. As a result, BOMEX yielded a considerable amount of radar data, but insufficient spatial and/or temporal coverage preclude precipitation calculations for the complete space-time domain directly from "gain-step" data.

The principal purpose of this study is to derive a quantitative statistical model that describes the three-dimensional geometry and intensity of a radar echo, given a one-dimensional parameter of the echo to serve as the independent estimator. As shown later in this report, the maximum dimension of a radar echo, recorded at a 0° tilt angle, constitutes a significant estimator of other echo parameters. Kessler (1965) has recognized the importance of radar echo statistics for parameterizing the morphology of mesoscale precipitation and specifically stresses echo length as one important statistic. For BOMAP, a computer algorithm has been designed that scans digitized radar data and estimates the maximum dimension of each radar echo contained in the digital array.

The statistical echo model provides a method for deriving precipitation estimates for the BOMEX box for those areas and times not documented by "gain-step" data. Figure 1 illustrates that only about 50 percent of the BOMEX square is covered by the surface-based radars when operating at a maximum surveillance range of 200 mi.[1] Aircraft radar data are generally available only during midday. Specifically, the echo model is useful in view of the following:

(1) Meaningful "gain-step" measurements are unlikely for ranges exceeding about 125 mi (see Hudlow, 1970). However, the length measurements are not as seriously degraded at ranges beyond 100 mi. This statement can be supported from examination of the mean profiles of echo area versus height (fig. 2). The mean profiles illustrate that echo area, and thus echo length, remain essentially constant with altitude for a distance above echo base. For example, the profiles imply that reasonable echo length measurements can be made at beam altitudes up to about 12,000 ft for echo areas greater than 60 sq. mi. Therefore, it is assumed that the echo model can be applied in extending the usable ranges for statistical estimates of precipitation rates via radar.

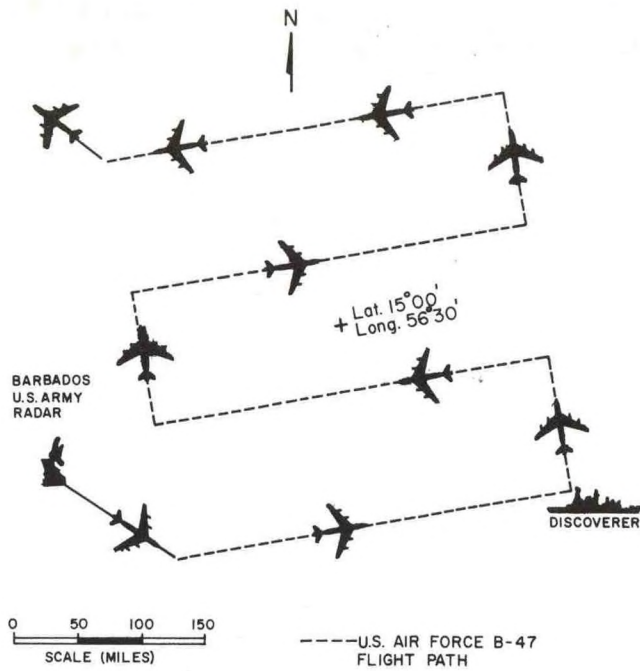[1]Statute miles are used throughout this report.

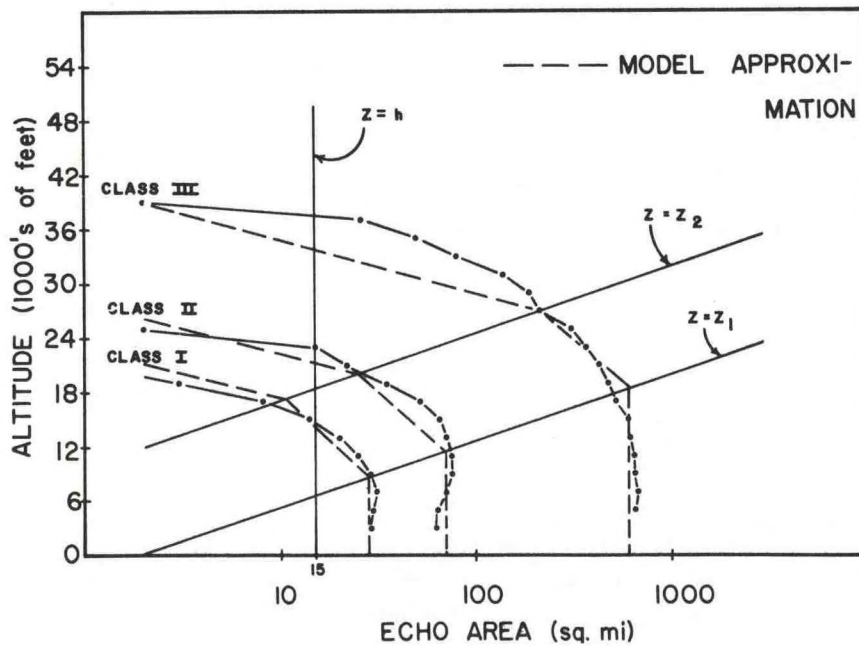*Figure 1. Surface-based and aircraft radar coverage during BOMEX.*

Figure 2. Average profiles depicting echo area vs. altitude above sea surface for three classes of echo sizes.

52

(2)   The echo model can be applied when only maximum gain data
      (no "gain stepping") are available.

(3)   The northern 50 percent of the BOMEX experimental area was
      not covered by surface-based radar sensors. For this area,
      the planned approach is to develop techniques for using
      satellite infrared data for assessing probable distributions
      of radar echo lengths. Given a distribution of echo lengths,
      the echo model can be used for making quantitative precipi-
      tation estimates. This subject is discussed by Mr. Scherer
      in his paper.

For storms observed in central Florida, Byers (1948) showed a signifi-
cant correlation between the volume of water deposited over a network of rain
gages and the time-averaged volume of radar echoes existing above the net-
work. More recently, Rogers and Rao (1968), Holtz (1968), and Altman (1970)
have presented quantitative echo models based on geometric and similarity
considerations. The results obtained by Rogers, Rao, and Holtz were derived
from thunderstorms observed in the Montreal vicinity, while Altman's data
were collected in central Oklahoma.

The Montreal and central Oklahoma models are found to be consistent with
the exponential model derived for this study, which relates received power,
$\overline{P}_r$, to the square root of echo area, $\sqrt{A_e}$, at a persisting gain threshold, but
some of the empirical coefficients entering the model will be sensitive to
season and location. An example of seasonal sensitivity is discussed later
in this report, where the echo model, developed predominantly from June data,
is tested against echoes occurring in late July.

Hardware

Data collected with the AN/MPS-34 weather radar were used for the
development of the statistical data base. This radar is van mounted and was
developed for Army applications requiring mobility. It is quite similar to
radar set AN/CPS-9 and, in most aspects, can be considered an improved CPS-9.
During BOMEX, the MPS-34 was located on a cliff overlooking the eastern shore
of Barbados, a site arrangement that yielded an antenna altitude of approxi-
mately 950 ft above mean sea level, and provided a vantage point for radar
surveillance of the BOMEX array to the east.

Conventional "gain stepping" of the radar receiver and scope photography
constituted the system for recording storm intensities. A complete descrip-
tion of the basic and auxiliary equipment is contained in an earlier publica-
tion by this author (Hudlow, 1970).

Calibrations

The gain-step increments were checked for each roll of 35-mm film and
were normally recalibrated if any step had drifted by more than 2 db. The
film was calibrated by inputting a signal from an x-band pulse generator.
The calibration was accomplished by photographing the PPI scope while the
antenna was rotating and while the calibration signal was changed in 2-db

increments, starting at 10 db above the minimum detectable signal (mds) and stopping at the mds; a photograph was made of each setting. This procedure documents on film a photographic minimum detectable signal. The results of the gain-step and film calibrations are presented in the publication cited above (Hudlow, 1970).

In addition to the conventional hardware calibrations, rainfall estimates derived from MPS-34 radar data for several storms were compared with those obtained from a rain-gage network inside a 35-sq. mi area in the extreme southeast portion of the island. The radar and rain-gage comparison showed the radar to underestimate the precipitation derived from the rain-gage analysis by an average factor of 6.5. This corresponds to a factor of about 12.5 (11 db) in received power. The reason for this large underestimate is not apparent but agrees with reports from other investigators (see Jones et al., 1966, pp. 11-13). Therefore, the gain-setting calibrations reported by this author (Hudlow, 1970) were adjusted by 11 db for adaptation to the echo model developed in this study.

Data Analysis

Sixty-two radar echoes represent the statistical sample selected from data collected on May 29, 1969, during 7 days in June 1969, and on July 1, 1969. The 62 echoes were all observed within 100 mi of the radar site (average range = 65 mi), with echo sizes varying in length from 4 mi to 166 mi.

The echo parameters were derived manually from photographic prints, emphasizing grid overlay and graphical techniques when possible. For example, echo area was computed by overlaying a gridded acetate onto the print and counting squares. Echo entities were identified as consisting of continuous echo area (no breaks).

The maximum power returned to the radar set from the intensity peak within an echo, $\overline{P}_{rm}$, was estimated by plotting the power corresponding to each gain threshold (in dbm) versus the square root of the echo area persisting at that threshold and extrapolating a straight-line relationship to zero area. When the value for $\overline{P}_{rm}$ derived in this manner exceeds a threshold setting of power for which echo was not observed to persist, $\overline{P}_{rm}$ is assumed equal to the threshold setting.

$\overline{P}_{rm}$ was corrected for range attenuation and for attenuation due to atmospheric constituents (oxygen and water vapor). All $\overline{P}_{rm}$ were normalized for a range of 50 mi. A mean tropical sounding was used in deriving the attenuation corrections resulting from atmospheric constituents.

The maximum dimension of the radar echoes, D_m, was scaled manually from photographs. However, D_m's derived with a software algorithm from digitized photographs were used in testing portions of the echo model.

The altitude of echo summits and the echo area existing at specific altitudes were derived from sequences of data collected at several antenna tilt angles, spaced at $\frac{1}{2}°$ increments. After corrections for earth curvature, beam width, and standard atmospheric refraction had been applied, the height

sequence data for the echoes were processed. Constant altitude plan views were manually constructed by superimposing finite range increments from photographs taken at several antenna tilt angles.

For this study, conventional least-squares techniques are used to derive empirical relationships that form the three-dimensional echo model. It is demonstrated that echo length, i.e., the maximum straight-line dimension of the echo, is a pertinent estimate of other echo geometry and echo intensity and is a useful transfer parameter for estimating precipitation. Geometric and exponential models are selected. Frequency histograms of the logarithmically transformed variables were examined for normality. Chi-square and Cornu tests for normality were run on the logarithm of echo lengths and the maximum powers (in dbm) and the null hypothesis of normality was accepted (all transformed distributions were approximately normal). Scatter diagrams for the transformed variables were examined for variability in the amount of scatter with change in magnitude of the dependent variable. An assumption of homogeneity of errors with magnitude of the dependent variable appeared reasonable for the regression analyses performed for this study.

The vertical profiles of echo area were grouped into three classes, and average values of echo area were computed for each 2,000-ft of altitude (fig. 2). Class limits were defined by echo length. Class I consisted of echoes with D_m's less than 10 mi, Class II of echoes with D_m's greater than 10 mi but not exceeding 20 mi, and Class III contained all echoes with maximum dimensions exceeding 20 mi. A three-segment model consisting of three straight lines on semilogarithmic paper adequately describes the average profiles (fig. 2).

Empirical relationships relating liquid water content and rainfall rate to reflectivity have been derived from drop-size spectra collected at the earth's surface for several geographic locations by Mueller and Sims (1969). Of the geographic locations considered by them, only Majuro in the Marshall Islands is subject to climatological influences similar to those existing in the Barbados vicinity. Therefore, Marshall Islands relationships were adopted for this study.

Figure 3 is a relative cumulative distribution giving percentages of the total precipitation content within an echo. These percentages are distributed over given percents of the total echo area as revealed by the echo model. For example, figure 3 reveals that 80 percent of the total precipitation content present in a horizontal slice through a radar echo is distributed over only about 17 percent of the total echo area. Jason Ching[2] has incorporated this result, in conjunction with a 3-D similarity liquid water profile, into a model for the vertical fluxes of liquid and water vapor due to aggregate cumulus and cumulonimbus clusters. The model predicts vertical velocities and separates the liquid water into rain (water that falls relative to the vertical velocity) and cloud (that portion of the total liquid water moving with the updrafts). The fluxes of water vapor, cloud, and rain are then computed for this hypothetical cloud cluster.

---

[2]Preliminary work in progress at the BOMAP Office.
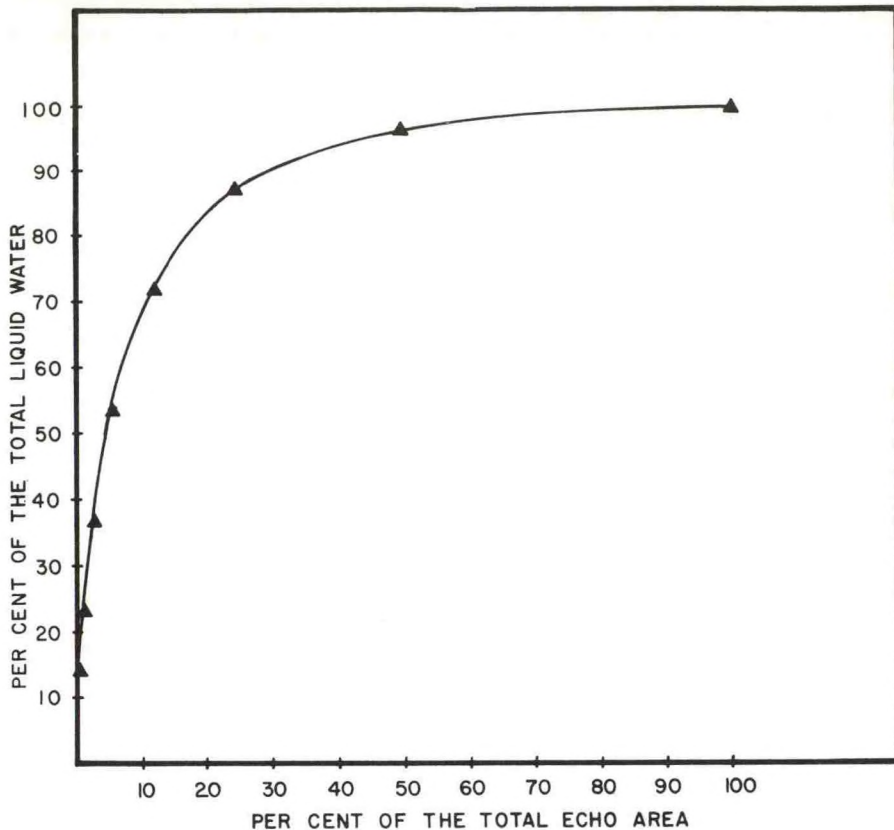
*Figure 3. Relative cumulative distribution of liquid water
for percentages of the total echo area.*

Figure 4 is a relative frequency histogram for echo lengths and repre-
sents an average distribution derived from 20 days of radar data collected
during June and July 1969. Figure 5 gives the relative amounts of precipi-
tation content deposited within an area of interest by various echo sizes.
It reveals statistically that the largest contribution to the total preci-
pitation **deposit**ed results from echoes about 30 mi long. Only 5 percent
of the precipitation is deposited from echoes less than 10 mi long.

Tests against independent data were made to further demonstrate the use-
fulness of the echo model for deriving information on the spatial and temporal
dimensional character and intensity of precipitation echoes. Echo parameters
derived from the statistical model are compared with echo parameters observed
with radar for the seven echoes listed in table 1. For these comparisons,
"observed" represents echo parameters measured directly via radar.

Figure 4. Relative frequency histogram for echo lengths.

Figure 5. Relative frequency histogram for precipitation vs. echo size.

57

*Table 1. Seven echoes used as independent tests
on the echo statistical model*
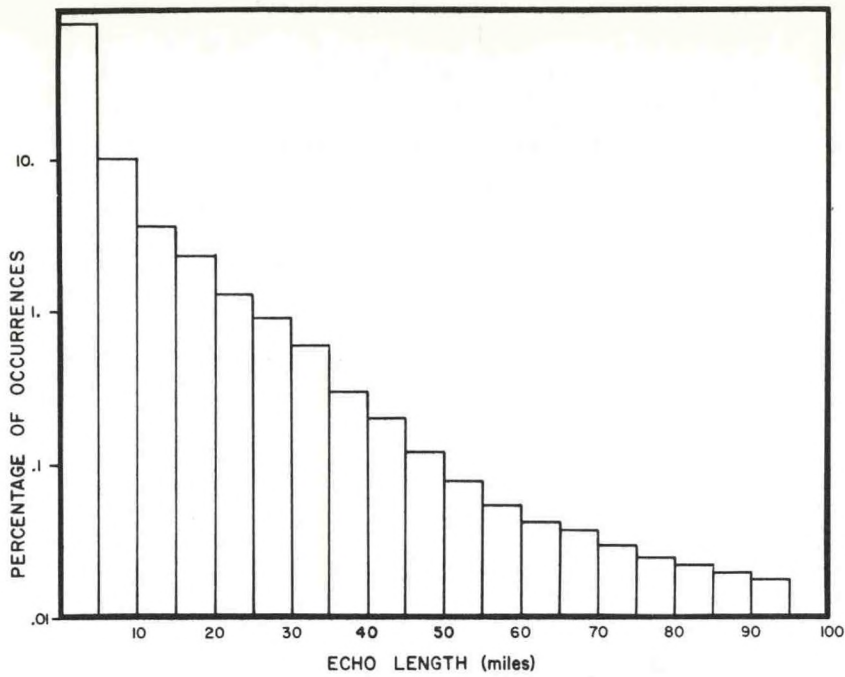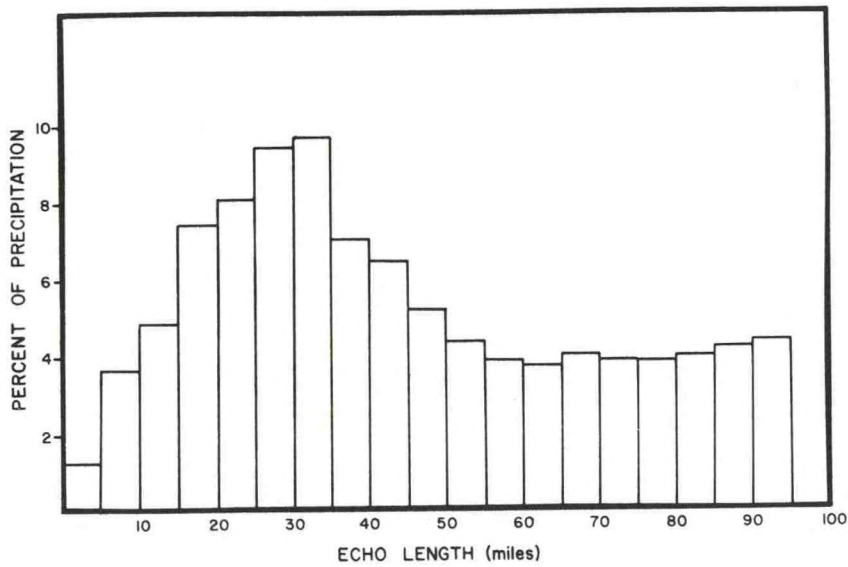
Echo	Date (1969)	Time (local)	Echo length (mi)	Range to centroid of echo (mi)
A	7/22	0404	14.5	63
B	7/22	0404	22.7	92
C	7/22	1555	5.8	82
D	7/22	1555	7.8	59
E	7/25	1557	12.3	52
F	7/25	1557	44	64
G	7/27	0205	25	82

Figure 6 appears to reveal that there is a tendency for the model to underestimate the area and height of the seven echoes (especially the larger ones). Similarly, figure 7 shows that the model generally underestimates the average rainfall rates derived from measured radar powers. This author believes that there is a strong possibility that the smaller values obtained from the model are a reflection of the sensitivity of the model to season and that the morphology of the tropical echoes used in development of the model differs somewhat from that associated with echoes occurring in late July. Nevertheless, the comparisons are, on the average, reasonably good for the relatively small number of echoes considered.

A more powerful test for the statistical model consists of comparing time marches of echo area and average rain rates derived from the statistical model with those estimated directly from digitized gain-step data. Figures 8 through 11 represent comparisons for 3 days in June 1969. June 29 was a moderately disturbed day, while the June 22 and 26 periods were relatively inactive in terms of convective activity. With the exception of rain rates occurring during the first 6-hour period of June 29, remarkable agreement between the model and the "observed" is evident from these four figures.

The discrepancy (factor of 2.6) in rainfall rate for the first 6-hour period on June 29 stems largely from a data-digitizing problem. BOMEX radar data were digitized at a spatial resolution equal to 4 mi. Through digitization a lengthy line of broken echoes was united into one large echo. The nonlinear dependence of rainfall rate on echo size resulted in an appreciable overestimate for this 6-hour period.
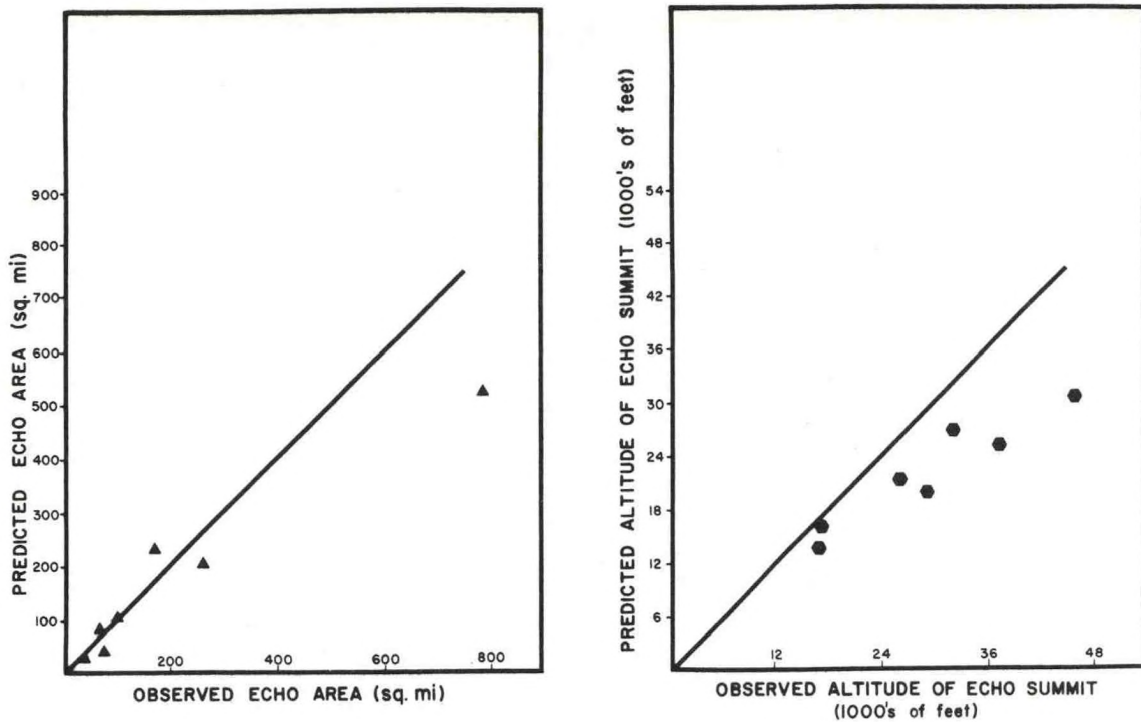
Figure 6. *Echo areas (left) and echo summits (right) given by the statistical model compared with observed values for seven echoes.*
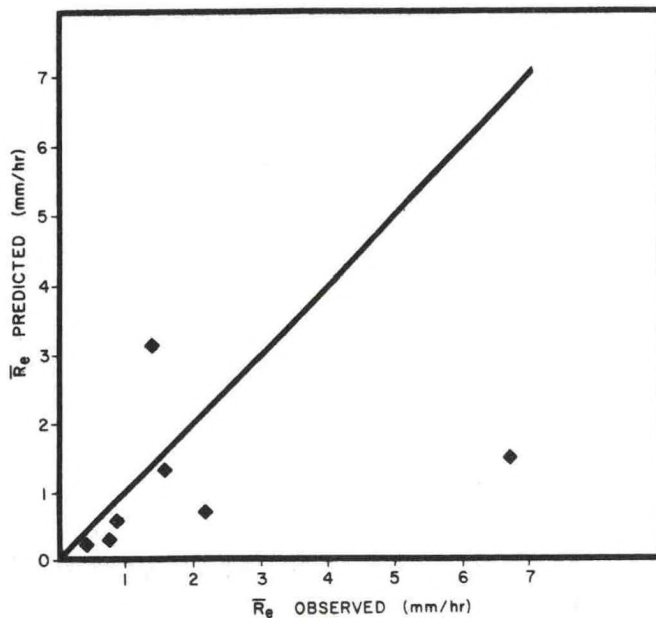
Figure 7. *Rainfall rate averaged over a horizontal slice through a radar echo given by the statistical model compared with derived values based on observed values for b (slope coefficient in mi^{-1}) and $\overline{P}_{rm}$.*

59
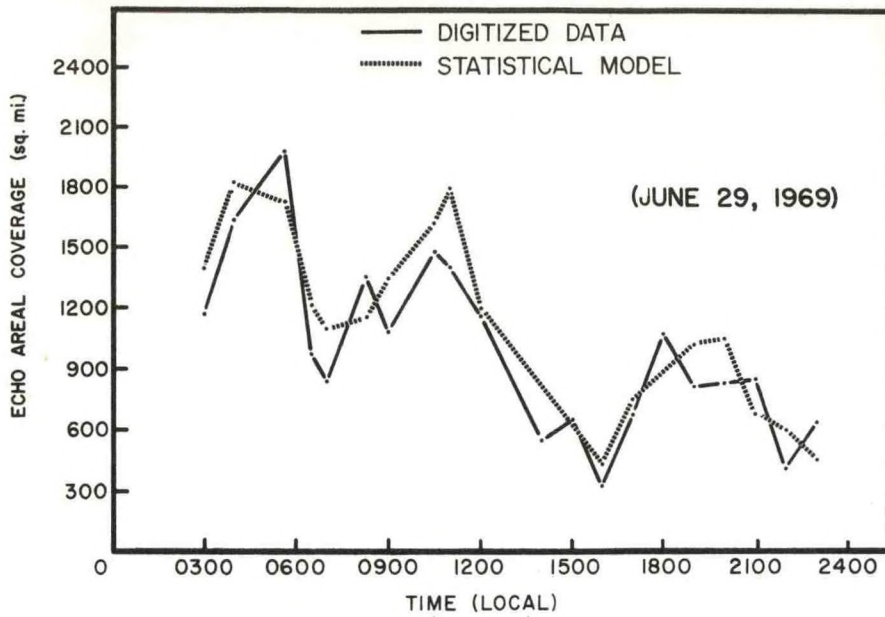
Figure 8. *Echo areal coverage derived from the statistical model compared with that obtained directly from digitized data.*
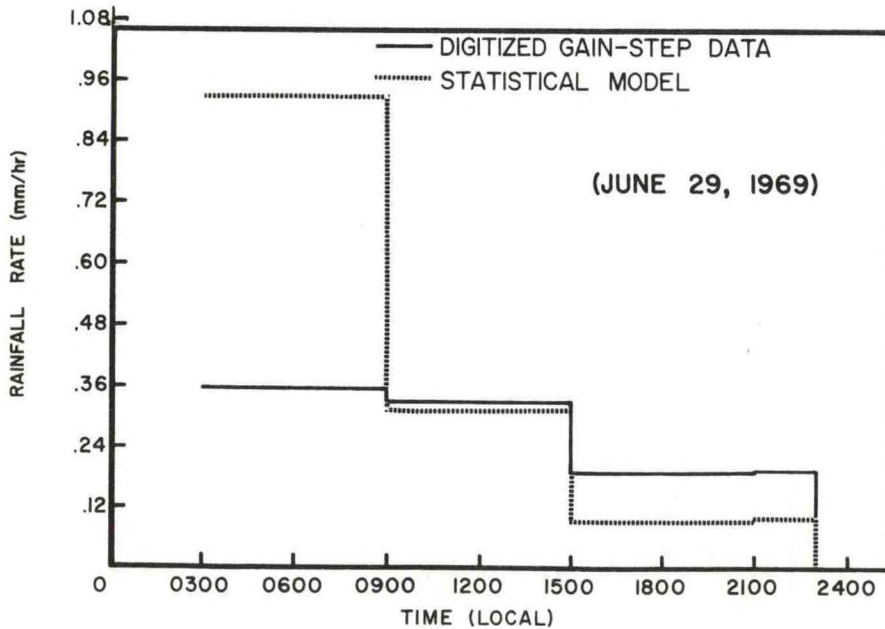
Figure 9. *Average rainfall rate over a 12,000-m² area for 6-hour intervals derived from the statistical model compared with those obtained directly from digitized gain-step data.*
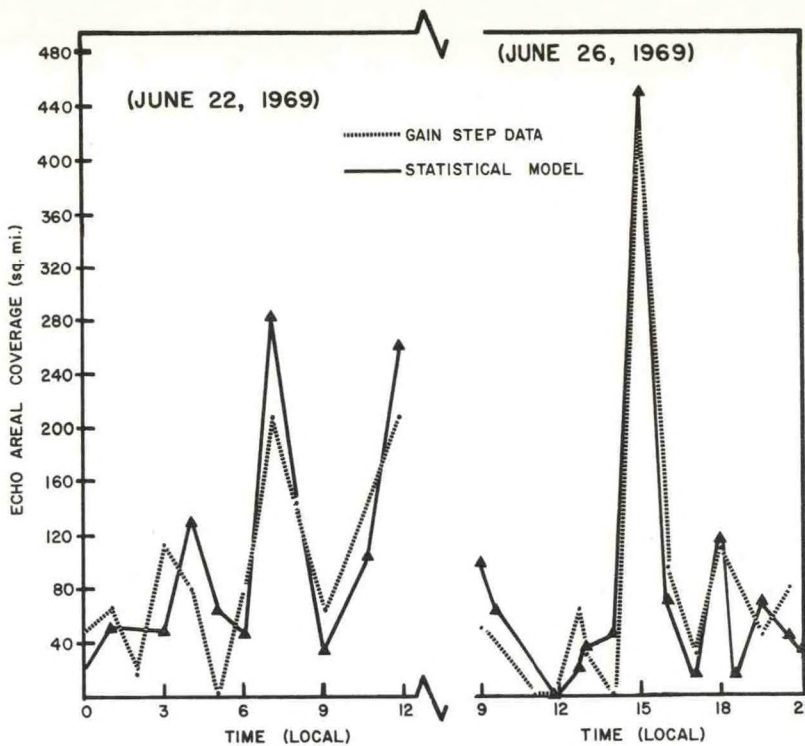
Figure 10. *Echo areal coverage derived from the statistical model compared with that obtained directly from digitized data for periods on June 22 and 25, 1969.*
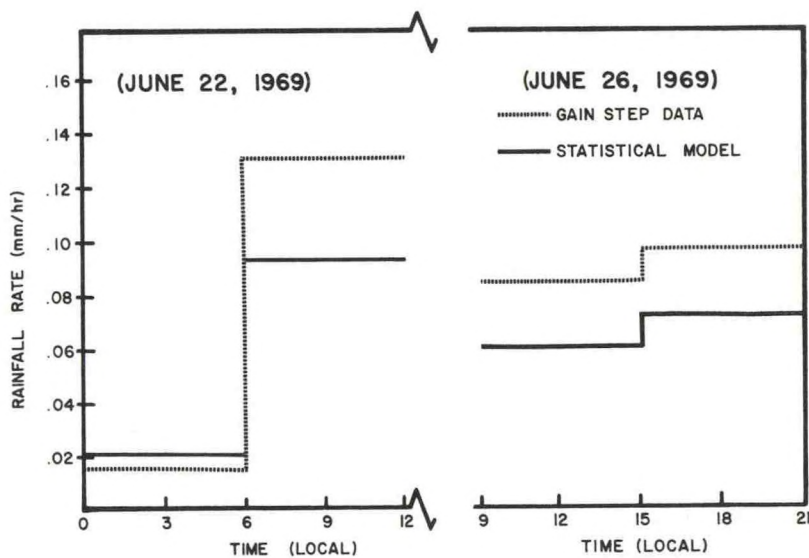
Figure 11. *Average rainfall rates over a 3,000-mi² area for 6-hour intervals derived from the statistical model compared with those obtained directly from digitized data for periods on June 22 (left) and 25 (right).*

Conclusions

The following conclusions concerning tropical precipitation echoes are the important ones inferred from this study:

(1) Echo length is a pertinent parameter for estimating echo area and echo height.

(2) The exponential relationship relating the received power at a gain threshold to the square root of the echo area persisting at the threshold, provides a useful means for deriving estimates of the spatial distribution and quantity of precipitation within an echo.

(3) The slope and intercept coefficients required to define the exponential relationship can be estimated, given the echo's maximum dimension.

(4) As revealed by the echo model, a major portion of the precipitation content, contained in a horizontal slice of the radar echo, is distributed over a relatively small portion of the total area of the radar echo. For example, about 80 percent of the liquid water present in a horizontal slice of the echo is contained within about 17 percent of the total area of the cross section.

(5) As revealed by the model, the precipitation spectrum giving the quantity of precipitation deposited within an area of interest by precipitation echoes of various sizes peaks at an echo length of about 30 mi. Also, it is found that echo sizes less than 10 mi contribute only about 5 percent to the precipitation deposited.

References

Altman, F.J., "Storm Reflectivity Models," Preprints for 14th Radar Meteorology Conference, Tucson, Arizona, 1970, pp. 291-295.

Byers, H.R., "The Use of Radar in Determining the Amount of Rain Falling Over a Small Area," Transactions of the American Geophysical Union, Vol. 29, 1948, pp. 187-196.

Holtz, C.D., "A Model of the Distribution of Precipitation in Three Dimensions," Proceedings of the 13th Radar Meteorology Conference, McGill University, Montreal, 20-23 August 1968, published by the American Meteorological Society, pp. 110-113.

Hudlow, M.D., "Weather Radar Investigations on the BOMEX," Research and Development Report ECOM-3320, U.S. Army Electronics Command, Fort Monmouth, N.J., 1970, 106 pp.

Kessler, E., "Computer Program for Calculating Average Lengths of Weather-Radar Echoes and Pattern Bandedness," Technical Note 3-NSSL-24, National Severe Storms Laboratory, Norman, Oklahoma, 1965, pp. 99-110.

Jones, R.F. (chairman): "Use of Ground-Based Radar in Meteorology (Excluding Upper-Wind Measurements)," Technical Report No. 78-WMO-No. 193 TP. 99, World Meteorological Organization, Geneva, Switzerland, 1966, pp. 11-13.

Mueller, E.A., and Sims, A.L., "Relationships Between Reflectivity, Attenuation, and Rainfall Rate Derived From Drop Size Spectra," Final Report, Technical Report ECOM-02071-F, Illinois State Water Survey at the University of Illinois, Urbana, Ill., 1969, 112 pp.

Rogers, R.R., and Rao, K.M., "A Preliminary Microwave Attenuation Climatology for the Montreal Area Based on Weather Radar Data," Scientific Report MW-52, Stormy Weather Group, McGill University, Montreal, 1968, 38 pp.

A Technique for Assessing Probable Distributions of Tropical Precipitation Echo Lengths for X-Band Radar From Nimbus 3 HRIR Data

Wolfgang D. Scherer and Michael D. Hudlow
BOMAP Office

The need for developing a procedure for simulating radar echoes from Nimbus 3 satellite high-resolution infrared (HRIR) data for BOMEX arises from the fact that surface radar coverage during the experiment was limited to the southern half of the BOMEX volume. In order to derive precipitation estimates for the entire box, a means for assessing probable distributions of radar echoes from satellite data is needed. Once echo lengths and their number are estimated, their contribution to precipitation estimates can be calculated based on a three-dimensional precipitation echo model that relates precipitation to echo length as described by Dr. Hudlow in his paper.

The results presented must be taken as preliminary, because so far we have analyzed only 14 cases in which radar data and satellite data reasonably matched in time were available. This desired simultaneity was usually within $\pm$ 15 min and never more than $\pm$ 30 min. Since 14 cases do not represent a large statistical sample, the absolute numbers calculated in this analysis may change as more data are examined.

The satellite data used in this investigation are nighttime HRIR data of equivalent blackbody temperatures in a Mercator projection grid. By assuming clouds to be at essentially the same temperature as the surrounding atmosphere and by using an average temperature sounding derived from radiosonde data for the BOMEX array, we were able to convert the temperature isopleths to pressure levels. Certain characteristics of the areal distribution of these pressure contours were then used to stratify the HRIR data into three disturbance classes: Class I - the undisturbed case - no appreciable cloud area higher than 450 mb above sea level; Class II - the intermediate case - no appreciable area higher than 650 mb above sea level; and Class III - the disturbed case - appreciable cloud area at the 650-mb level and above. All pressures refer to the p* system, i.e., they express pressure difference

with respect to sea level pressure (Rasmusson, 1971).

Statistics of dimensional characteristics of radar echoes for BOMEX show a correlation between the degree of disturbance and the summit height of observed radar echoes. Dr. Mike Hudlow shows[1] that the summit height of radar echoes is correlated with the echo length (correlation coefficient, 0.84), i.e., the greater the echo length, the greater is the degree of disturbance and the accompanying precipitation. Therefore, for the tropics it seems reasonable to expect a good correlation between cloud height and area as derived from HRIR data and the degree of convective activity, if we assume contamination of the satellite data due to cirrus and cirrostratus to be minor. If cirrus or cirrostratus does exist over large areas at altitudes greater than 650 mb above sea level (about 30,000 ft), we assume that it is associated with cumulonimbus activity.

The radar data were stratified into undisturbed, intermediate, and disturbed classes corresponding to the classes established for the satellite data. Cumulative frequency distributions of radar echo lengths were derived for each class and are presented in figure 1. Although the cases in which both radar and satellite data were available are too few, these frequency distributions compare favorably with other frequency distributions for the BOMEX volume derived for a different time period and from larger amounts of radar data (Hudlow, 1970).

Next, comparisons of the average radar echo area with the average satellite cloud area for each class (degree of disturbance) were made. The HRIR cloud area was measured at various pressure levels. These comparisons, shown in figure 2, were made for 20,000-mi^2 areas located within 150 mi of the radar sites; an example is shown in figure 3. Since the radar echo area increases with the degree of disturbance, the ratio of radar echo area to satellite cloud area for a given fixed satellite cloud area increases as the degree of disturbance increases.

Since we calculate the ratio of echo area to cloud area, this ratio must be less than 1 for physical reasons, i.e., the radar echo area must be smaller than the cloud area within which it is located. This restriction limits the choice for the undisturbed case to the 200-mb level (see fig. 2). The choice of the comparison levels for classes II and III was determined in order to maintain a constant average ratio. This constant average ratio of radar echo area to satellite cloud area of 0.25 is obtained by choosing appropriate pressure levels for computing this ratio. Thus, for Class I, the ratio of radar echo area to satellite cloud area is derived from the 200-mb level. For the intermediate and disturbed cases this ratio is obtained at the 500-mb level. An areal comparison for a disturbed case on June 21, 1969, 0300 GMT, is shown in figure 3 as a superposition of contoured HRIR and radar echo data within an area in the southeast corner of the BOMEX box subtending approximately 20,000 mi^2. The reasonably good overlap of the 500-mb contours and the radar echoes (shaded regions) indicates relatively small geographical gridding errors.

---

[1] Work in progress at the BOMAP Office.
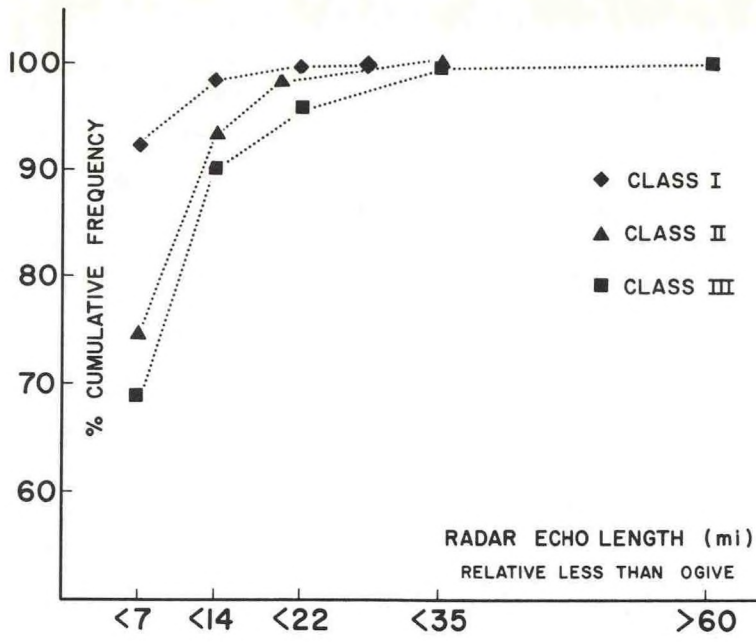
Figure 1. *Frequency distribution of radar echo lengths for island and Discoverer surface radars (14 cases).*
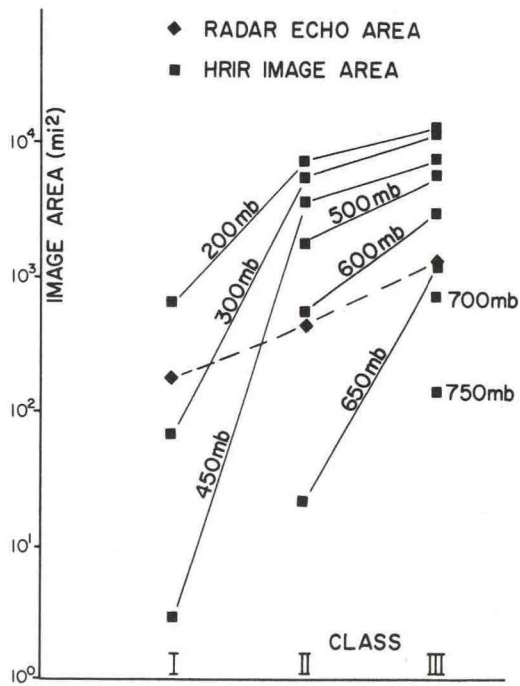
Figure 2. *Radar – HRIR area comparisons.*

65
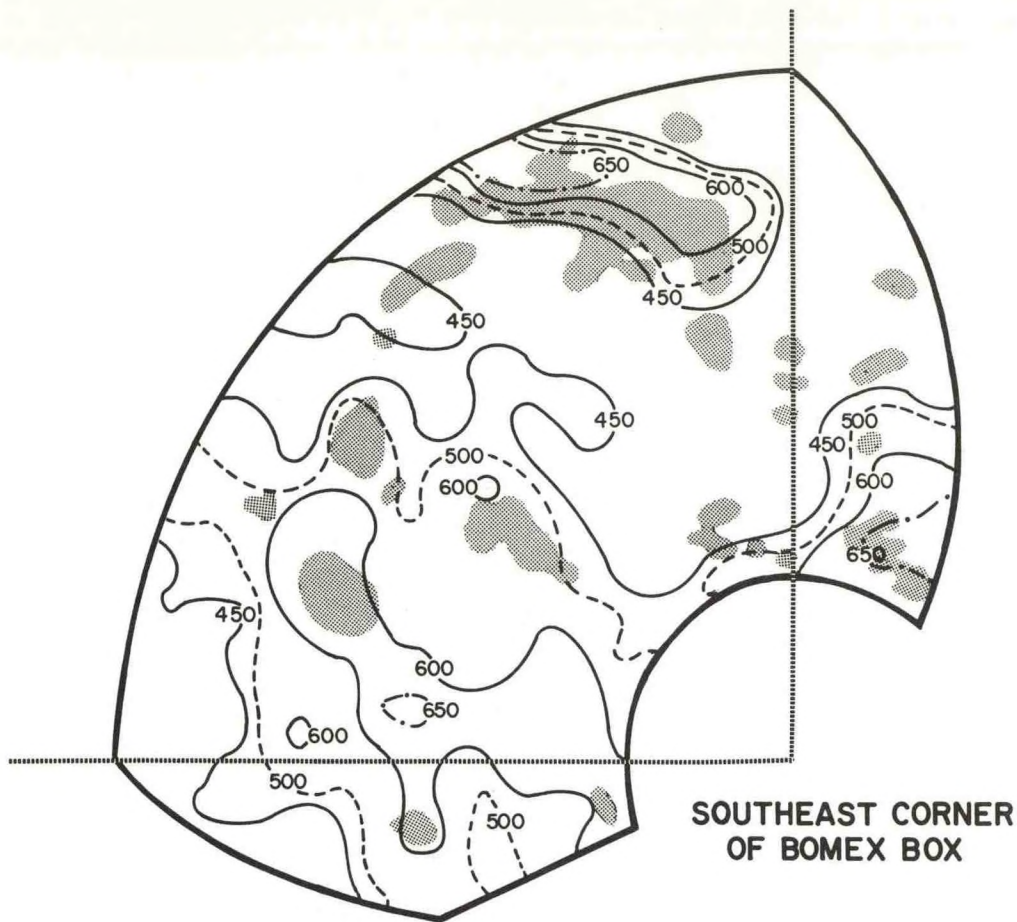
Figure 3. Superposition of radar echoes on a contoured HRIR map.

Once the comparison levels and the ratio of radar echo area to satellite cloud area have been established, the procedure for obtaining precipitation estimates for a chosen mesoscale tropical region is as follows:

(1) Select class according to degree of disturbance based on HRIR criteria.

(2) Compute HRIR cloud area (a) subtended by the 200-mb contour for Class I and (b) subtended by the 500-mb contour for Classes II and III.

(3) Estimate total radar echo area via average radar-satellite ratio.

(4) Derive by a reiteration procedure the number of echoes of various sizes from the average distribution of echo lengths appropriate for the class of disturbance (fig. 1) and the statistical relationship between echo area and echo length, as discussed by Dr. Hudlow.

66

(5) Estimate precipitation from the echo lengths and their distribution, based on a three-dimensional precipitation model.

Figures 4 and 5 show some results and tests of this procedure through step 4 for a disturbed and an intermediate case, respectively. The predicted total echo areas for the two test cases agree well with the actually observed echo areas. However, there is a proportionally larger difference between the total number of predicted echoes and the total number of observed echoes. This discrepancy is further reflected in the histograms, which show both the number of observed and predicted echoes in various length classes. The disagreement between the observed and predicted echo numbers is a reflection, at least partly, of the inadequate number of cases analyzed for the derivation of the echo length frequency distributions and the relationship linking statistically the area and length of a radar echo.
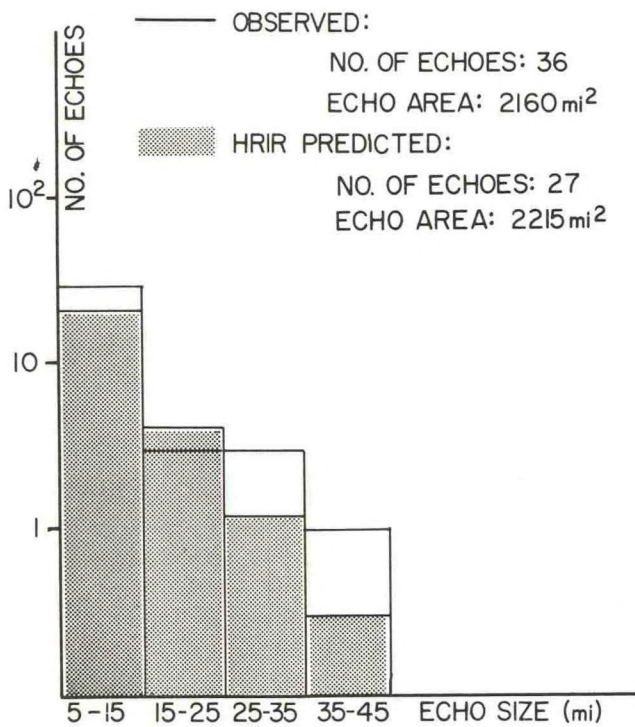
Figure 4. Comparison of observed radar echo lengths and echo lengths simulated from HRIR data (disturbed case).
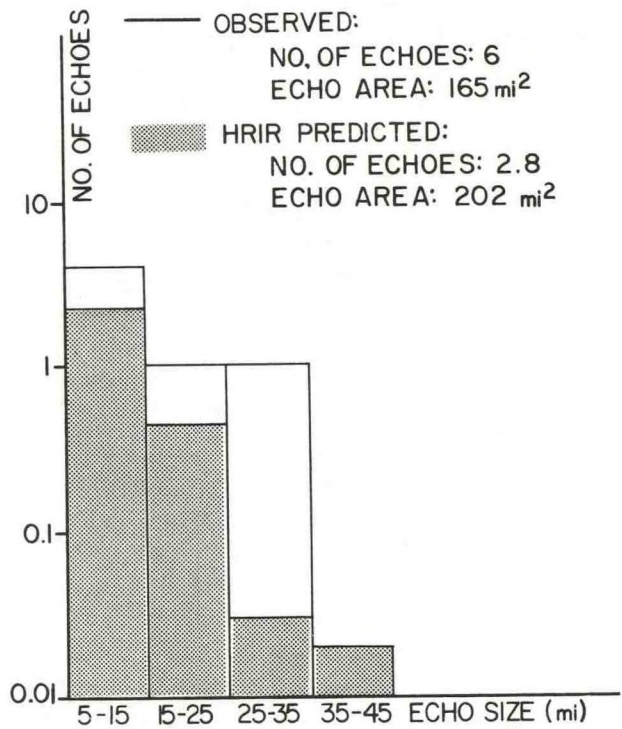
Figure 5. Comparison of observed radar echo lengths and echo lengths simulated from HRIR data (intermediate case).

References

Hudlow, M.D.: "Weather Radar Investigations on the BOMEX," Research and Development Report, ECOM-3320, U.S. Army Electronics Command, Fort Monmouth, N.J., 1970.

Rasmusson, E.M., "Mass, Momentum, and Energy Budget Equations for BOMAP Computations," NOAA Technical Memorandum ERL BOMAP-3, January 1971.

Analysis of Radiosonde Humidity Errors Based on BOMEX Data

H.L. Crutcher, National Climatic Center
L.D. Sanders and J.T. Sullivan, BOMAP Office

Introduction

The carbon hygristor currently used in United States radiosondes has been found to yield incorrect humidities because the temperature of the hygristor and of the air passing through the hygristor duct differ from that of the ambient air as sensed by the outrigger thermistor.

The temperature difference stems mainly from heating of the black hygristor by solar radiation, by heat transfer from the sonde package, and from thermal lag of the hygristor as the sonde ascends (or descends in the case of the dropsonde) through the atmosphere with its temperature changes. The problem is further aggravated by the reduction in the rate of airflow through the hygristor duct of the radiosonde and a resultant reduction in heat transfer rate from hygristor to air, thereby increasing the thermal lag time. Also, thermal conditioning of the radiosonde before release apparently contributes to an initial hygristor temperature anomaly in the lowest 50 mb of the sounding.

Humidity errors resulting from the heating effect on the hygristor have been noted by Wallace and Chang (1969), Teweles (1970), Morrissey and Brousaides (1970), and Ostapoff, Shinners, and Augstein (1970). Bunker (1953), Mathews (1965), Morrissey and Brousaides (1970), and Harney (1971) have discussed the problems of thermal lag and ventilation. Teweles (1970) listed modifications to the duct that have been suggested in order to minimize the radiation errors and to reduce the thermal lag of the hygristor by increasing the ventilation rate. An improved duct has been designed and is planned to be in operational use by the latter part of 1971 or early 1972. The duct will be fabricated of material more opaque to solar radiation, will have a blackened interior, a substantial improvement in ventilation rate, and will have a separate duct channel beneath the hygristor duct to insulate it from the rest of the sonde package. It is expected that these modifications will substantially reduce the errors due to heating of the hygristor by solar radiation and by heat transfer from the sonde package. The error due to thermal lag of the hygristor will be substantially reduced by the improved ventilation, but will still exist.

The hygristor is an excellent sensor of the true humidity of an air sample. However, if the hygristor and the sensed air sample in its immediate vicinity have temperatures different from the ambient free-air temperature, the sensed relative humidity will not represent the humidity of the free air, but rather the humidity the ambient air would have if its temperature were changed to that of the hygristor. Thus, when the sensor relative humidity is related to the ambient air temperature as measured by the thermistor, the sensed and computed relative humidity will be too low if the hygristor temperature is higher than the ambient free-air temperature. The converse is also true.

In the case of the ascending radiosonde, three effects are quite noticeable: the effects of solar and package heating, the effect of thermal lag, and the effect of pre-release thermal conditions. The thermal lag, in response to decreasing temperature, causes the hygristor to yield both day and night humidity values that are too low. The solar effect, of course, is absent at night. The lag effect will approach zero in isothermal conditions and will reverse sign in inversions. Depending upon conditions before release, the sonde package may be either warmer or colder than the air temperature at release, causing humidity errors of either sign. This effect may manifest itself in an abrupt decrease of specific humidity from the surface value, based on psychrometric observations aboard ship, to the first point of the sounding, and unusually low humidities through the lowest 50 mb (approximate).

In the case of dropsondes, the hygristor is mounted on an outrigger and the resulting five- to ten-fold increase in its ventilation rate compared with that of the radiosonde substantially reduces the daytime solar radiation and package heating errors. The thermal lag effect will give an error of opposite sign to that given by the radiosonde. The net effects of the greater dropsonde ventilation rate (shorter lag time) and higher rate of change of temperature because of the dropsonde's fall speed tend to offset each other, however, and give a humidity error **caused by lag** that is of approximately the same magnitude as the radiosonde's. Thus, if simultaneous nighttime radiosonde and dropsonde soundings at the same location were available, these could be used to evaluate the lag corrections required for both instruments to bring the two humidity soundings into agreement.

Correction Procedure

Equiprobability Transformation -- Figure 1 schematically illustrates a procedure by which one set of biased measurements can be modified. The curves shown represent cumulative percent frequency distributions of specific humidity obtained during BOMEX from aircraft and radiosondes, nighttime and daytime, in the lowest 300 m of the soundings. These have been measured at the same position in time and space. The best set, the aircraft data, is considered the master set.

If we are interested only in averages, then the modifying procedure would be to change the 50th percentile values of the radiosonde distributions to the 50th percentile value of the aircraft data. Thus, a 14.0 g/kg value for the night radiosonde distribution and the 16.6 g/kg value for the day radiosonde distribution would be increased to about 17.8 g/kg for the aircraft distribution. In figure 1, the arrows at (a) of the 50th percentile from

14.0 g/kg upward and then horizontally to the "A curve and then downward illustrate this.

If we wish to modify an individual reading, we can use the following technique. Let us suppose, for example, that a 13.6 g/kg reading is obtained from the day radiosonde (RD) sounding. We then proceed upward from 13.6 g/kg to the radiosonde day curve. The intersection occurs at about 0.33 on the cumulative percent frequency curve. We then go to the same cumulative percent frequency on the aircraft curve, and from this intersection proceed downward to the abscissa at 17.6 g/kg. The daytime curve can be modified to the nighttime curve value at 16.3 g/kg, or both can be modified to the 17.6-g/kg aircraft value.

The difference between the aircraft (A) and nighttime radiosonde (RN) distribution curves in figure 1 reflects the thermal lag effect. The difference between the radiosonde (RN) and day (RD) curves reflects the solar radiation effect and, possibly, thermal conditioning before release.

Lag Corrections -- From Middleton and Spilhaus (1953), the following approximation is derived:

$$(T_h - T_a)_2 = (T_h - T_a)_1 \; e^{-t/\lambda} - \beta\lambda \; (1 - e^{-t/\lambda}), \tag{1}$$
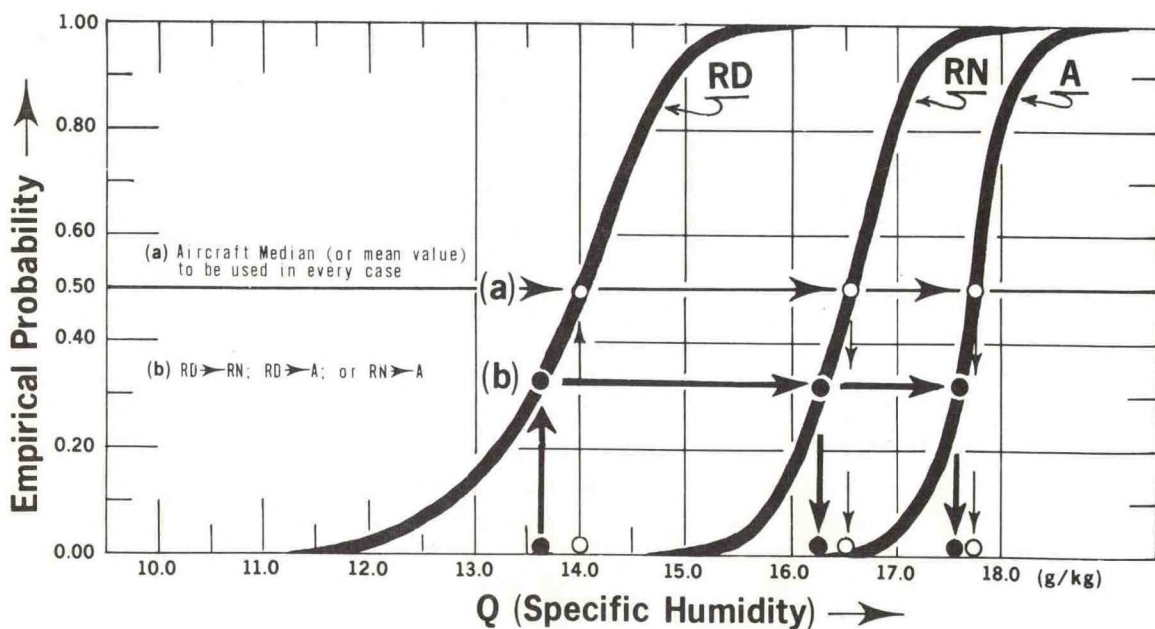
Figure 1. Schematic of proposed procedure for correction of BOMEX radiosonde humidity data. Curves represent actual cumulative frequency (empirical probability) distributions of specific humidity from daytime radiosonde (RD), nighttime radiosonde (RN), and aircraft measurements (A).

70

where T_h is the hygristor temperature in °C, T_a is the temperature of the ambient air in °C (as sensed by the thermistor), and t is the time in seconds since the previous point in the sounding. The time lapse rate term β equals $\Delta T_a/\Delta t$ and is assumed to be a constant between each pair of consecutive points. The lag constant in seconds is λ; subscripts 1 and 2 denote values at successive points in the sounding.

An initial approximation to the lag constant λ as determined by Glaser (Teweles, 1970) was considered to be about 30 sec, but it does vary with air density and ventilation rate. From lag constant calibration data for thermistors and application to BOMEX soundings, the following tentative relationship has been derived:

$$\lambda = 34.9(\rho V_V)^{-0.4} , \tag{2}$$

where ρ is the air density in kg/m^3 and V_V is the ventilation rate in meters per second.

The ventilation rate for the National Weather Service radiosonde has been determined by Ostapoff et al. (1970; see also Teweles, 1970) to be 28 to 33 percent of the ascent rate, i.e., approximately

$$V_V(R/S) = 0.3 \, A, \tag{3a}$$

where A is the ascent rate in meters per second.

As noted earlier, the dropsonde hygristor was mounted on an outrigger arm directly in the airstream and ventilated at the fall velocity (approximately) 7.5 to 11.5 m/sec). Because the descent rates were not readily available for the BOMEX dropsondes, an approximate equation was derived from a small sample that gives the descent rate as a function of air density. Vertical air motions were ignored. The validity of this equation,

$$V_V(D/S) = 8.7 \, \rho^{-0.6}, \tag{3b}$$

will be tested further with a larger sample and modified as required.

By substituting equations (3a) and (3b) into equation (2), we obtain the respective lag constants for the radiosonde, λ_R, and for the dropsonde, λ_D:

$$\lambda_R = 34.9 \, (0.3 \, \rho \, A)^{-0.4} \tag{4a}$$

$$= 56.5 \, (\rho \, A)^{-0.4},$$

and

$$\lambda_D = 14.7 \, \rho^{-0.16} \tag{4b}$$

The true ambient relative humidity at the ambient thermistor temperature, T_a, can be written

$$(RH)_a = \{e_s(T_h) \ / \ e_s(T_a)\} \ (RH)_i, \tag{5}$$

where $(RH)_i$ is the indicated relative humidity, and $e_s(T_h)$ and $e_s(T_a)$ are the saturation vapor pressures at the hygristor temperature and at ambient air temperature, respectively.

The above equations and their constants have been derived from the limited calibration data available, from a small set of data from BOMEX Period III (June 19 - July 2, 1969), and from results of previous work on this problem. They should therefore be considered preliminary and tentative, subject to change as this study progresses. Forthcoming BOMAP publications on this subject will be more specific and precise, and will contain supporting data from the literature as well as from BOMEX.

Pre-release Thermal Conditioning Errors -- Evidence exists that pre-release heating or cooling may cause humidity errors that affect the lower levels of the radiosonde soundings. Specifically, in some instances there appears to be heating from the ship's deck and superstructure; in others, cooling from the deck or from keeping the radiosonde in a cool room before release. This problem must be studied in more detail.

Solar Radiation Correction -- In order to evaluate the humidity error caused by solar heating of the hygristor and sonde package, we must first remove the errors due to thermal lag of the hygristor and to pre-release thermal conditioning. Evaluation of the magnitude of this error due to solar heating, and corrective procedures, will be covered in future reports.

Correction of Other Errors -- Effects other than those mentioned above are believed to be less significant and are given a lower priority for the present. These include heat generated by the sonde's battery and electronic components, entrainment of the heated wake of the balloon into the hygristor duct, variation of ventilation rate caused by the swinging of the sonde (Harney, 1971), wet-bulb effect of the thermistor when the sonde passes from cloud to dry warm air in and above the inversion, and pressure sensor errors due to drift and hysteresis. In addition, there are the residual instrumental errors inherent in the manufacturing process. These effects will be analyzed as time permits.

Results of the Lag Correction Procedures

The equations given in the preceding section have been used in modifying the BOMEX radiosonde and dropsonde humidity data shown in figures 2 through 4. Figure 2 shows the radiosonde, dropsonde, and aircraft data from and near the *Oceanographer* on June 26, 1969, during the night. Included are the radiosonde and dropsonde temperature data, identified as T_R and T_D, and specific humidity data, identified as R and D. The soundings are shown from about 1,020 mb (1.02 bar) to 750 mb (.75 bar). The abscissa scale is broken in order for both temperature and specific humidity data to be shown.

In figure 2, the radiosonde unmodified data are represented by the heavy broken line marked R, while the dropsonde unmodified data are identified by the dotted line marked D. The corrected humidity profiles are marked R_c and D_c, respectively. The aircraft data are shown at about 300, 1,300, and 2,300 m above sea level and are identified by solid circles and triangles. The circles indicate data obtained from a Cambridge Systems dew-point hygrometer; the triangles indicate data obtained from an infrared hygrometer. The times of observation for the radiosonde and dropsonde are, respectively, 0302 and 0235 GMT and for the aircraft 0212, 0242, 0554, and 0624 GMT. The aircraft was in the air more than 5 hours. The corrections to the curves are generally in the right direction, but at some levels there is an over-correction. The fact that the two soundings are removed in time and space by about ½ hour and 50 n mi may have some bearing on this.

Figure 3 illustrates another set of nighttime soundings, made on June 24, 1969. The ship is the *Discoverer* in the southeast corner of the BOMEX array. Here the corrected humidity profiles show good agreement only below 960 mb and near 850 mb, beneath the inversion. The difference in the corrected curves between these two levels may be the result of insufficient corrections, or may represent true differences over the 50-n-mi separation between the two soundings. The aircraft data in this case appear low, but they were
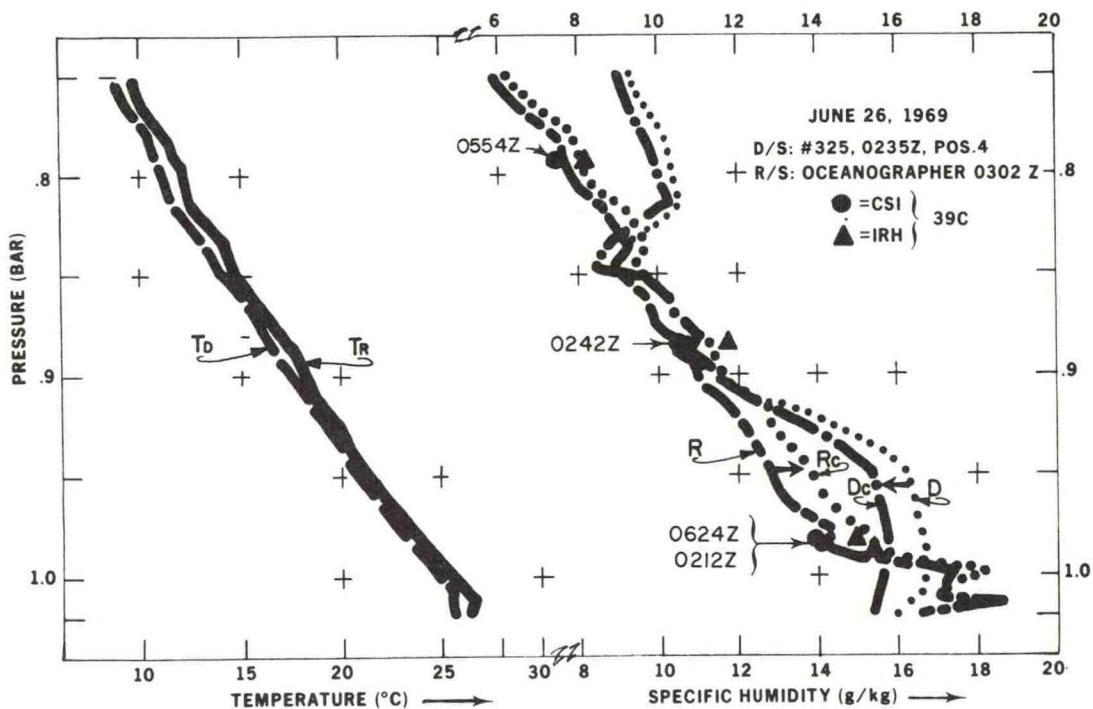

Figure 2. *Radiosonde and dropsonde temperatures and specific humidities, before and after correction for thermal lag of hygristor, compared with aircraft-measured specific humidity. Nighttime soundings, June 26, 1969.*
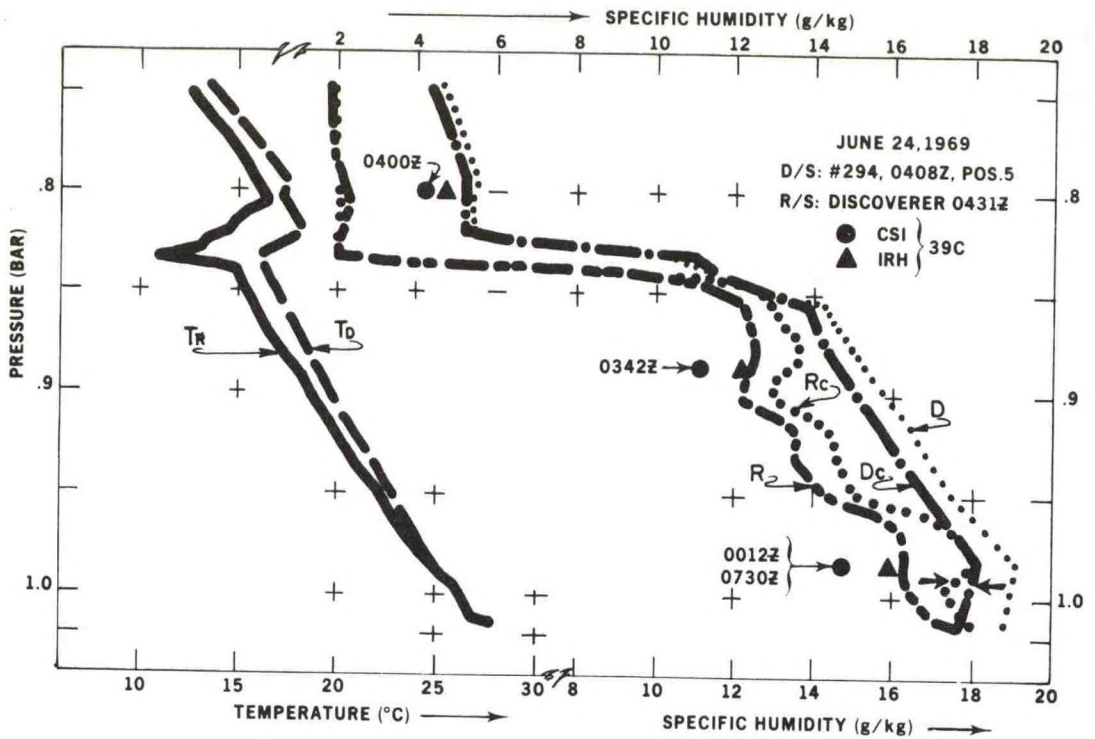
Figure 3. Same as fig. 2, for nighttime soundings, June 24, 1969.
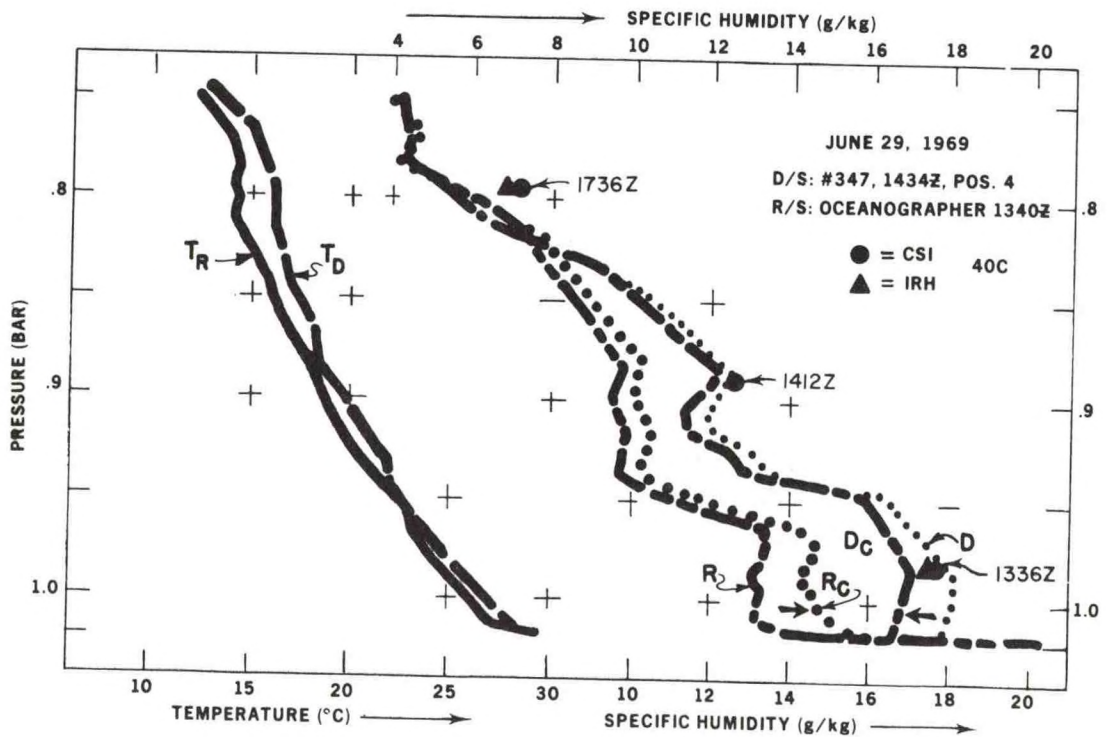
Figure 4. Same as fig. 2, for daytime soundings, June 29, 1969.

74

obtained from the DC-6 39C aircraft of NOAA's Research Flight Facility (RFF) and are known to be less reliable than data from the RFF DC-6 40C. The anomaly in the radiosonde temperature curve near 840 mb is presumably created by (a) evaporative cooling at the top of clouds and/or (b) the "wet-bulb effect" resulting from evaporation of moisture collected on the thermistor during ascent through the clouds.

The daytime pair of soundings in figure 4 perhaps better illustrates the modifying procedure. The soundings were made at and near the *Oceanographer* on June 29, 1969. Here, the sounding modification requires further correction. This, obviously, is the correction required for the solar heating effect on the radiosonde hygristor. Also, apparent heating effects from the ship's deck and superstructure are seen in both the radiosonde temperature and humidity curves. The surface temperature and humidity readings are those from the shipboard sling psychrometer rather than from the radiosonde.

Summary

Radiosondes and dropsondes currently used in the United States yield incorrect humidities for several reasons. For the radiosonde these include the effects of solar radiation during the day, inadequate ventilation, and thermal lag in the hygristors. For the dropsonde, the error is due mainly to thermal lag.

Lag corrective procedures have been established, and tentative lag constants determined. Results appear to be satisfactory, but a second evaluation of the constants in the lag correction equations, based on a larger data sample, will be made before final modifications of the BOMEX soundings.

Other effects, such as those of solar radiation, package heating, and pre-release thermal conditioning, are being checked and will be covered in subsequent reports.

References

Bunker, A.F., "On the Determination of Moisture Gradients From Radiosonde Records," Bulletin of the American Meteorological Society, Vol. 34, 1953, pp. 406-409.

Harney, P.J., "Tests on Ventilation Rates and Other Factors in Radiosonde Performance," Journal of Applied Meteorology, Vol. 10, 1971, pp. 295-300.

Mathews, D.A., "Some Research on the Lithium Chloride Radiosonde Hygrometer and a Guide for Making it," Humidity and Moisture, I, Reinhold Publishing Corporation, New York, N .Y., 1965, pp. 228-247.

Middleton, W.E.K., and Spilhaus, A.F., Meteorological Instruments, 3rd revised edition, University of Toronto Press, Toronto, Canada, 1953, 286 pp.

Morrissey, J.F., and Brousaides, F.J., "Temperature-Induced Errors in the ML-476 Humidity Data," Journal of Applied Meteorology, Vol. 9, 1970, pp. 805-808.

Ostapoff, F., Shinners, W.W., and Augstein, E., "Some Tests on the Radiosonde Humidity Error," NOAA Technical Report ERL 194-AOML 4, Atlantic Oceanographic and Meteorological Laboratories, Miami, Fla., 1970, 50 pp.

Teweles, S., "A Spurious Diurnal Variation in Radiosonde Humidity Records," Bulletin of the American Meteorological Society, Vol. 9, 1970, pp. 836-840.

Wallace, J.M., and Chang, C.P., "Spectrum Analysis of Large-Scale Wave Disturbances in the Tropical Lower Atmosphere," Journal of Atmospheric Sciences, Vol. 26, 1969, pp. 1010-1025.

III. TEMPORARY BOMEX DATA ARCHIVE

To receive, conserve, and disseminate BOMEX data, a special archive was
established by NOAA's Environmental Data Service in February 1971. Data that
had been sufficiently processed, reduced, and documented at that time were
transferred from the BOMAP Office to the temporary archive. It is defined as
"temporary" since much of the data are made available at an early state in
the continuing BOMAP processing activity. As this processing cycle is fin-
ished, a permanent archive will be established, containing all data of general
interest, whether originally collected by government facilities or by univer-
sity and private organizations.

A detailed description of the archived data, including processing and
reduction procedures and inventory tables, will be contained in a forthcoming
NOAA Technical Report to be issued by the Environmental Data Service. Once
published, this report will be furnished every user requesting data from the
archive. Pending publication of this report, users of BOMEX data are referred
to BOMEX Bulletin No. 9, which contains a first edition of the inventory
tables, as well as ordering instructions and costs. The following tables of
supplementary items that have been deposited in the archive since the initial
announcement appear on the next few pages in the same form they appeared in
BOMEX Bulletin No. 9:

> Fixed-Ship Salinity/Temperature/Depth and Sea Surface Temperature Data,
> table 3-5;
>
> Island, *Discoverer*, Air Force WB-47, Navy WC-121, RFF DC-6 39C,
> RFF DC-6 40C, and RFF DC-4 82E Radar Data, table 3-7; and
>
> RFF Aircraft Cloud Photography Data, table 3-8.

Explanatory material concerning each category of archived data not found
in BOMEX Bulletin No. 9 is available on microfilm.

Table 3-5. Fixed-Ship Salinity/Temperature/Depth and Sea Surface Temperature Observed Data Inventory (Additional STD 8 sps Data Indicated by Asterisk)

Order by designation in this column	Name of ship	Archived form of data[1,2]	Contents	Date and time of first observation, 1969 — Date	Hr:Min	Date and time of last observation, 1969 — Date	Hr:Min	Duplication cost	Availability date for distribution
B9045*	Oceanographer	Magnetic tape	STD 8 sps Data	June 20	1022	June 24	2106	$60.00 per magnetic tape (includes cost of reel)	2/1/71
B9046*	=	=	=	July 25	0053	30	0910	=	=
B9008	=	=	=	11	1011	July 17	2111	=	=
B9009	=	=	=	18	0056	21	2223	=	=
B9010	=	=	=	22	0057	25	2123	=	=
B9011	=	=	=	26	0056	29	0316	=	=
B9044*	Rainier	=	=	June 21	0118	July 2	0121	=	=
B9047*	Mt. Mitchell	=	=	20		3	0212	=	=
B9040*	Discoverer	=	=	21	0100	June 26	2100	=	=
B9041*	=	=	=	27	0059	July 2	1156	=	=
B9005	=	=	=	July 11	0558	17	2100	=	=
B9006	=	=	=	18	0000	23	2100	=	=
B9007	=	=	=	24	0000	27	1520	=	=
B9042*	Rockaway	=	=	June 19	2143	June 25	1225	=	=
B9043*	=	=	=	26	0304	July 2	1228	=	=

[1] When ordering magnetic tape, specify (A) 7 channel; BCD; 556 or 800 BPI; or (B) 9 channel; EBCDIC; 800 BPI. (On special request, a 7 channel, BCD, 200 BPI magnetic tape copy is available at a cost of $180.00 per order number in the far left column.)

[2] A computer tabulation of all 8 sps data on one of the magnetic tapes (B9005 to B9011) is also available. When ordering a printout, specify magnetic tape number, ship's name, date and time of first observation and date and time of last observation. Example: "Listing of B9005, Discoverer, July 11/0558, July 17/ 2100." Cost is $30.00 per magnetic tape printout.

Table 3-7. Addition to Island, Discoverer, Air Force WB-47, Navy WC-121, RFF DC-6 39C, RFF DC-6 40C, and RFF DC-4 82E Radar Data inventory

Order by reel No. in this column[1]	Type of radar	Data acquisition unit	Date and time of first frame		Date and time of last frame		Duplication cost [2]		Availability date for distribution
			Calendar date, 1969	Hr:Min	Calendar date, 1969	Hr:Min	Registered	Nonregistered	
187	APS-20	RFF DC-6 39C	July 11	(GMT) 1438	July 11	(GMT) 2112	$20.00	$9.00	2/8/71
188	WP-101	"	" 11	1433	" 11	1719	"	"	" "
189	APS-20	RFF DC-6 40C	" 11	1554	" 11	2004	"	"	" "
190	WP-101	"	" 11	1121	" 11	1816	"	"	" "
191	"	"	" 11	1818	" 11	2208	"	"	" "
192	RDR-1	"	" 11	1334	" 11	1817	"	"	" "
193	"	"	" 11	1818	" 11	2210	"	"	" "
194	RDR-1	RFF DC-6 39C	" 13	1355	" 13	2000	"	"	" "
195	"	"	" 13	2001	" 13	2225	"	"	" "
196	APS-20	RFF DC-6 40C	" 13	1431	" 13	2223	"	"	" "
197	WP-101	"	" 13	1230	" 13	1933	"	"	" "
198	"	"	" 13	1934	" 13	2226	"	"	" "
199	RDR-1	"	" 13	1232	" 13	2034	"	"	" "
200	"	"	" 13	2035	" 13	2226	"	"	" "
201	APS-42	RFF DC-4 82E	" 13	1225	" 13	1507	"	"	" "
202	APS-20	RFF DC-6 39C	" 14	1430	" 14	2345	"	"	" "
203	RDR-1	"	" 14	1335	" 14	2021	"	"	" "
204	"	"	" 14	2023	" 14	2345	"	"	" "
205	APS-20	RFF DC-6 40C	" 14	2120	" 14	2345	"	"	" "
206	WP-101	"	" 14	1448	" 14	2105	"	"	" "
207	"	"	" 14	2106	" 14	2353	"	"	" "
208	RDR-1	"	" 14	1339	" 14	2104	"	"	" "
209	"	"	" 14	2104	" 14	2353	"	"	" "

[1]Radar film will be sent as a positive copy.

[2]When ordering radar film, specify registered or nonregistered copy. Allow 3 weeks for delivery of registered and 2 weeks for delivery of nonregistered film after receipt of request.

Table 3-7. Addition to Island, Discoverer, Air Force WB-47, Navy WC-121, RFF DC-6 39C, RFF DC-6 40C, and RFF DC-4 82E Radar Data inventory (continued)

Order by reel No. in this column [1]	Type of radar	Data acquisition unit	Date and time of first frame		Date and time of last frame		Duplication cost [2]		Availability date for distribution
			Calendar date, 1969	Hr:Min	Calendar date, 1969	Hr:Min	Registered	Nonregistered	
210	APS-42	RFF DC-4 82E	July 15	1210	July 15	1702	$20.00	$9.00	2/8/71
211	APS-20	RFF DC-6 39C	18	1145	18	2013	" "	" "	" "
212	RDR-1	"	18	1145	18	1845	" "	" "	" "
213	"	"	18	1546	18	2013	" "	" "	" "
214	APS-20	RFF DC-6 40C	18	1136	18	1921	" "	" "	" "
215	"	"	18	2002	18	2128	" "	" "	" "
216	WP-101	"	18	1323	18	1352	" "	" "	" "
217	"	"	18	1518	18	2128	" "	" "	" "
218	RDR-1	"	18	1116	18	1522	" "	" "	" "
219	"	"	18	1523	18	2128	" "	" "	" "
220	APS-42	RFF DC-4 82E	18	1114	18	2053	"	"	"
221	APS-20	RFF DC-6 40C	20	1636	20	2218	" "	" "	" "
222	WP-101	"	20	1521	20	2223	" "	" "	" "
223	RDR-1	"	20	1520	20	2223	" "	" "	" "
224	APS-42	RFF DC-4 82E	21	1309	21	1743	"	"	"
225	APS-20	RFF DC-6 40C	23	1502	23	2223	" "	" "	" "
226	WP-101	"	23	1240	23	1935	" "	" "	" "
227	"	"	23	1937	23	2223	" "	" "	" "
228	"	"	23	1240	23	1932	" "	" "	" "
229	"	"	23	1933	23	2223	" "	" "	" "
230	APS-42	RFF DC-4 82E	23	1240	23	2129	"	"	"

[1] Radar film will be sent as a positive copy.

[2] When ordering radar film, specify registered or nonregistered copy. Allow 3 weeks for delivery of registered and 2 weeks for delivery of nonregistered film after receipt of request.

Table 3-7. Addition to Island, Discoverer, Air Force WB-47, Navy WC-121, RFF DC-6 39C, RFF DC-6 40C, and RFF DC-4 82E Radar Data inventory (continued)

Order by reel No. in this column [1]	Type of radar	Data acquisition unit	Date and time of first frame		Date and time of last frame		Duplication cost [2]		Availability date for distribution
			Calendar date, 1969	Hr:Min	Calendar date, 1969	Hr:Min	Registered	Nonregistered	
				(GMT)		(GMT)			
231	RDR-1	RFF DC-6 39C	July 25	1016	July 25	1720	$20.00	$9.00	2/8/71
232	=	=	" 25	1720	" 25	2154	=	=	" "
233	=	=	" 26	1324	" 26	2006	=	=	" "
234	=	=	" 26	2006	" 26	0017	=	=	" "
235	APS-20	RFF DC-6 40C	" 26	1028	" 26	2000	=	=	" "
236	WP-101	=	" 26	1011	" 26	1706	=	=	" "
237		=	" 26	1707	" 26	2003	=	=	" "
238	RDR-1	=	" 26	1012	" 26	1704	=	=	" "
239	=	=	" 26	1705	" 26	2000	=	=	" "
240	APS-42	RFF DC-4 82E	" 26	0916	" 26	1615	=	=	"
241	WP-101	RFF DC-6 39C	" 28	1435	" 28	2143	=	=	"
242	=	=	" 28	2144	" 28	2351	=	=	"
243	RDR-1	=	" 28	1435	" 28	2142	=	=	"
244	=	=	" 28	2143	" 28	2351			"

[1] Radar film will be sent as a positive copy.

[2] When ordering radar film, specify registered or nonregistered copy. Allow 3 weeks for delivery of registered and 2 weeks for delivery of nonregistered film after receipt of request.

Table 3-8. Additions to RFF Aircraft Cloud Photograph Data Inventory

Order by designation in this column[1]	Film type	Aircraft	Type of camera	Contents of reel					Distribution cost	Availability date for distribution
				Date and time of first frame		Date and time of last frame		RFF flight No.		
				Calendar Date, 1969	Hr:Min (GMT)	Calendar Date, 1969	Hr:Min (GMT)			
713 AF	16-mm 400-ft reel, color	RFF DC-6 39C	Nose	July 13	1338	July 13	2235	690713	$108.00 per 400-ft reel	1/24/71
714 AF	"	"	"	14	1430	14	2230	690714	=	=
718 AF	"	"	"	18	1235	18	2018	690718	=	=
720 AF	"	"	"	20	1457	20	2152	690720	=	=
723 AF	"	"	"	23	1229	23	2118	690723	=	=
726 AF	"	"	"	26	1258	26	2212	690726	=	=
728 AF	"	"	"	28	1418	28	2230	690728	=	=
713 AR	35-mm 800-ft reel, black & white	RFF DC-6 39C	Right side camera	July 13	1201	July 14	2230	690713 690714	$88.00 per 800-ft reel	=
718 AR	"	"	"	18	1108	20	2152	690718 690720	=	=
723 AR	"	"	"	23	1227	25	2037	690723 690725	=	=
726 AR	"	"	"	26	1257	28	2219	690726 690728	=	=
713 AL	"	RFF DC-6 39C	Left side camera	July 13	1201	July 14	2215	690713 690714	=	=
718 AL	"	"	"	18	1108	20	2152	690718 690720	=	=
723 AL	"	"	"	23	1227	25	2021	690723 690725	=	=
726 AL	"	"	"	26	1257	28	2230	690726 690728	=	=

[1] Allow 4 to 6 weeks delivery after receipt of request.

Table 3-8. Additions to RFF Aircraft Cloud Photograph Data Inventory (continued)

Order by designation in this column [1]	Film type	Aircraft	Type of Camera	Contents of reel					Distribution cost	Availability date for distribution
				Date and time of first frame		Date and time of last frame		RFF flight No.		
				Calendar Date, 1969	Hr:Min (GMT)	Calendar Date, 1969	Hr:Min (GMT)			
713 BF	16-mm 400-ft reel, color	RFF DC-6 40C	Nose	July 13	1024	July 13	2140	690713	$108.00 per 400-ft reel	1/24/71
714 BF	"	"	"	14	1314	14	1802	690714	"	=
718 BF	"	"	"	18	1135	18	1305	690718	"	=
720 BF	"	"	"	20	1513	20	2159	690720	"	=
723 BF	"	"	"	23	1230	23	1351	690723	"	=
726 BF	"	"	"	26	1012	26	1728	690726	"	=
511 BR	35-mm 800-ft reel, black & white	RFF DC-6 40C	Right side camera	May 11	1020	May 12	2125	690511 690512	$88.00 per 800-ft reel	=
711 BL	"	RFF DC-6 40C	Left side camera	July 11	1334	July 11	0518	690711	=	=
713 BL	"	"	"	13	1200	14	2209	690713 690714	=	=
718 BL	"	"	"	18	1100	20	2227	690718 690720	=	=
723 BL	"	"	"	23	1230	26	2007	690723 690726	=	=

[1] Allow 4 to 6 weeks for delivery after receipt of request.

IV. ANNOUNCEMENT

Research based on BOMEX data is progressing in government and university laboratories, but these programs will exploit only part of the research potential available. To take advantage of this scientific resource, NOAA recently announced that it is prepared to assist graduate students in atmospheric science and oceanography to visit the BOMAP Office in order to examine data, confer with the BOMAP staff, and identify data sets to be requested for their research. To this end, NOAA offers to provide round-trip travel from anywhere in the contiguous United States, and per diem at the rate of $20 per day for up to five days for graduate students whose applications are approved. Inquiries should be directed to Mr. Valti W. Powell, Operations Manager, BOMAP Office.

Since funds for this assistance program are limited, qualified applicants will be assisted on a first-come first-serve basis. Applicants should have a general familiarity with BOMEX (see references below), should identify a reasonably specific research topic or area of interest in their letter of inquiry, and should include endorsement by a faculty member who is familiar with their qualifications and plans.

References

BOMEX Bulletin Nos. 4-10, BOMAP Office, U.S. Department of Commerce, NOAA, Rockville, Md. 20852.

Davidson, Ben, "The Barbados Oceanographic and Meteorological Experiment," Bulletin of the American Meteorological Society, Vol. 49, 1968, pp. 928-934.

Kuettner, J.P., and Holland, J., "The BOMEX Project," Bulletin of the American Meteorological Society, Vol. 50, 1968, pp. 394-402.

Holland, J.Z., "Preliminary Report on the BOMEX Sea-Air Interaction Program," Bulletin of the American Meteorological Society, Vol. 51, 1970, pp. 809-820.